



UNIVERSITÀ DELLA CALABRIA



UNIVERSITA' DELLA CALABRIA

Dipartimento di Meccanica, Energetica E Gestionale

Dottorato di Ricerca in
INGEGNERIA DEI MATERIALI E DELLE STRUTTURE

Con il contributo di
Commissione Europea, Fondo Sociale Europeo e Regione Calabria

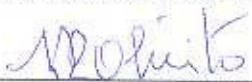
CICLO XXVI

TITOLO TESI

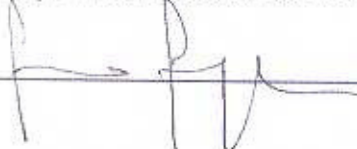
**FATIGUE AND FRACTURE BEHAVIOR IN NICHEL-TITANIUM BASED
SHAPE MEMORY ALLOYS**

Settore Scientifico Disciplinare : ING/IND-14

Coordinatore: Ch.mo Prof. R. OLIVITO

Firma 

Supervisore/Tutor: Ch.mo Prof. F. FURGIUELE

Firma 

Dottorando: Dott. EMANUELE SGAMBITTERRA

Firma 

TABLE OF CONTENTS

INTRODUCTION AND SCOPE OF RESEARCH.....	1
--	----------

CHAPTER 1: NITI BASED SHAPE MEMORY ALLOYS: OVERVIEW

1.1. Introduction.....	3
1.2. Crystallographic Structure: Martensitic Transformation.....	5
1.3. Characteristic Temperatures and Phase Transformations....	13
1.4. Shape Memory Effect.....	16
1.4.1. One Way Shape Memory Effect.....	16
1.4.2. Two Way Shape Memory Effect.....	17
1.5. Pseudoelasticity.....	19
1.6. A More General Overview of Shape Memory Behavior.....	22
1.7. Main Shape Memory Alloys.....	23
1.7.1. Niti Shape Memory Alloy.....	23
1.7.1.1.The Nickel-Titanium System.....	24
1.7.1.2.Near-Equiatomic Nickel-Titanium.....	25
1.7.2. Alloys with Narrow Hysteresis.....	28
1.7.3. Alloys with Wide Hysteresis.....	28
1.7.4. High Temperature Smas.....	28
1.7.5. Copper Based Alloys.....	29
1.7.6. Iron-Based Alloys.....	30
1.8. Applications.....	30
1.8.1. Aerospace Applications.....	31
1.8.2. Medical Applications.....	34
1.8.3. Transportation Applications.....	39
1.8.4. Other Applications.....	39

CHAPTER 2: FATIGUE OF PSEUDOELASTIC NITI WITHIN THE STRESS INDUCED TRANSFORMATION REGIME

2.1. Introduction.....	41
2.2. Materials and Experiments.....	46
2.3. Functional and Structural Fatigue.....	50
2.3.1. Recovered and Residual Strain.....	54
2.3.2. Recovered and Dissipated Energy.....	56
2.3.3. Transformation Stress and Young's Modulus.....	58
2.3.4. Transformation Temperatures.....	59
2.4. Strain-life Fatigue Model.....	60
2.5. SEM Analyses of the Fracture Surfaces.....	64
2.6. Summary.....	66

CHAPTER 3: DIGITAL IMAGE CORRELATION TECHNIQUE: OBERVIEW

3.1. Introduction.....	67
3.2. 2Dimensional DIC.....	69
3.3. Specimen Preparation and Image Capture.....	69
3.4. Basic Principles and Concepts.....	71
3.4.1. Basic Principles.....	71
3.4.2. Shape Function/Displacement Mapping Function.....	73
3.5. Correlation Criterion.....	76
3.6. Interpolation Scheme.....	76
3.7. Displacement Field Measurement.....	77
3.7.1. Initial Guess of Deformation.....	77
3.7.2. Calculation Path.....	80
3.7.3. Sub-Pixel Displacement Registration Algorithms.....	81
3.7.3.1.Coarse–Fine Search Algorithm.....	81
3.7.3.2.Peak-Finding Algorithm.....	81
3.7.3.3.Genetic Algorithms.....	82

3.7.3.4. Finite Element Method and B-Spline Algorithm.....	83
--	----

CHAPTER 4: FATIGUE CRACK PROPAGATION IN NITI BASED SYNGLE CRYSTAL SHAPE MEMORY ALLOYS.

4.1. Introduction.....	84
4.2. Material and Experimental Procedure.....	85
4.3. Digital Image Correlation (DIC) Analysis.....	88
4.4. Fatigue Crack Propagation.....	91
4.5. Fatigue Crack Closure.....	94
4.6. Summary.....	100

CHAPTER 5: CRACK TIP STRESS DISTRIBUTION AND STRESS INTENSITY FACTOR IN NITI SHAPE MEMORY ALLOYS

5.1. Introduction.....	101
5.2. Fracture Mechanics in Smas: Basic Mechanisms and Analytical Modeling.....	102
5.3. Experiments.....	105
5.4. Numerical Modeling.....	106
5.5. Results and Discussions.....	108

REFERENCES.....	117
------------------------	------------

INTRODUCTION AND SCOPE OF RESEARCH

In this dissertation, the results of the research activities carried out during the Doctoral Course at the University of Calabria are presented. The aim of these activities regarded the interesting field of Smart Materials and, in particular, some aspects related to the functional and structural behavior of Nickel-Titanium (NiTi) Shape Memory Alloys (SMAs). Smart Materials are a very interesting class of materials due to their ability to completely recover high applied strain, and an original recorded shape, by give in input thermal energy.

NiTi alloys are the most promising Shape Memory Alloys in terms of practical applicability; due to their special functional properties, namely one way or two way shape memory effect (OWSME, TWSME) and superelastic effect (SE), NiTi components have seen growing use in recent years in a number of industrial fields as biomedical, automotive, aeronautic and many others. Generally, the use of the these alloys seems to be very useful in applications where it is necessary to use smart components with low dimensions. Many conventional actuators and sensors could be substituted with NiTi ones, obtaining high advantages in terms of reduction of weight and dimensions, reliability and costs. Furthermore, in the last years, their use for the realization of smart composites, as an example for vibration and shape control, is becoming very interesting.

Unfortunately, there are still some difficulties with shape memory alloys that must be overcome before they can live up to their full potential. For example, these alloys are still relatively expensive to manufacture compared to other materials such as steel and aluminium. These difficulties regard the high sensibility to the production parameters and the low workability of NiTi alloys. Furthermore, the high non linearity characteristic of their behaviour increases the difficulties related to the control of their functional properties and to predict their resistance. In fact classic theories, applied to fatigue and fracture mechanic calculation, cannot be applied.

In this dissertation, the results related to different investigations carried out on a NiTi alloy are presented. In particular, using proper experimental procedures, the thermomechanical behaviour of the material was investigated under static and cyclic conditions to better understand the deformation mechanisms involved in the shape memory effect.

Furthermore, strain controlled fatigue tests of a commercial pseudoelastic nickel–titanium (NiTi) shape memory alloy (SMA) have been carried out in this investigation. In particular, flat dog-bone shaped specimens, obtained from commercial NiTi sheets, have been analyzed, under pull–pull loading conditions, in two subsequent steps: (i) material stabilization and (ii) fatigue life estimation. The first step was carried out to obtain a stable pseudoelastic response of the SMA, i.e. with no residual deformations upon unloading, and it can be regarded as a preliminary processing condition of the alloy.

Large ratcheting strains have been observed from the first mechanical cycles, up to a complete stabilization of the stress-strain response of the material. These mechanisms, mainly attributed to the formation of stabilized martensite and dislocation networks, cause a marked evolution of the functional properties of the alloy in terms of pseudoelastic recovery capabilities. This evolution has been systematically analyzed by identifying some functional damage parameters, involving strain, energy, transformation stress, Young's modulus and phase transition temperatures. Furthermore, a modified Coffin–Manson approach for fatigue life estimation of SMAs is proposed, which takes into account the strain mechanisms involved during repeated stress-induced martensitic transformations.

Fatigue crack propagation, in the stable microstructures (martensite and austenite) of the alloy has been also investigated. In particular single crystal alloys of the same atomic composition, have been studied by using the Digital Image Correlation optic technique, in order to calculate the effective crack propagation law, by using the displacement field at the crack tip, recorded during the load history.

Furthermore the fracture properties have been investigated by analytical studies, FE simulations and experiments. In particular, single edge crack (SEC) specimens have been analyzed for different operating temperature in the pseudoelastic regime of the alloy. The phase transition mechanisms occurring in the crack tip region, together with the resulting stress distribution, have been analyzed by a recent analytical model [167-169] as well as by FE simulations, carried out by using a special constitutive model for SMAs. Finally, experiments have been carried out, by using SEC specimens obtained from NiTi sheets by electro-discharge machining (EDM). The results have been analyzed by LEFM theory, and the analytical model has been used to calculate modified SIFs for SMAs.

CHAPTER 1

NITI BASED SHAPE MEMORY ALLOYS: OVERVIEW

1.1 Introduction

The shape memory effect (SME), associated to a solid phase transformation of a metal, has been firstly observed by two researchers, Chang and Read [1], in 1932. They observed an unexplainable phenomenon while performing research on the bending behavior of Gold-Cadmium bars. Upon loading, the AuCd bar deformed in a way consistent with expectation. However, after load removal and subsequent heating, the bar returned to its original undeformed shape. At the time of this bending experiment, the unique thermo-mechanical behavior of AuCd was not completely understood. However, during the years, the knowledge of this experiment has been improved. Today, the ability of a material to apparently "remember" its original shape upon heating is called the "shape memory effect", and materials which demonstrate this effect are classified as "shape memory alloys" (SMA).

Subsequently, a similar behavior was observed in 1938 in a CuZn (brass) alloy at the Massachusetts Institute of Technology, but official recognition of shape memory alloys took place only thirty years later, in 1962, when Buehler [2] and his collaborators at the laboratories of the NOL (U.S. Naval Ordnance Laboratory) accidentally discovered the equiatomic Nickel-Titanium (NiTi) shape memory alloy while they were working on a project on a material resistant to corrosion and high temperatures. Since then, many researchers started to study this class of materials and, in particular, the Nitinol (acronym of nickel, titanium and NOL) [3,4,5].

In the following decades, the shape memory alloys became the subject of considerable interest, both scientific and commercial, and many products, made with this kind of material, started to be adopted in different application fields like mechanical engineering, chemistry, medicine, hydraulic stuff, aerospace industry, automobile industry.

For example many devices for space missions, like satellites can be realized by exploiting the peculiar properties of shape memory alloys (SMA).

The satellites, realized for commercial, scientific or military purposes, need of active and passive components that exploit the potentiality of SMA. The big cross-linked

structures, by which the space stations are built, have low stiffness and their assembly is quite complex: devices made with shape memory alloys allow a smoother handling of these issues. Furthermore, for the antennas opening and solar panels adopted in space station Mir, the Russian space program has developed devices that take advantage from the shape memory effect. NASA uses successfully, from several years, SMA actuators, which have replaced the old mechanisms.

Such a success is due to their unique properties related to the shape memory effect, one-and two-way, to the superelasticity and their ability to dampen vibrations, but, mainly, to their property to be easy designed and adapted to the most different demands.

Since the eighties of the twentieth century, the properties of these materials have been investigated more thoroughly from a macroscopic point of view, to understand their complex mechanisms of transformation, called martensitic transformation. Consequently, it can be said that this class of materials has dual charm, for its increasingly number of applications and for the phenomena that characterize its phase transformations.

In the last years many other shape memory alloys have been introduced like NiFeGa, CuZnAl and CuAlNi. Their properties are very different: for example the NiFeGa, that is a ferromagnetic alloy, has the capability to be activated by using a simple magnetic field, and it is able to recover imposed deformation in the order of 14%. However, their cost is still more expensive than NiTi and not many informations, about their structural behavior, are available in letterature. The copper based alloys, on the contrary, are really cheap in comparison with the other shape memory materials, and moreover they can be fused in a very easier way and manifest a wider transformation range. But, in any case, the NiTi alloys manifest a higher recovery in deformation due to the shape memory effect (up to 10% compared to 5% of the copper based), they are more thermally stable, they have excellent resistance to corrosion and stress corrosion. Furthermore, due to their greater mechanical strength, they can be use in mechanical joints, and thanks to the corrosion resistance, just mentioned, as well as biocompatibility, they can be use NiTi in the biomedical field, to realize stent or pins for bone fractures.

For all of these reasons, today, NiTi is the most studied and applied shape memory alloys.

1.2 Crystallographic Structure: Martensitic Transformation.

The SMA materials are characterized by two main properties: the shape memory effect (SME), i.e. the ability to "remember" their original shape after significant applied deformation and the pseudo-elasticity (PE); they are related to the possibility of such materials to manifest, in certain thermo-mechanical conditions, particular microscopic crystallographic configurations known as the martensitic and austenite (also known as beta or "*parent*") phase. The presence of either phase depends mainly on the temperature and/or on the applied stress. The austenite (γ phase) is stable at high temperature and low applied stress and is characterized by a body centered cubic cell (CCC), while the martensite (α' phase), is stable at low temperature and high applied stress and has a distorted monoclinic cell (figure 1.1).

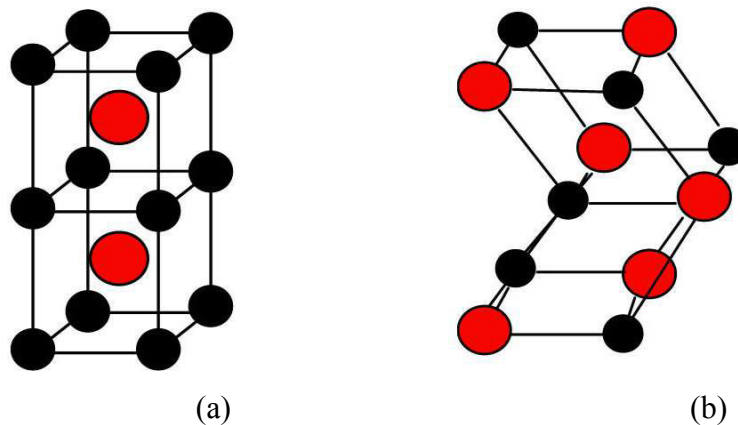


Figure 1.1: (a) Austenite and (b) Martensite lattice structures

The phase transformation mechanism can be activated in two different ways:

- Thermally induced (TIM, Thermally Induced Martensite);
- Stress induced (SIM, Stress Induced Martensite);

From an energetic point of view, the martensitic phase transformation is a solid phase transformation induced by the free energy (ΔG) difference associated to the martensitic and austenitic microstructure.

Figure 1.2 shows the free energy trends, for the austenitic (γ) and martensitic (α') structure, as a function of the applied temperature. In particular it is possible to observe that, for a specific value of temperature (T_0) the free energy difference of the system is zero, and the transformation phenomena can occur. For values of temperature lower

than T_0 the martensite is the stable structure while for temperatures higher than T_0 the austenite is the stable structure. In figure 1.2 the characteristic transformation temperatures of the alloy are also reported, in particular M_S and M_F are, respectively, the initial and final martensitic transformation temperatures while A_S and A_F are, respectively, the initial and final austenitic transformation temperatures, details will be given in a following section. An applied stress can support the martensitic transformation but the operating temperature has to be lower than a specific value called martensite start temperature due to deformation M_D ; higher than M_S .

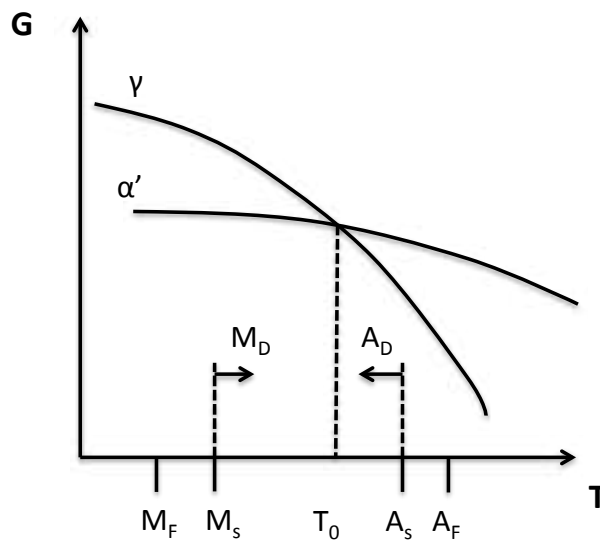


Figure 1.2: Free energy trends, as a function of the temperature, for the austenitic (γ) and martensitic (α') structure

The reason why there is a value of temperature M_D above which the martensitic transformation due to deformation does not occur is clearly justified in figure 1.3, where is plotted, as a function of the temperature, the transformation (τ_{sit}) and plastic (τ_{NP}) shear stress.

The transformation shear stress (τ_{sit}) increases with the temperature because the higher the temperature the lower the available ΔG needed for the process, that means an higher required shear stress to allow the martensitic transformation.

In this way it is possible to define M_D as the temperature above which an applied stress induces plastic deformation, while, below this value transformation mechanism can occur.

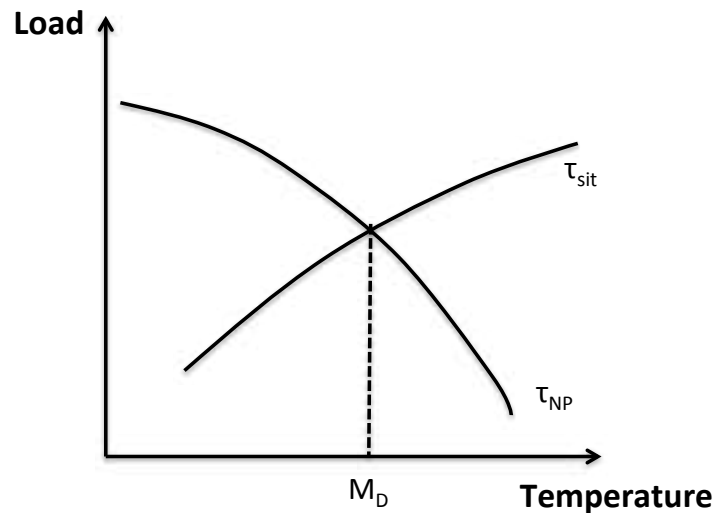


Figure 1.3: transformation (τ_{sit}) and plastic (τ_{NP}) shear stress as a function of the temperature.

From a crystallographic point of view, it is possible to define two kinds of solid state phase transformations: *diffusive* and *displasive* transformations. In diffusive transformations, the new phase is generated by means of big atomistic movements, with a consequent rupture of the crystal lattice. This phenomenon implies the generation of a new phase with a chemical composition different from the parent one. This kind of transformation depends on the time and temperature.

In dispalasive transformations, the atoms rearrange in a new crystal lattice, without changing the chemical composition of the parent phase. Since there is no atomic migration, the displasive transformations are time independent and, since the fraction of the new generated phase depends only on the reached values of temperature, this kind of transformation is also called athermal transformation.

In NiTi shape memory alloys, transformation does not occur by diffusion of atoms, but rather by shear lattice distortion. Such a transformation is known as martensitic transformation. Each martensitic crystal formed can have a different orientation direction, called a *variant*.

The assembly of martensitic variants can exist in two forms: twinned martensite, which is formed by a combination of “self-accommodated” martensitic variants, and detwinned or reoriented martensite in which a specific variant is dominant. The reversible phase transformation from austenite (parent phase) to martensite (product phase) and vice versa forms the basis for the unique behavior of SMAs.

Martensitic phase transformation is a consequence of two different contributes: *Bain Strain* and *Lattice Invariant Shear*.

Bain Strain is the crystal lattice deformation characterized by a series of atomic movements by which the new structure is generated. The complete transformation process is shown in figure 1.4. Starting from the austenitic structure (a), a very small movement is required for each atomic plane (b-c) in order to reach the final configuration of the martensitic structure (d). All these small movements are called Bain Strains.

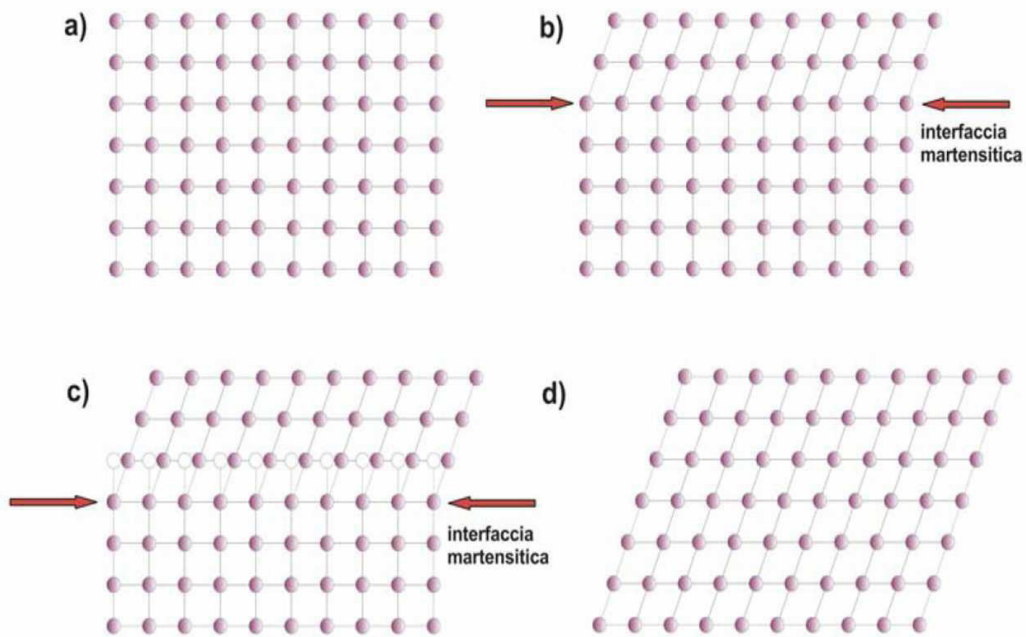


Figure 1.4: Bidimensional scheme of the phase transformation from a) austenite to d) martensite. As shown in the figure, the atomistic movement is short enough to avoid chemical bonds rupture

In the last part of the transformation, the lattice invariant shear, is an accommodation of the new generated structure (martensite), where shape and volume are usually different from the surrounding parent phase (austenite).

Typically, there are two different mechanisms by which the accommodation phenomena can occur: slip or twinning, figure 1.5. In both cases, the material is able to keep the same microstructure with the same lattice constants, but the twinning is a reversible process, while the atomic slip modifies, irreversibly, the microstructure of the material, due to the rupture of the atomic bonds.

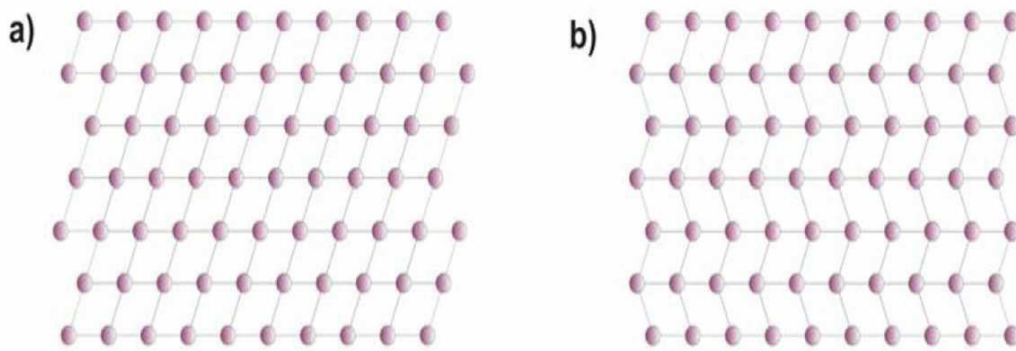


Figure 1.5: (a) atomistic slip e (b) twinning.

In shape memory alloys, twinning is the dominant accommodation mechanism. Twinning typically occurs along a specific plane called twin boundary, figure 1.6, that is a plane of symmetry where the resistance energy is very low and the atoms are free to move.

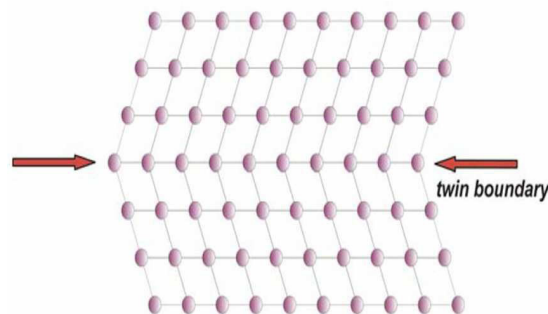


Figure 1.6: representation of a twin boundary.

Due to the peculiar properties of the twin boundary, figure 1.7, under the effect of an applied shear stress, the microstructure is arranged according to a preferential variant, the one whose orientation is more favorable to the applied load. This phenomenon is called detwinning and the final result is a macroscopic shape variation.

The phase transition from austenite to martensite is called *forward transformation*. The transformation results in the generation of several martensitic variants, up to 24 for NiTi. The arrangement of variants occurs such that the average macroscopic shape change is negligible, resulting in twinned martensite. When the material is heated from the martensitic phase, the crystal structure transforms back to austenite, and this

transition is called reverse transformation, during which there is no associated shape change.

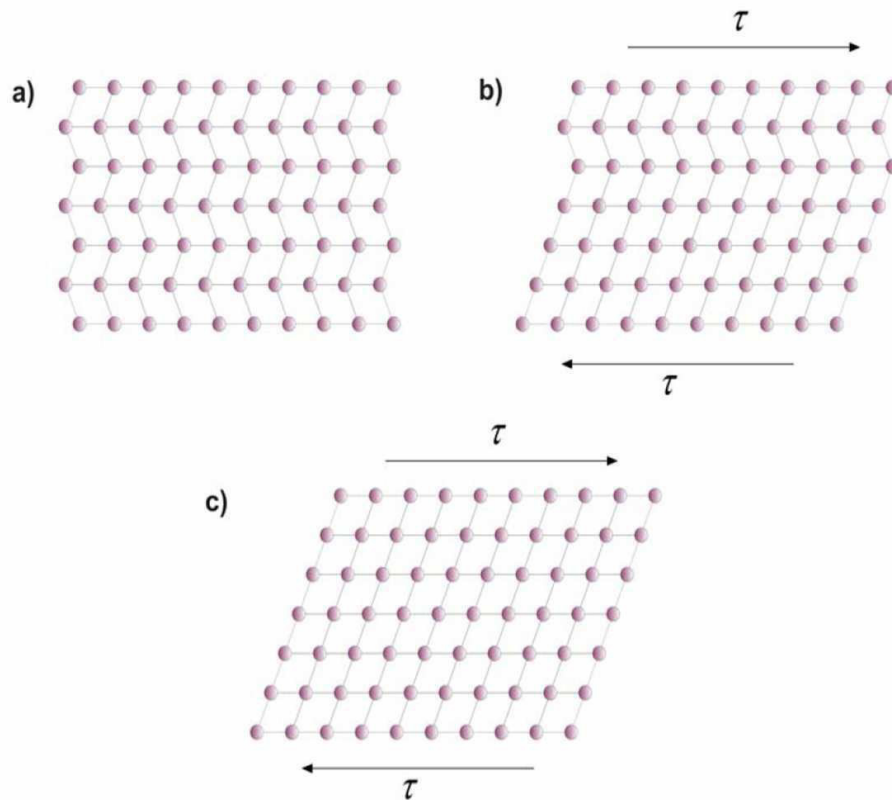


Figure 1.7: an applied stress generates a movement of the martensitic twin boundaries. The result is a macroscopic geometric shape variation.

A schematic of the crystal structures of twinned martensite and austenite for an SMA and the transformation between them is shown in figure 1.8. During the forward transformation, austenite, under zero load, starts to transform to twinned martensite at the martensitic start temperature (M_S) and completes transformation to martensite at the martensitic finish temperature (M_F). At this stage, the transformation is complete and the material is fully in the twinned martensitic phase. Similarly, during heating, the reverse transformation initiates at the austenitic start temperature (A_S) and the transformation is completed at the austenitic finish temperature (A_F).

If a mechanical load is applied to the material in the twinned martensitic phase (at low temperature), it is possible to detwin the martensite by reorienting a certain number of variants (see figure 1.9). The detwinning process results in a macroscopic shape change, where the deformed configuration is retained when the load is released. A

subsequent heating of the SMA to a temperature above A_F will result in a reverse phase transformation (from detwinned martensite to austenite) and will lead to complete shape recovery (see figure 1.10). Cooling back to a temperature below M_F (forward transformation) leads to the formation of twinned martensite again with no associated shape change observed. The process described above is referred to as the Shape Memory Effect (SME). The load applied must be sufficiently large to start the detwinning process.

In addition to thermally induced phase transformation, transformation can also be induced by applying a sufficiently high mechanical load to the material in the austenitic phase. The result of this load is fully detwinned martensite created from austenite. If the temperature of the material is above A_F , a complete shape recovery is observed upon unloading to austenite. This material behavior is called the pseudoelastic effect.

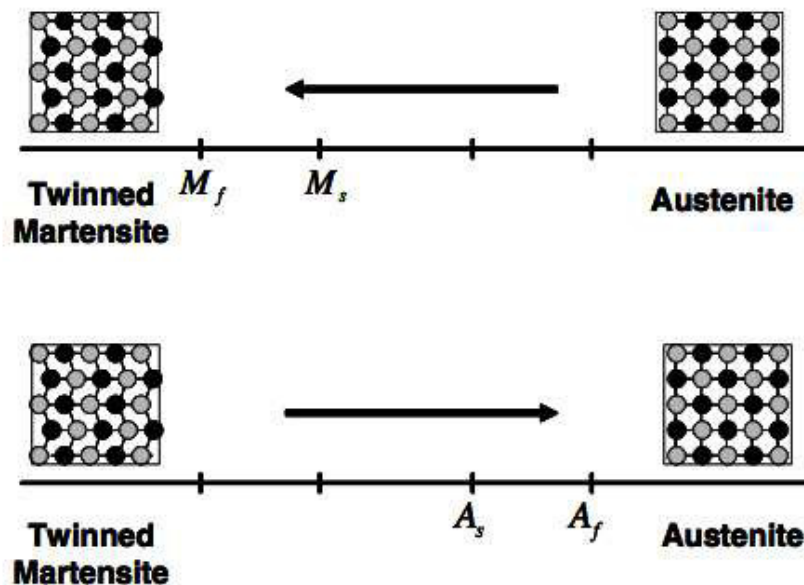


Figure 1.8: Temperature-induced phase transformation of an SMA without mechanical loading.

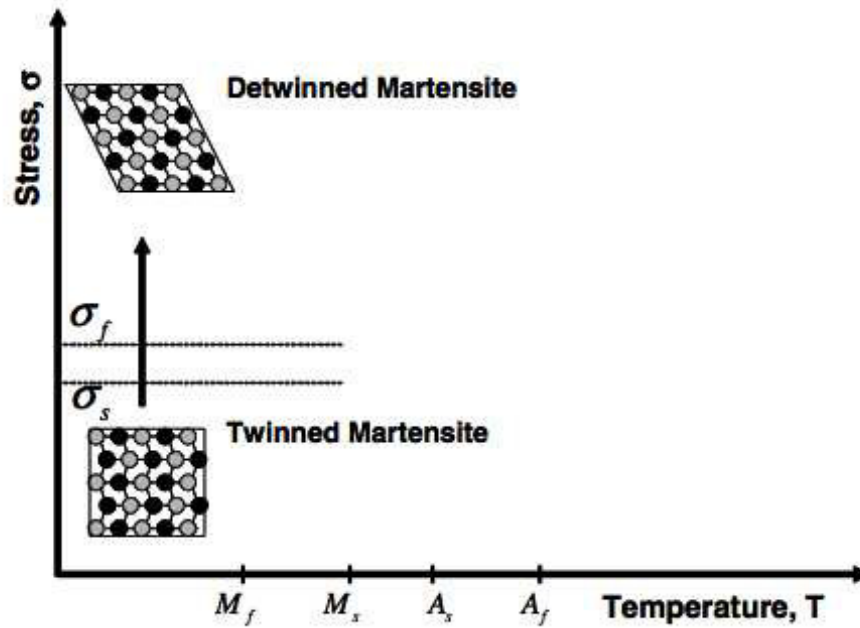


Figure 1.9: Schematic of the shape memory effect of an SMA showing the detwinning of the material under an applied stress.

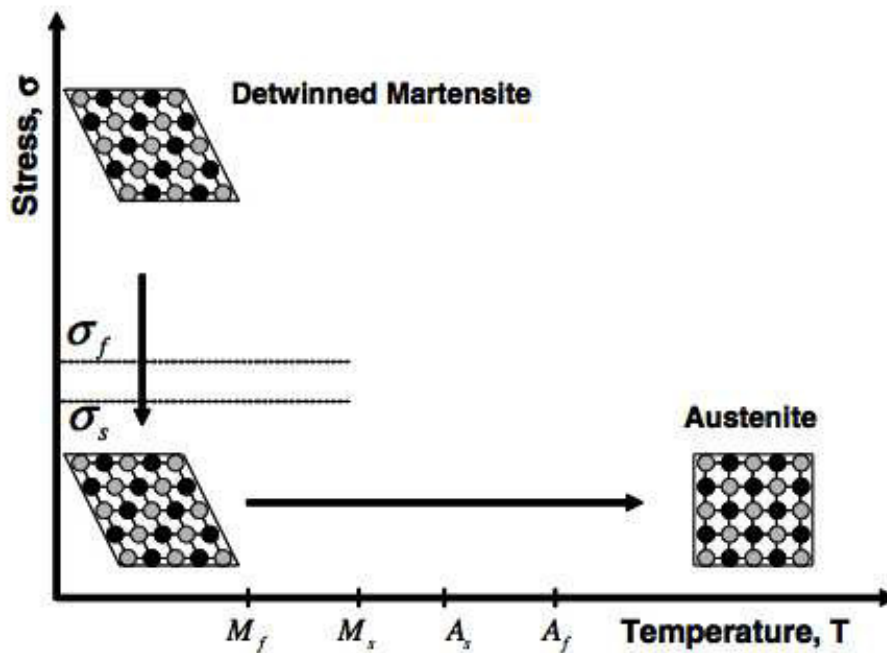


Figure 1.10: Schematic of the shape memory effect of an SMA showing the unloading and subsequent heating to austenite under no loading condition.

1.3 Characteristic Temperatures and Phase Transformations

A typical way to characterize the phase transformations and define the characteristic temperatures, is represented in figure 1.11. In particular, applying a constant load value and heating up and cooling down a sample, it is possible to get a hysteretic loop, shown in figure, in which the different phases of the material and the characteristic temperatures, that determine the beginning and the end of phase transformations, can be recognized.

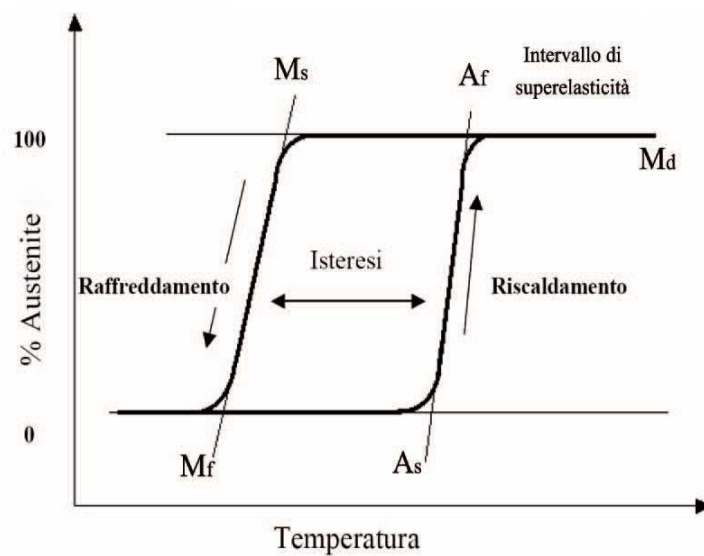


Figure 1.11: Hysteretic behavior obtained, under a constant applied stress, by heating and cooling a sample. The tangent lines allow to get the characteristic transformation temperatures.

In particular:

- **A_S**, or *Austenite Start*: heating, is the temperature at which the transformation from martensite to austenite starts.
- **A_F**, or *Austenite Finish*: heating, is the temperature at which the transformation from martensite to austenite starts.
- **M_S**, or *Martensite Start*: in cooling, is the temperature at which the transformation from austenite to martensite starts.
- **M_F**, or *Martensite Finish*: in cooling, is the temperature at which the transformation from austenite to martensite starts.

These temperatures are a function of the alloy composition, of machining processes and of the thermo-mechanical treatment conditions, and their interval can be more or

less wide. Looking at the sample with a microscope, it is possible to observe that by decreasing the temperature, martensitic plates start to generate gradually and with continuity. The same type of process occurs during the inverse transformation. The first plate of martensite that is generated at the M_S temperature is the last one to be transformed into austenite at the A_F temperature, and, vice versa, the last plate of martensite that is generated at the M_F temperature is the first one to return martensite at the A_S temperature [6].

The hysteresis depends on the alloy analyzed and its specific properties. In fact, even with very small variations in percentages of the different components, drastic effects on the transition temperatures that characterize the phase transformation of the alloy can be recorded. This is one of the most important engineering property of these materials, namely their capability to be applied in different phase transition temperatures depending on requirements previously defined. Furthermore, according to the operating temperature, the alloy manifests different mechanical behaviors, as showed in figure 1.12, where the NiTi stress-strain response, in different thermal conditions, is reported.

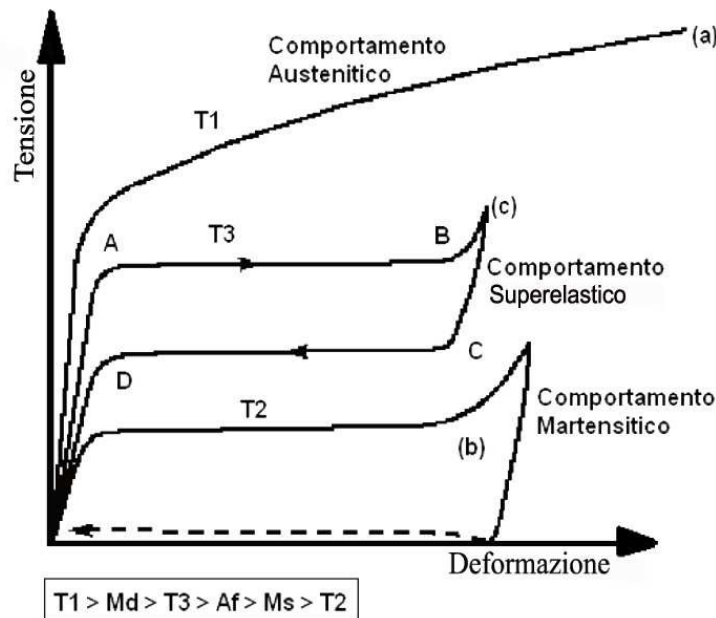


Figure 1.12: Stress-strain response obtained at different operating temperatures: (a) $T > M_D$, no martensitic phase transformation is recorded, the material is characterized by a stable austenitic structure and exhibits the typical behavior of a common engineering metal. (c) $A_F < T < M_D$ the material shows the pseudo-elastic behavior. (b) $T < M_S$ no martensitic phase transformation is recorded, the material exhibits a stable martensitic structure

For values of temperature below M_S , the material can be easily deformed with low stresses, and after unloading, the residual strain can be completely recovered by heating above A_F : in the final configuration the material is fully transformed in austenite recovering, from a macroscopic point of view, its original shape, as the dotted line shows in figure.

If the applied temperature lies in a range between A_F and M_D (as described before M_D is the temperature above which an applied stress induces plastic deformation, while, below this value transformation mechanism can occur) the material exhibits a pseudoelastic behavior: this means that the material after an applied load is able to completely recover deformations in the order of 10%.

No shape recovery is recorded if the operating temperature $T > M_D$. In these conditions, in fact, the material exhibits a pure austenitic behavior, i.e. common plastic slip mechanisms in the crystals, with no transformation phenomena, occur.

Figure 1.13 shows more clearly these behaviors as a function of the temperature.

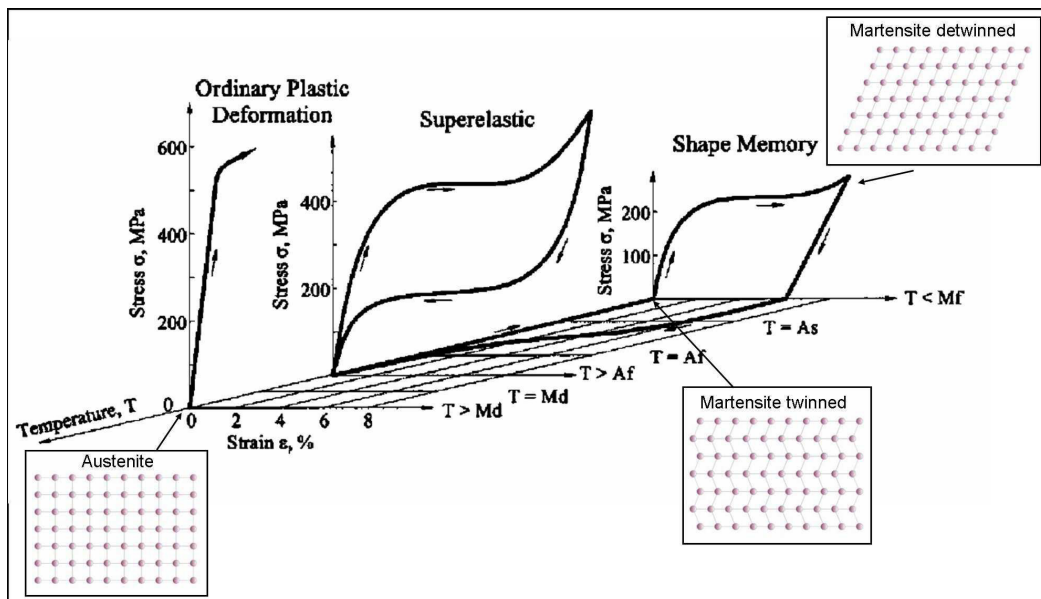


Figure 1.13: one way shape memory effect: thermomechanical cycle in a load-strain-temperature

1.4 Shape Memory Effect

1.4.1 One Way Shape Memory Effect

A SMA exhibits the shape memory effect (SME) when it is deformed while in the twinned martensitic phase and then unloaded while at a temperature below A_S . When it is subsequently heated above A_F , the SMA will regain its original shape by transforming back into the parent austenitic phase. The nature of the SME can be better understood by following the thermo-mechanical loading path in a combined stress-strain-temperature space as shown in figure 1.14. Figure 1.14 represents experimental data for a typical NiTi specimen tested under uniaxial loading. The stress σ is the uniaxial stress on the specimen due to an applied load. The corresponding strain ϵ is the change in the length of the specimen along the direction of applied load, normalized by the original length.

Starting from the parent phase (point A in figure 1.14), the stress-free cooling of austenite below the forward transformation temperatures (M_S and M_F) results in the formation of twinned martensite (point B). When the twinned martensite is subjected to an applied stress that exceeds the start stress level (σ_S), the reorientation process is initiated, resulting in the growth of certain favorably oriented martensitic variants that grow at the expense of other less favorable variants. The stress level for reorientation of the variants is far lower than the permanent plastic yield stress of martensite. The detwinning process is completed at a stress level, σ_F , that is characterized by the end of the plateau in the σ - ϵ diagram in figure 1.14. The material is then elastically unloaded from C to D and the detwinned martensitic state is retained. Upon heating in the absence of stress, the reverse transformation initiates as the temperature reaches A_S , (at E) and is completed at temperature A_F (point F), above which only the parent austenitic phase exists. In the absence of permanent plastic strain generated during detwinning, the original shape of the SMA is regained (indicated by A). The strain recovered due to the phase transformation from detwinned martensite to austenite is termed as the transformation strain (ϵ_t). Subsequent cooling to martensite will again result in the formation of self-accommodated twinned martensitic variants with no associated shape change, and the whole cycle of the SME can be repeated. The above described phenomenon is called one-way shape memory effect, or simply SME, because the

shape recovery is achieved only during heating after the material has been detwinned by an applied mechanical load.

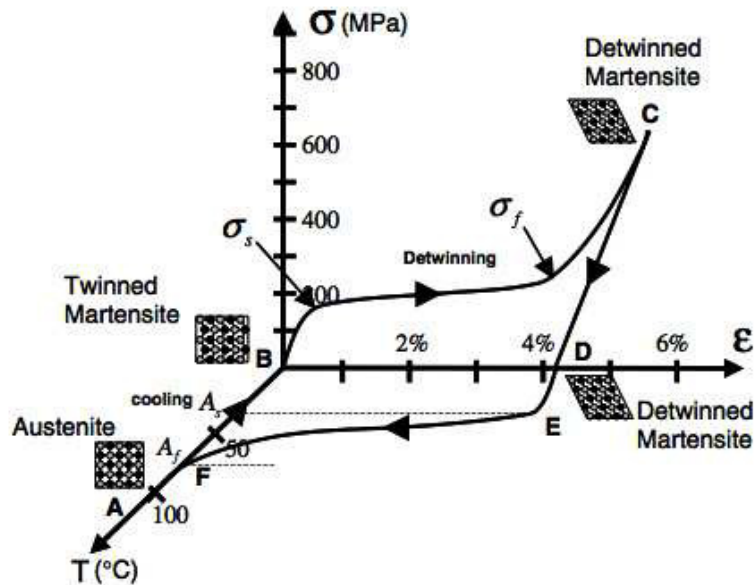


Figure 1.14: stress-strain-temperature data exhibiting the shape memory effect for a typical NiTi SMA

1.4.2 Two Way Shape Memory Effect

We have studied the one-way SME behavior in SMAs. Sometimes an SMA can exhibit repeatable shape changes under no applied mechanical load when subjected to a cyclic thermal load. This behavior is termed two-way shape memory effect (TWSME). The TWSME can be observed in a SMA material which has undergone repeated thermo-mechanical cycling along a specific loading path (training). Repetition along a loading path for a large number of cycles can induce changes in the microstructure, which causes macroscopically observable permanent changes in the material behavior.

Training an SMA refers to a process of repeatedly loading the material following a cyclic thermo-mechanical loading path until the hysteretic response of the material stabilizes and the inelastic strain saturates. Let us consider the case of cyclic thermal loading of an SMA specimen under a constant applied stress (figure 1.15). During the first thermal cycle, only a partial recovery of the strain generated during cooling is observed upon heating with some permanent (irrecoverable or plastic) strain generated

during the cycle. A small, permanent strain remains after each thermal cycle is completed. The additional permanent strain associated with each consecutive cycle begins to gradually decrease until it practically ceases to further accumulate (figure 1.15). A similar behavior can be noticed in the case of mechanically cycling an SMA repeatedly in its pseudoelastic regime, until saturation takes place (figure 1.16). The TWSME behavior can also be achieved by adopting different training sequences [7, 8]. A more recent technique that leads to TWSME deals with aging the material under stress in the martensitic state [9].

TWSME is a result of defects introduced during training. These permanent defects create a residual internal stress state, thereby facilitating the formation of preferred martensitic variants when the SMA is cooled in the absence of external loads. If the internal stress state is modified for any reason (e.g., aging at high temperature or mechanical overload), the TWSME will be perturbed [10].

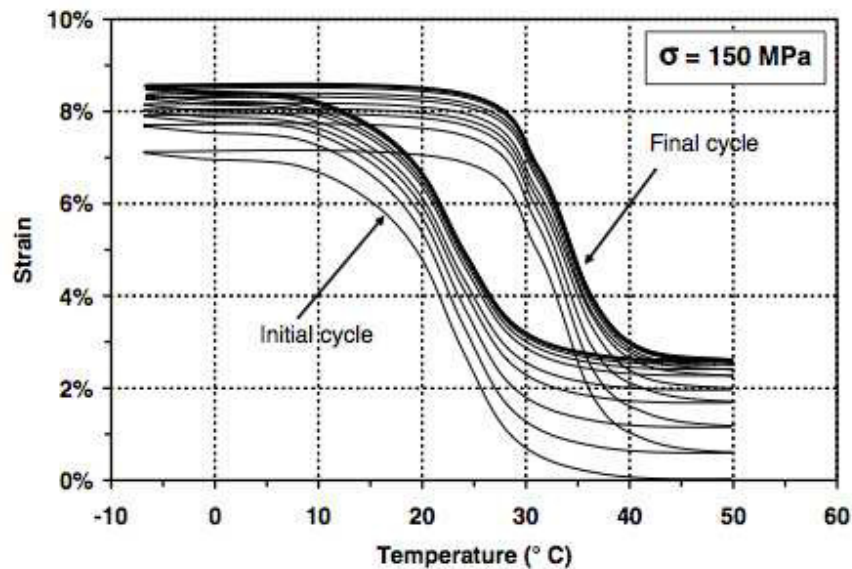


Figure 1.15: Thermal cyclic loading of a NiTi shape memory alloy under constant load of 150 MPa [8].

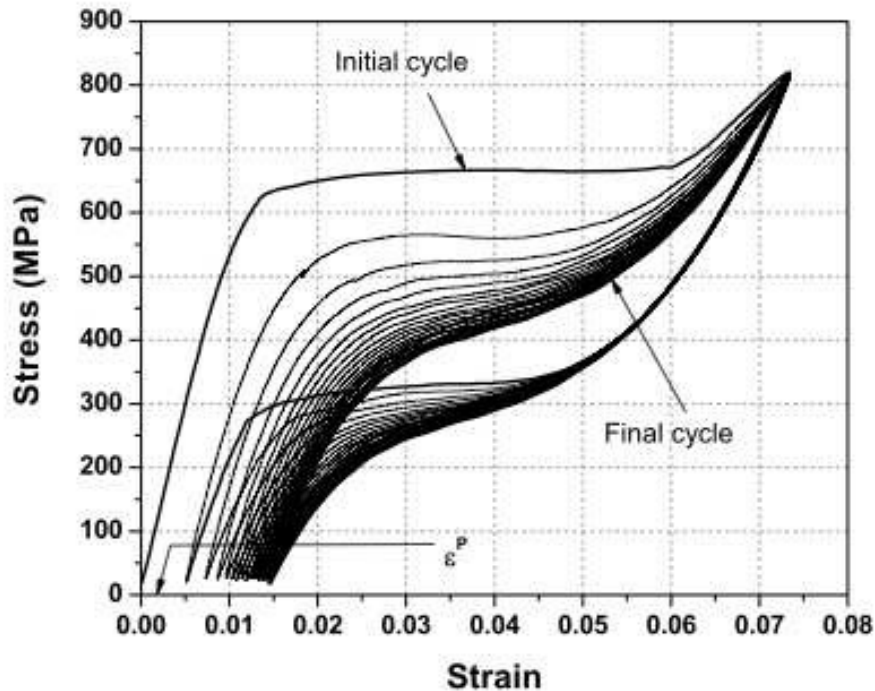


Figure 1.16: Pseudoelastic response of an as-received NiTi wire with $A_f = 65\text{ }^\circ\text{C}$, tested at a temperature of $70\text{ }^\circ\text{C}$. Also shown is the stabilized pseudoelastic hysteresis loop after 20 cycles.

1.5 Pseudoelasticity

The pseudoelastic behavior of SMAs is associated with stress-induced transformation, which leads to strain generation during loading and subsequent strain recovery upon unloading at temperatures above A_F . A pseudoelastic thermomechanical loading path generally starts at a sufficiently high temperature where stable austenite exists, then develops under an applied load to a state at which detwinned martensite is stable, and finally returns to the austenitic phase when returned to zero stress state.

To illustrate the pseudoelastic behavior in greater detail, let us consider the thermomechanical loading path ($A \rightarrow B \rightarrow C \rightarrow D \rightarrow E \rightarrow F \rightarrow A$) in figure 1.17, which starts at zero stress at a temperature above A_F . The corresponding σ - ϵ experimental data for the loading path is shown in figure 1.18. When a mechanical load is applied, the parent phase (austenite) undergoes elastic loading ($A \rightarrow B$). At a specific load level, the loading path intersects the surface for initiation of martensitic transformation on the phase diagram. This marks the stress level (σ_s^{AM}) for the onset of

transformation into martensite. Note that the stress-induced transformation from austenite to martensite is accompanied by the generation of large inelastic strains as shown in the stress- strain diagram of figure 1.18. The transformation proceeds (B → C), to the stress level (σ_F^{AM}) where the loading path intersects the M_F transformation surface, indicating the end of the transformation.

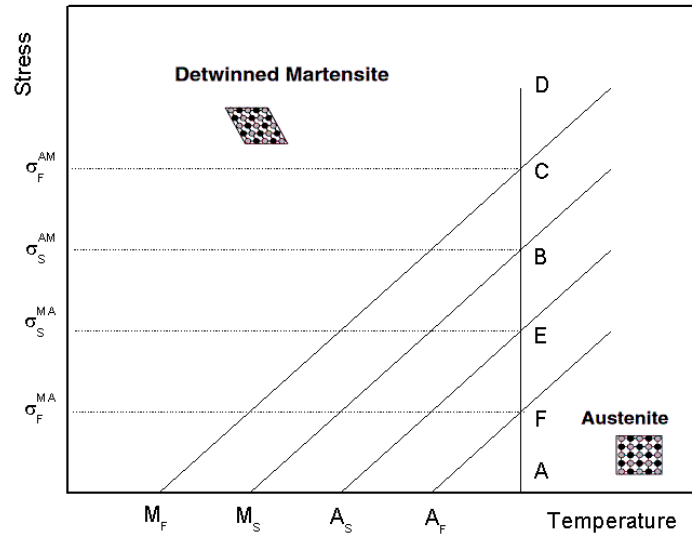


Figure 1.17: Phase diagram and two possible pseudoelastic loading paths.

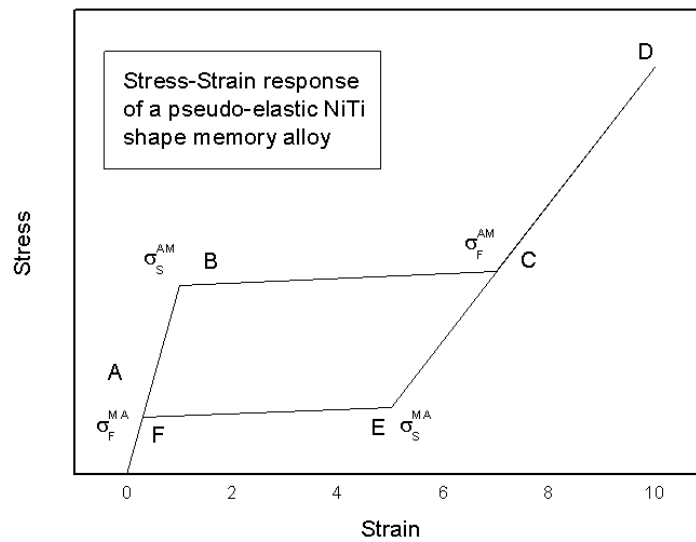


Figure 1.12: A typical SMA pseudoelastic loading cycle.

The completion of martensitic transformation is indicated by a distinct change in slope on the σ - ϵ curve, which is associated with the elastic loading of the martensitic phase. A subsequent increase in the stress causes no further transformation and only the

elastic deformation of detwinned martensite occurs ($C \rightarrow D$). When the stress is released gradually by unloading, the martensite elastically unloads along the path ($D \rightarrow E$). At point E, the unloading path intersects the austenitic start surface (at σ_s^{MA}), which causes the martensite to revert to austenite. The process is accompanied by the recovery of the strain due to phase transformation at the end of unloading. The end of the transformation back into austenite is denoted by the point at which the σ - ϵ unloading curve rejoins the elastic region of austenite (point F corresponding to stress σ_F^{MA}). The material then elastically unloads to A. The forward and reverse phase transformation during a complete pseudoelastic cycle results in a hysteresis, which, in the σ - ϵ space, represents the energy dissipated in the transformation cycle. The transformation stress levels and the size of the hysteresis vary depending on the SMA material and testing conditions.

The detwinned martensite that forms from austenite as a result of the applied stress during Path 1 or 2 in figure 1.17 is one form of stress-induced martensite (SIM). SIM, in general, is martensite that forms from austenite in the presence of stress. There are many thermomechanical loading paths that can result in the formation of SIM.

Generally, the term pseudoelasticity describes both superelastic behavior and so-called rubber-like behavior [11]. The reversible phase transformation (described in the previous paragraph) caused by a thermomechanical loading path is strictly called the superelastic behavior. The rubber-like effect is an exclusive behavior of the martensite phase only and occurs due to the reversible reorientation of martensite. In some cases, aging the martensitic phase can enable the reversal of the martensitic detwinning process upon unloading at temperatures below M_f . The resulting σ - ϵ curve is similar to the superelastic curve, and this phenomenon is called the rubber-like effect to emphasize the similarities with the nonlinear elastic behavior of rubber. In SMAs exhibiting the rubber-like effect, the stress required to detwin martensite is very small compared to σ_s^{AM} . We will not consider the rubber-like effect any further, and the term pseudoelasticity will refer to the superelastic behavior of SMAs only.

1.6 A More General Overview of Shape Memory Behavior

Thus far we have considered the SME and superelasticity as two separate effects. If stress is applied at intermediate temperature, however, between A_F and A_S , this may result in a combination of the two effects. To illustrate this idea, it is useful to consider a stress-temperature plot (see figure 1.19). In this plot, the line representing the critical stress to induce martensite, σ_s^{AM} has a positive gradient, since this stress increases with temperature, from the Clausius-Clapeyron relationship. The line representing the stress required to induce slip, σ_s , decreases with temperature, since dislocation motion becomes easier at higher temperatures, due to reduced energy barriers.

The SME is represented as a regime of temperature: stable martensitic variants can be induced by cooling below M_S , are unstable above M_S , and start to revert on heating above A_S . Superelasticity is similarly represented by any vertical line cutting through the superelastic region, in which the initial stress is insufficient to induce the martensitic transformation but, once a critical stress value is reached, unstable variants are formed that revert to the parent phase on removal of the stress.

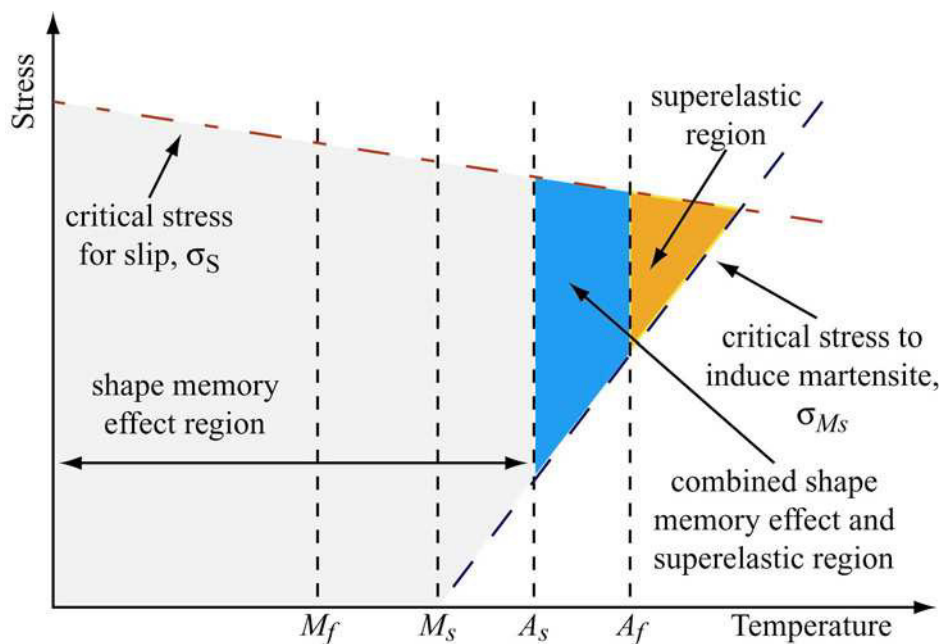


Figure 1.19: Stress-temperature plot for a typical shape memory system,

Figure 1.19 also demonstrates the potential for a shape memory material to exhibit the SME and superelasticity simultaneously. Increasing the applied stress above σ_s^{AM} ,

between A_S and A_F , will induce some stable and some unstable martensitic variants: only the unstable variants will revert to the parent phase, on removal of the applied stress, leaving some temporarily stable variants and some temporary deformation: these temporary variants will revert on increasing the temperature above A_F .

Figure 1.19 illustrates the key to superelasticity: for a material to exhibit such an effect, it must be possible for a stress to induce martensite formation preferentially to slip at temperatures above A_S . Thus, if, in Figure 1.19, σ_S were to equal σ_S^{AM} at a temperature below A_S , the material would exhibit no superelasticity, but could still exhibit the SME. This explains why all SMAs exhibit the SME, but only some of them exhibit superelasticity.

Clearly Figure 1.19 only represents the behavior of one specific SMA. The temperature A_S may in practice be below M_S and, from the discussion above, σ_S^{AM} may equal σ_S below A_S .

1.7 Main Shape Memory Alloys

1.7.1 Nitinol Shape Memory Alloy

Despite the discovery of the shape memory goes back to the '50s, the interest for SMAs, from an engineering point of view, was only recognized when the NiTi based alloy called Nitinol (Nickel Titanium Naval Ordnance Laboratory), from the name of the laboratory where it was discovered and studied [2], was discovered.

Over the past three decades, the NiTi binary alloys have been thoroughly investigated and today, from the commercial point of view, they are the most important, thanks to the excellent performances in terms of shape recovery and good mechanical properties. Moreover, these alloys have excellent corrosion resistance and excellent biocompatibility, which make them widely used in various biomedical applications. Finally, because it is pretty easy to make components in different shapes and sizes, they are technically usable for the realization of active elements in composite materials.

Their realization, however, is rather expensive for several factors: the heat treatment response is strongly dependent on the relative composition of nickel and titanium, and this requires a very high accuracy in selecting the composition. Moreover, due to the

reactivity of titanium at high temperatures, their realization requires extreme attention. Due to the high cost and the difficulties in realization, in the early seventies researches on alternative shape memory materials, starting from ternary NiTi based alloys, have been carried out.

1.7.1.1 The Nickel-Titanium System

As mentioned previously, there are many SMAs, but the nickel-titanium system is the only one to have achieved any real industrial success. This is a consequence of the remarkable combination of properties it exhibits. Not only is the magnitude of reversible thermoelastic deformation that nickel-titanium can cope with extremely large, but it is also possible for the transformation temperatures of this system to be controlled accurately, by careful thermomechanical treatment.

In all nickel-titanium systems, the SME is a result of the diffusionless transformation of the parent phase. The parent phase has the cubic (B2) structure and transforms either directly to the monoclinic (B19') martensitic phase or via an intermediate orthorhombic (B19) R-phase.

There are two main types of nickel-titanium SMA, based on either near-equiatomic nickel-titanium or nickel-rich nickel-titanium. Titanium-rich nickel-titanium can also exhibit shape memory effects, but such alloys have been less widely investigated. The mechanisms by which transformation temperatures are controlled differ substantially between these systems. There is clear evidence that changing the nickel concentration by 0.1 at% reduces the transformation temperatures of the alloy by up to 20K and examination of the phase diagram (see figure 1.20 and figure 1.21) shows that there is a transition from the extremely narrow stable NiTi region to the NiTi-Ni₃Ti region on increasing the nickel content very slightly above 50 at%, and similarly to the NiTi-NiTi₂ region on reducing the nickel content below 50 at%.

Some ternary nickel-titanium alloys also exhibit shape memory characteristics. The nickel-titanium system has a high solubility for a number of other elements, which are substituted either for nickel or for titanium, and result in alloys whose properties are substantially different from the parent material. Generally the ternary element is added to provide stability of some characteristic of the material e.g. a change to the

transformation temperatures, a variation in the hysteresis width or extra mechanical stability of the material.

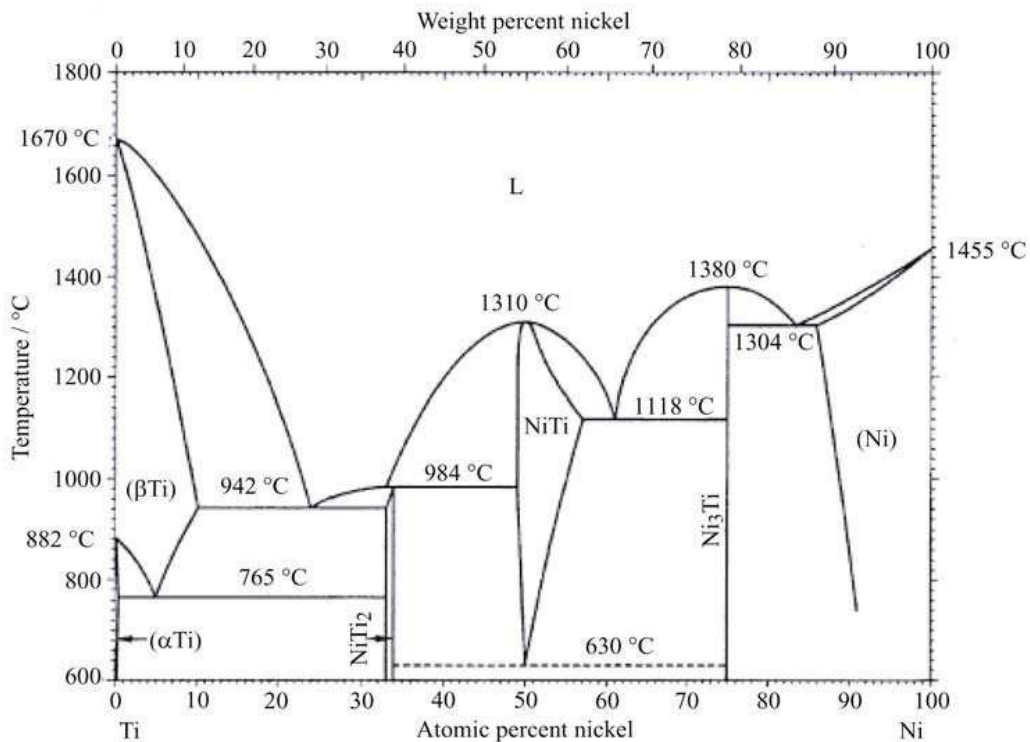


Figure 1.20: Nickel-titanium phase diagram: the region below 630 °C and around 50 at% Ni is expanded in Figure 2.12.

1.7.1.2 Near-equiatomic nickel-titanium

In order for a nickel-titanium system to demonstrate variation in its transformation behavior, some non-equilibrium stabilization or destabilization of the martensitic phase must occur. Close examination of the nickel-titanium binary phase diagram shows that a near-equiatomic nickel-titanium system is not able to exhibit any stabilizing precipitation effects (see figure 1.20 and figure 1.21), so any ability to vary its transformation temperatures must occur by some other mechanism.

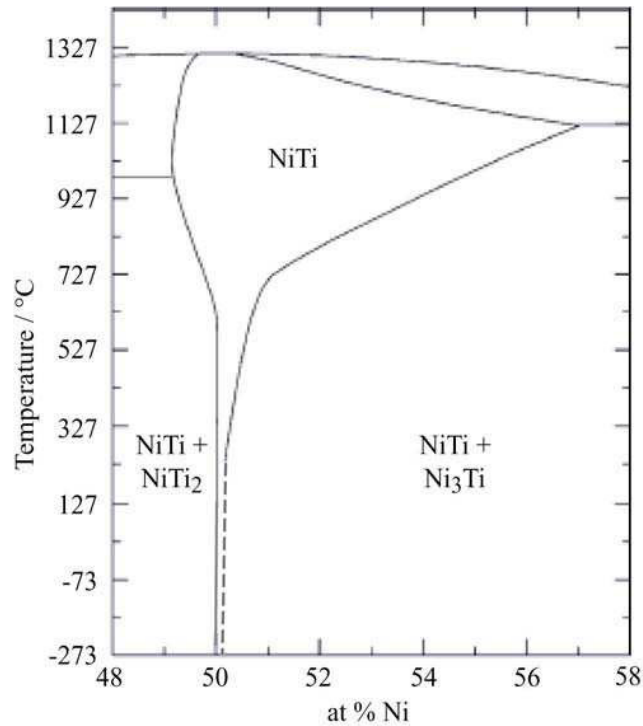


Figure 1.21: Expanded region of the nickel-titanium phase diagram, after Kompatscher et al.

Processing of nickel-titanium is often hampered by its high work-hardening rate. It is the presence of dislocations, in varying densities, that leads to the ability to carefully control the transformation temperature of near-equiatomic nickel-titanium. A high dislocation density raises the critical stress for slip and hence stabilizes the B2 phase to lower temperatures, by resisting transformation, hence reducing M_s . Simultaneously, however, these dislocations act as nucleation sites for the cubic parent phase, aiding reversion to the parent phase and lowering A_s by an equivalent amount. Even very slight variations in the density of dislocations can lead to an observable change in the transformation temperatures of the material.

As the dislocation density is increased, M_s will eventually be reduced to a sufficiently low level for the intermediate R-phase to form. This has been clearly demonstrated through the appearance of a second transformation peak in the cooling curve obtained using differential scanning calorimetry (see figure 1.22). Care must be taken when handling nickel-titanium that no extraneous stresses are applied during heat treatments and also that thermal cycling is not excessive. Under such stresses, a large presence of the R-phase may develop and this can result in reduction of the recoverable strain, by

limiting the martensitic variants that can form and hence forcing permanent variant formation. There is also the possibility of a build-up of plastic deformation through slip. One way of reducing such negative effects is to lower the anneal temperature, since this minimizes the matrix vulnerability to dislocation generation and motion and hence limits the presence of the R-phase in the final product, by retaining the one-step cubic to monoclinic transformation³⁶.

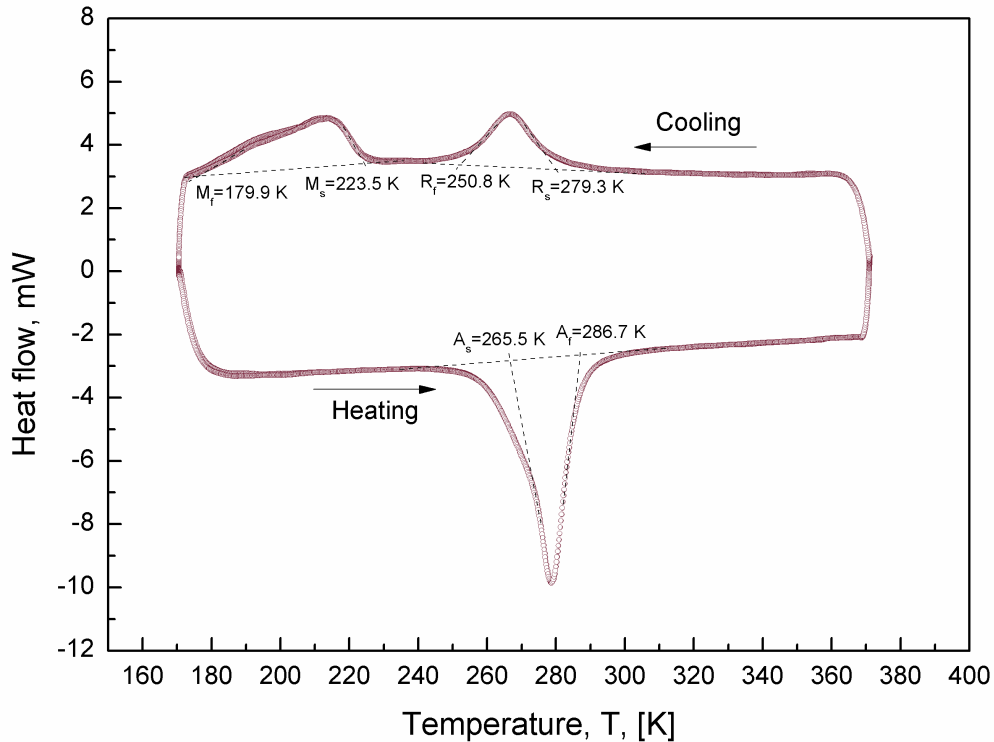


Figure 1.22: Differential scanning calorimetry plot demonstrating two-phase transformation on cooling via the R-phase.

The instability of near-equiatomic nickel-titanium alloys is therefore clear. The transformation temperatures of the material are governed closely by dislocation density, and this could easily be altered if the material were subjected to cyclic loading, or large temperature fluctuations. Despite these problems, or perhaps because of them, near-equiatomic nickel-titanium has extremely useful shape memory properties, which can be controlled by careful manipulation of processing conditions.

1.7.2 Alloys with Narrow Hysteresis

The partial replacement of copper atoms in nickel lattice location has interesting effects on the material properties, resulting in obvious advantages. Ternary Ti-Ni-Cu alloys exhibit a lower sensitivity to the temperature, an evident reduction of the hysteresis related to the transformation, from 30 K to less than 10 K, an increase of the damping capability, and finally a significant difference in stiffness between the martensitic and austenitic phase. These properties make them particularly advisable for the realization of actuators for intelligent systems [11].

1.7.3 Alloys with Wide Hysteresis.

The addition of niobium to the binary Ni-Ti alloys allows to decrease the start temperature of the martensitic phase transformation, and also to create a difference of 150 K between A_S and M_S .

Such a type of alloys are particularly suitable for the realization of coupling and attachment devices [12]. One of the most used alloy is Ti₄₃Ni₄₇Nb₉, where the numbers are referred to the percentages.

1.7.4 High Temperature SMAs

When the nickel, in a Ni-Ti alloy, is partially replaced by palladium, platinum or gold up to a percentage of 50% and the titanium is replaced by hafnium and zirconium up to 20%, the temperatures of martensitic transformation can be increased up to 873 K, keeping the shape memory effect [13].

These alloys, even if very expensive, are suitable for high temperature applications. The most studied alloy, because the most interesting from an economic point of view, is the Ni-Ti-Hf.

1.7.5 Copper Based Alloys

Although NiTi SMAs offer excellent pseudoelastic and SME properties and are biocompatible, they are relatively expensive compared to Cu-based SMAs. Good electrical and thermal conductivity along with their formability makes Cu-based SMAs an attractive alternative to NiTi. Copper-based alloys generally exhibit less hysteresis than NiTi, with the transformation temperatures in Cu-based alloys highly dependent on the composition. A precise change from 10^{-3} to 10^{-4} at.% is sometimes necessary to achieve reproducible transformation temperatures within a 5°C range. The main Cu-based alloys are found in the Cu-Zn and Cu-Al systems. In this section some of the most commonly used Cu based SMAs will be discussed.

CuZnAl - The CuZn binary alloys are very ductile and have resistance to intergranular fracture as compared to other Cu-based alloys [11]. These alloys transform to the martensitic state at a temperature below room temperature. Addition of aluminum to the binary alloy can considerably increase the transformation temperatures. Varying the composition of aluminum between 5 wt.% and 10 wt.% can shift the M_S temperature from -180°C to 100°C . However, the parent phase exhibits a strong tendency to decompose into its equilibrium phases when overheated or aged. Due to this, the operating temperatures are typically restricted to approximately 100°C . The transformation temperatures of the alloy are extremely sensitive to composition, and zinc can be lost during the melt process. Due to these factors, the fabrication process of the alloy needs to be precisely controlled. CuZnAl alloys are also very sensitive to heat treatments such that the quenching rate can lead to phase dissociation or change in transformation temperatures. Their mechanical behavior is limited to stress levels of approximately 200 MPa due to the low critical stress for slip. Within the operational range of stress, the alloy exhibits perfect SME and pseudoelasticity, but the transformation strain is limited to about 3-4% [11]. Since CuZnAl is very ductile as compared to other Cu-based alloys, they are mostly chosen for use in applications.

CuAlNi - CuAlNi is less sensitive to stabilization and aging phenomena. Similar to CuZnAl, the transformation temperatures of CuAlNi can be varied by changing the aluminum or nickel content. Changing the aluminum composition between 14 at.% and 14.5 at.% can change the M_S temperature from -140°C to 100°C . The relative change in transformation temperatures is not significant and the hysteresis remains

fairly constant. Since this alloy is harder to produce, manganese is often added to improve its ductility and titanium is added to refine its grains. However, the primary limitation of the CuAlNi system is the poor ductility due to intergranular cracking [14]. This phenomenon also affects the mechanical behavior such that the material typically fractures at a stress level of about 280MPa. Transformation strain in these materials is limited to 3%. The material also exhibits very poor cyclic behavior [14].

Developed later (1982), the CuAlBe alloy has been studied during the last few years. Recently, several other Cu-based SMAs are in development, such as CuAlMn which has good ductility and CuAlNb which is suitable for high temperature applications.

1.7.6 Iron-Based Alloys

FeNiCoTi and FeMnSi are the main ferrous SMAs. FeNi₃₁Co₁₀Ti₃ after specific thermomechanical treatment, exhibits SME. The alloy exhibits a thermal hysteresis of approximately 150°C.

Another ferrous alloy with good commercial prospects is FeMnSi. Si is primarily added to improve the shape memory effect and raise the critical stress for slip in austenite. When subject to training under a specific thermomechanical loading path, these SMAs exhibit complete SME. The transformation strains in these alloys are in the range of 2.5-4.5% [11].

1.8 Applications

There are several applications fields for SMA: starting from biomedical applications (orthodontic wires, dental implants, stents, orthopedic implants), to aerospace applications (smart wings for airplanes, couplings and fastening), from their use as actuators (for example in the automotive field), to the exploitation of their good damping capability (for example to realize seismic dampers).

In particular, the biomedical applications exploit the combination of biocompatibility (as demonstrated by various experiments conducted in vivo on the human body), strength and ductility.

Aerospace applications exploit the damping capability of SMA, in order to reduce the vibrations, obtaining a greater efficiency and a significant decrease of the noise in the surrounding environment.

The ability of SMA to work in the absence of gravity makes them particularly advisable for space applications.

The use of SMA as actuators exploits their capacity to make work by means of their shape memory effect: when subjected to an external load, they deform and keep this deformation until the external load is removed; if subsequently heated, they are able to recover their original shape thanks to a reverse phase transformation.

In particular, these alloys are suitable for applications in the automotive field, thanks to their simplicity and lightness.

Finally, especially in the civil field, several applications exploit the high inherent damping capability

1.8.1 Aerospace Applications

SMA technology implementation in the aerospace industry has spanned the areas of fixed-wing aircraft, rotorcraft, spacecraft and work in all these areas is still progressing. Some of the more recent applications of SMAs and research on their potential uses in these areas are described in the following sections.

Fixed-Wing Aircraft Applications - Perhaps two of the most well-known fixed-wing programs are the Smart Wing program and the Smart Aircraft and Marine Propulsion System demonstration (SAMPSON) [15]. The Smart Wing program represented a collaboration between DARPA, AFRL, and Northrop Grumman, and its purpose was to implement active materials, such as SMAs, to optimize the performance of lifting bodies [16]. In this program, SMAs were used as wire tendons to actuate hingeless ailerons and were also formed into torque tubes that initiated spanwise wing twist of a scaled-down F-18 aircraft wing.

There have been a number of other efforts to integrate SMA elements into aerostructures. One such study led to the development of a variable geometry airfoil. Through SMA actuation, this airfoil effectively changed its configuration from symmetric to cambered [17]. Many other studies on the utilization of SMAs in

aerostructures have focused on actuating smaller elements. SMAs can be used in smaller elements because their behavior is exhibited across a large range of sizes. One includes looking into the possibility of pairing SMAs and Micro-Electromechanical Systems (MEMS) to decrease the turbulent drag of an aerodynamic surface [18]. When activated appropriately, the MEMS skin would create a traveling wave to energize the boundary layer and thereby decrease turbulent drag. Some research has also been performed in the area of dynamic property optimization of aircraft structural panels using SMA elements, which provide a changing elastic stiffness via the martensitic transformation. It was found that the thermally-induced post-buckling deflection of a structure could be decreased by pre-straining the SMA or increasing the volume fraction of the SMA fibers [19]. The concept of a tunable SMA “Smart Spar” represented another attempt to alter the dynamic properties [20].

The usefulness of active materials in tailoring propulsion systems was demonstrated through the SAMPSON program [21]. One of the uses of SMAs in this program was to change the geometry of an F-15 engine inlet. A total force of approximately 26,700N was achieved through the use of SMA bundles containing 34 wires/rods. This generated force rotated the inlet cowl through 9°. Another concept tested by the SAMPSON program was the concept of changing the shape of the inlet lip through a more complex system of SMA actuation.

Engine noise levels during take off and landing have become more highly regulated worldwide. To reduce this noise, some designers are installing chevrons onto engines to mix the flow of exhaust gases and reduce engine noise. Research is being performed into methods by which SMA beam components can be embedded inside chevrons. The SMA beams bend the chevrons into the flow during low-altitude flight or low speed flight, thereby increasing mixing and reducing noise. During high-altitude, high speed flight, these SMA beam components will cool into martensite, thereby straightening the chevrons and increasing engine performance [22]. The current Boeing design for these variable geometry chevrons can be seen in figure 1.23.

A different solution to the active chevron problem has been proposed by NASA. In this design, SMA strips are installed on each side of the chevron centroid during the fabrication process [23]. Upon heating, the SMA strips contract alternately, leading to asymmetric stresses within the chevrons and therefore create a bending moment.



Figure 1.23: Boeing variable geometry chevron, flight testing [24].

Rotorcraft - The role of SMAs in rotorcraft applications has been focused on the main rotor [25]. One active research area is SMA blade twist actuation [26]. SMAs are ideally suited for such applications because of their high actuation energy density and forces required in the small available volume within a rotor blade. One study proposed the use of SMA torque tubes to vary the twist of rotor blades, as found on tiltrotor aircraft [27]. These SMA torque tubes, when actuated, could facilitate the formation of different blade configurations and thereby optimize performance of such aircraft in both the hover and forward flight regimes. Recent work has also been performed on developing SMA-actuated tabs to improve tracking [28]. A trailing edge tab actuated by SMA wires was built into an airfoil section to accomplish this improvement. Alternately, the Smart Material Actuated Rotor Technology (SMART) Rotor project team [29] proposed to link an SMA torque tube to the tracking tab. Other rotorcraft applications include using SMA wire components for collective control [30] and to provide rotor blade tip anhedral [31], which minimized the blade vortex interaction noise by moving the blade tip vortex away from the rotor plane.

Spacecraft Applications - SMAs have been used in space applications to address problems related to actuation and release in zero atmosphere environment as well as vibration damping during spacecraft launch. Most of the applications and systems are typically designed by careful experimentation. One such application that uses SMAs is for the low-shock release mechanism in satellites [32]. Until 1984, it was estimated

that nearly 14% of space missions experienced failure due to shock, and, in some cases, caused the mission to be aborted [33]. The shocks were caused due to pyrotechnic release mechanisms. The slow actuation due to gradual heating in SMAs makes them suitable for low shock release mechanisms in space applications. The scalability of SMA actuator designs also facilitates fabrication of smaller release devices for smaller satellites [34] in need of compact release mechanisms. Some of the devices developed for this purpose include the Qwknut [35] and the Micro Sep-Nut [34]. In both of these devices, the shape memory effect is used. Another miniature release device for space applications utilized a rotary actuation. The device, with a maximum dimension of 5mm, could provide a rotary actuation through an angle of 90°.

SMAs are also used in actuation of various components such as solar panels. An early design of this used SMA torsional elements to actuate solar collectors [25]. The Lightweight Flexible Solar Array (LFSA) [36] used thin SMA strips as hinges, which deploy the folded solar panels upon heating in approximately 30 seconds.

A different SMA space actuation application was utilized on the Mars Pathfinder mission in 1997. An SMA actuator was used to rotate a dust cover from a specific region of a solar cell so that the power output of this protected, and therefore clean area of the panel could be compared to the power output of non-protected regions. This determined the negative effects of dust settlement on the solar panels. In addition to actuation, another attractive application for SMAs is vibration isolators and dampeners [33]. The hysteresis in the pseudoelastic behavior is representative of the mechanical energy that an SMA can dissipate during a cycle. Further, the change in the stiffness from the initial elastic region to that in the transformation region makes it an effective tool to isolate vibrations.

1.8.2 Medical Applications

The shape memory and pseudoelastic characteristics coupled with the biocompatibility of NiTi make them an attractive candidate for medical applications. The combination of these unique characteristics has led to the development of various applications such as stents, filters, orthodontic wires as well as devices for minimally

invasive surgery (MIS).

An important requirement for an SMA, or any other material to be used in the human body, is that it be biocompatible. Biocompatibility is a property of the material to remain nontoxic through its functional period inside the human body. A biocompatible material can not produce any allergic reaction or inflammatory response in the host. The other requirement for the material is its biofunctionality, which is the ability to function desirably for its expected service life in the human body environment. These two requirements are crucial for the application of SMAs in the medical industry.

Several investigations have been performed to study the biocompatibility and biofunctionality of NiTi alloys [37-38]. Analysis has focused on each individual element that constitutes the alloy, namely, nickel and titanium. Nickel intake occurs in a regular lifestyle [39], and most often its impact at trace levels is minimal. However, excessive intake of nickel can be poisonous to the human body. Unlike nickel, titanium and its compounds are intrinsically biocompatible and are commonly used in orthopedic and orthodontic implants [40]. The oxidation of titanium results in a coating of TiO₂, which provides a corrosion-resistant layer, making such a device stable within the human body. Corrosion studies performed on NiTi alloys have shown better stability than most alloys used in medicine and dentistry [41]. It has also been shown that surface coating NiTi with TiN or TiCN is effective in further improving the corrosion resistance of this material.

Orthodontic Applications - The properties of SMAs have been successfully implemented in a variety of dental applications. Nitinol orthodontic archwires have been used since the 1970s [42], and are more effective than other alternative materials. In a linear elastic material like stainless steel, there is a large increment in stress, for a small increment in strain which results in a large amount of force on the tooth for a small amount of corrective motion. The advantage of pseudoelastic archwires is the ability to operate in the pseudoelastic plateau, during which the material has a near-zero stress change over a large strain increment. As a result, they provide a nearly constant, moderate force to actively move the teeth over a longer period of time compared with stainless steel. Further, the material composition and processing can be engineered to produce different levels of optimal force. An example of Nitinol orthodontic braces is shown in figure 1.24a.

Another key dental application for SMAs involves the use of Nitinol drills used in root canal surgery, which involves careful drilling within the tooth (figure 1.24b). The

advantage of these Nitinol drills is that they can bend to rather large angles, which induce large strains, yet still withstand the high cyclic rotations [43].

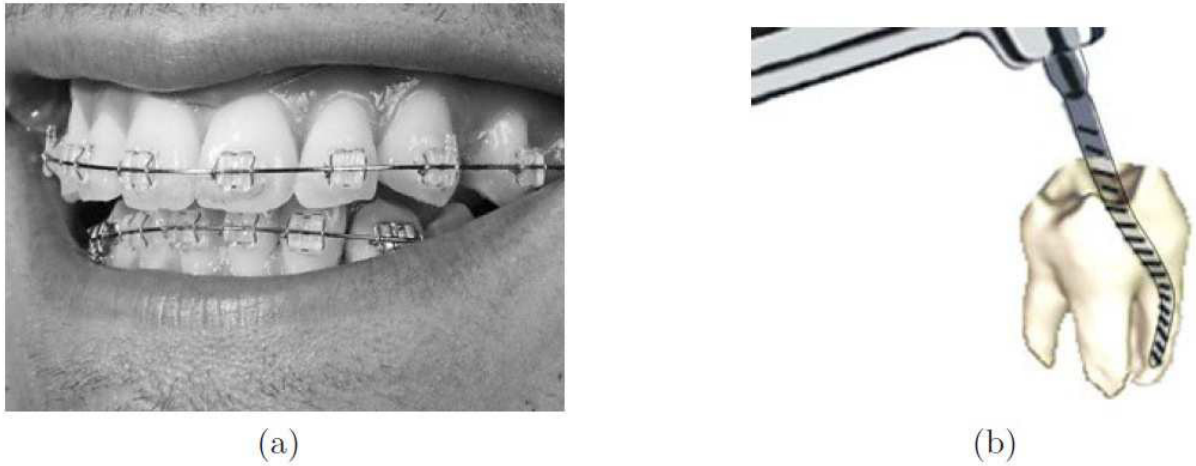


Figure 1.24: Orthodontic application of SMAs: (a) Nitinol braces used for alignment purposes in dental applications. (b) A schematic showing a NiTi drill used for root canal surgery.

Cardiovascular Applications - An early cardiovascular SMA device was the Simon Filter. The device acts as a filter that traps clots traveling in the blood stream. The trapped clots are then eventually dissolved. From the original expanded state, the device is deformed and constrained within a catheter. At the time of implantation, the filter is deployed in the blood vessel where the ambient temperature exceeds A_s of the filter material. The release from the constraint and the active properties of the SMA filter cause the filter to expand and it assumes its original shape as shown in figure 1.25a [44].

Another application of SMAs in the cardiovascular field is the atrial septal occlusion device. This device is used to seal an atrial hole that is located on the surface dividing the upper heart chambers. The traditional surgical technique used to address this problem is highly invasive and dangerous. The atrial septal occlusion device provides a suitable alternative to such a surgery. This device also exploits the shape memory characteristics exhibited by SMAs, and consists of two umbrella shape halves that can be screwed together in the center. Initially, these halves are folded, constrained and introduced into the heart. The two halves are deployed on either side of the hole and are connected using a screw. The resulting “sandwich” configuration forms a patch that seals the hole. A more common cardiovascular application is the “self-expanding”

NiTi stent. Like other conventional stents, this device is used to support the inner circumference of tubular passages in the body such as blood vessels. Traditionally, stents are made using stainless steel. These stents are expanded from the size of the introduced catheter to the size of the artery walls by an inflatable balloon. As the balloon is deflated, the steel stent undergoes elastic unloading, often resulting in a loose fit. Furthermore, to reach a particular nominal diameter, it is necessary to over-expand the stent to account for this unloading. This process of over-inflation can damage the vessels and can cause a condition where the blood vessel collapses after the procedure due to weakening of the walls. The self-expanding NiTi stents provide an attractive alternative to the traditional method. The device is generally laser cut from sheets or tubing and is then shape set to the appropriate diameter. After being constrained, the NiTi stent is introduced into the body where the temperature exceeds that of the stent material. It is then released in the artery where it expands to its original larger diameter and gently pushes outward on the walls. Furthermore, the device can adapt to any oblong passage as compared to the balloon inflated steel stents that are biased towards a circular shape. Figure 1.25b shows an illustration of a Nitinol stent in the constrained and deployed configuration.

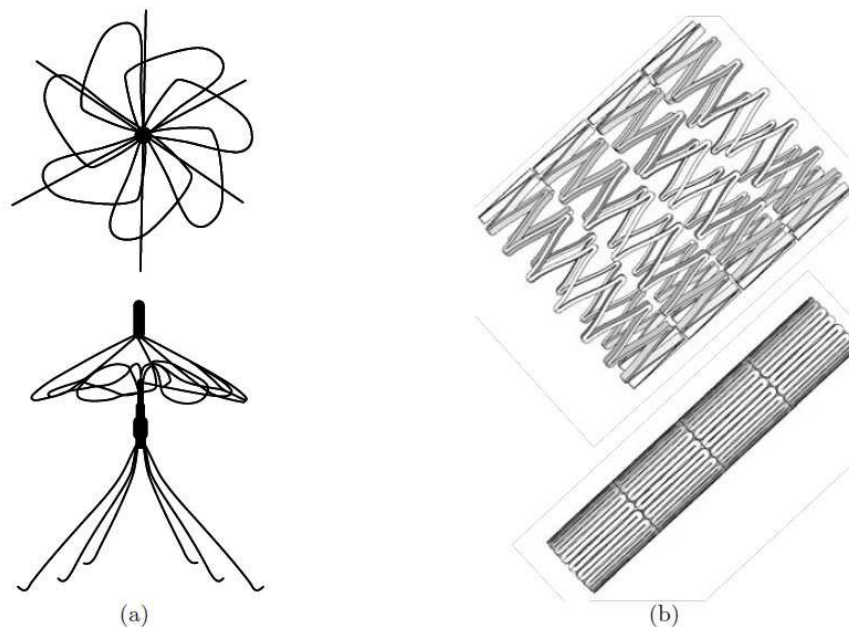


Figure 1.25: Cardiovascular devices that utilize the engineering properties of SMAs: (a) Top view (above) and side view (below) of the Simon filter in the deployed configuration [44]. (b) A self-expanding Nitinol stent shown in the deployed configuration (above) and constrained state (below).

Orthopedic Applications - The devices developed for orthopedic applications are used to support injured, weakened or fractured bones. One such device is the spinal vertebra spacer, used to provide local reinforcement to the vertebrae and prevent motion during the healing process. The device applies a constant force on the joint while providing flexibility [39].

Porous SMAs represent a different kind of material form and can be used as artificial bone implants [45]. The porous nature of the material enables the existing bone tissue to migrate inward, increasing bonding strength. Furthermore, the implant properties (stiffness and porosity) can be engineered to match those of the bone. In a separate application, SMAs fasten to broken or fractured bones to facilitate healing. These devices include orthopedic staples and shape memory plates. The staple, for example, is installed in an open configuration at the fractured joint. An external heating source is used to heat the staple causing it to return to its original form via SME, which consequently provides a compressive force at the interface of the separated bones [39]. The shape memory plate is a device used when a cast cannot be applied over the fracture surface (i.e. facial areas, jaw, nose). The plate is also “shape set”, deformed, installed and then actuated via (external) heating, providing a force which holds the fractured joints together [39].

Surgical Instrument Applications - Advances in medicine continue to enhance the use of minimally invasive surgery (MIS). Some of the enabling technologies advancing MIS includes instruments that can be inserted through these small openings followed by expansion to a desired size for the particular function. The pseudoelastic and shape memory effect properties of SMAs allow for more creative design options compared to conventional materials. One such device is the SMA basket used to remove stones in the bile duct. Other instruments using the shape memory effect behavior include surgical tools with grippers, scissors and tongs used in laparoscopy procedures. Pseudoelastic guide wires are widely used in surgery due to their kink resistance and superior flexibility [44].

1.8.3 Transportation Applications

Shape memory alloys have been used in automobiles for applications ranging from impact absorption to sensing and actuation. The pseudoelastic behavior hysteresis provides an effective system to dissipate vibrations and impact. This property has been used for impact absorption on armor vehicles in military [46] and commercial applications [47]. One design for an impact absorption application required the deployment of a protective panel within 5-7 ms. The limited response time of commercially available actuation devices (10 ms) is overcome by the use of an SMA element. The device can be released in 3 ms and then reset for another actuation. The SME has also been implemented for actuating blinds that cover the fog lamp to prevent damage. A series circuit ensures the actuation of the SMA louvers every time the fog lamps are turned on. SMAs can also be used for sensor and actuation purposes simultaneously. An application that exploits this behavior is the SMA spring for the continuous variable transmission in the Mercedes A class. The spring acts as a sensor that monitors the temperature and actuates a valve at a specific temperature, which changes the direction of oil flow.

A similar actuation system is incorporated in the Shinkansen bullet train gearbox where the temperature in the gear box is monitored and an SMA spring actuates a valve to adjust the oil level in the gearbox [48]. Other applications developed for trains include the thermally actuated switch for the radiator fan in diesel engines and steam traps for the steam heating system in passenger trains. Both of these applications utilize the shape memory effect.

1.8.4 Other Applications

In addition to the aerospace, transportation and medical industries, there are many other fields and applications that incorporate SMAs. The oil industry has shown extensive interest to use the SMA actuation capabilities in release devices and protection systems for downhole drilling equipment. The high operating conditions have also opened the avenue for the use of HTSMAs in these devices [49]. Everyday applications such as coffee makers and rice cookers have also incorporated SMAs. A

rice cooker equipped with an SMA valve has the valve actuate when the cooker reaches a certain temperature and releases the excess steam in the chamber. SMA actuated louvers have also been incorporated in air conditioning vents that can adjust depending on the temperature of the air exiting the vents. The SME is also utilized in shower faucet designs where an SMA spring automatically adjusts the flow of hot and cold water to maintain a preset water temperature [50].

The pseudoelastic behavior has also been used in a wide range of applications. Developers of vibration control devices in civil structures have shown interest in pseudoelastic behavior of NiTi due to its capability to dissipate energy through a large hysteresis [51]. Other applications that employ the pseudoelastic behavior are flexible metallic eyeglasses and headphones, that can be bent without breaking [52]. SMAs have also been used in sporting goods like golf clubs where the SMA embedded in the club absorbs the impact of the strike. Figure 1.26 shows a picture of a pseudoelastic eye glass frame and a golf club with a pseudoelastic SMA embedded in it.

In a recent study, an innovative approach of knitting SMA wires into different patterns has shown to produce complex shape changes such as rolling, spiraling, arching and folding [53]. The ability to generate such unique configurations using SMAs can open prospects for other novel design applications.

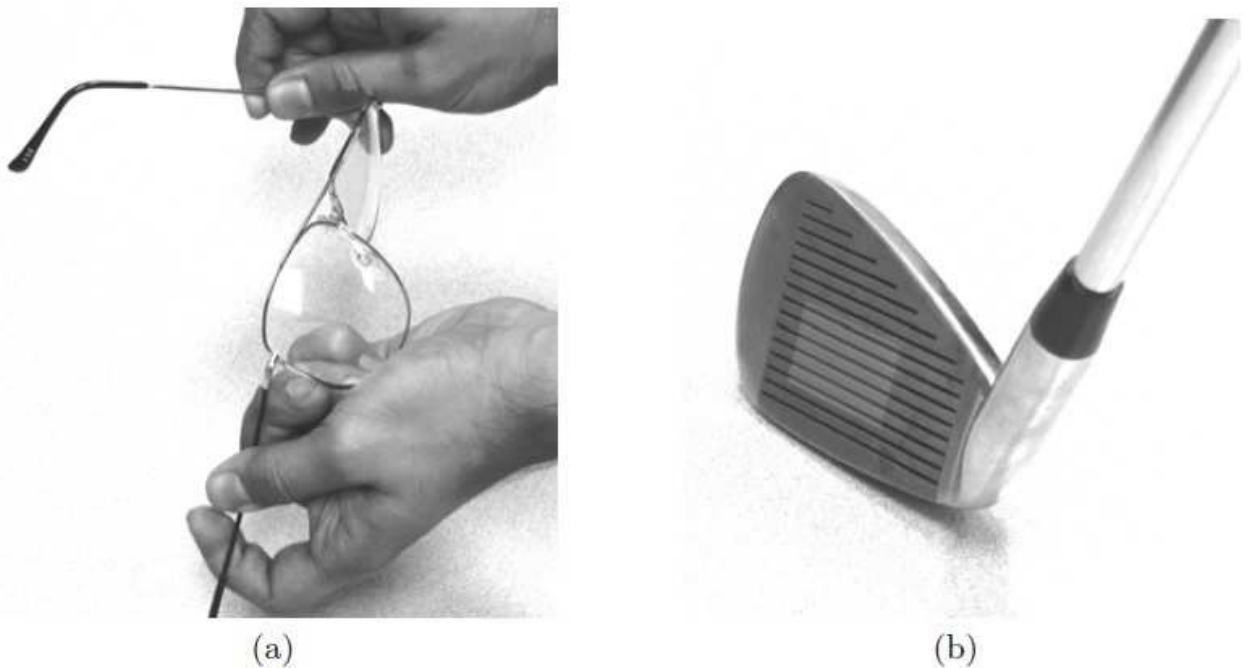


Figure 1.26: Commercial pseudoelastic applications of SMAs. (a) Pseudoelastic eye glass frames. (b) Golf club with embedded pseudoelastic SMA insert.

CHAPTER 2

FATIGUE OF PSEUDOELASTIC NITI WITHIN THE STRESS-INDUCED TRANSFORMATION REGIME

2.1 Introduction

The use of Nickel-Titanium based shape memory alloys (SMAs) is continuously increasing in many braches of engineering and medicine due to their good functional properties, mechanical performance and biocompatibility [54]. However, despite this increasing interest the use of NiTi alloys is currently limited to high-value applications due to their complex material processing and component manufacturing. In addition, NiTi alloys exhibit unusual fracture and fatigue responses, if compared with common engineering metals, due to their stress-induced and/or thermally-induced microstructural evolutions. As a consequence, well known theoretical models and standard testing procedures, to analyze the nucleation and propagation of cracks under fatigue loads, cannot be applied to SMAs. Moreover, NiTi alloys are currently employed in the shape of wires, tubes or sheets and their functional and mechanical properties are significantly affected by their own thermo-mechanical processes. For this reason the properties of commercial semi-finished NiTi products can be regarded as the result of the chemical composition, processing and training of the material. As consequence, non-standard specimens and testing procedures should be developed to study the cycling properties of SMAs, with the aim of using commercial semi-finished products, instead of standard bulk fatigue specimens.

Starting from the pioneer work by Melton and Mercier [55], who analyzed the functional and structural fatigue properties of NiTi based SMAs several researches have been focused on the fatigue properties of SMAs [56-57], by using non-standard specimens and testing procedures. In particular, in most of these works the cyclic behavior of NiTi wires [58-72], subjected to strain controlled axial loading [58-64] and rotating bending conditions [65-72] have been analyzed. In these studies the effects of the wire diameter, material processing conditions as well as the environmental and loading conditions have been investigated. In particular an interesting work has been done by Wagner et al. [68], where the effect of the wire diameter, in terms of fatigue

Fatigue of Pseudoelastic NiTi within the Stress-Induced Transformation Regime

life resistance, has been investigated by performing bending rotating tests, figure 2.1. Results haven't shown a marked effect of the geometry in the material life resistance, even though the dispersion of data is higher for high values of the applied strain than for the lowest ones. The reason of this behavior has been related to the more evident transformation phenomena that occur in the low cycle fatigue regime.

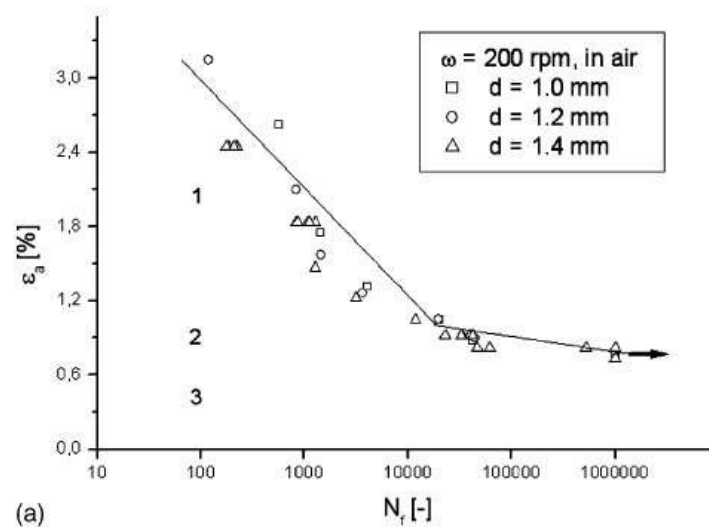


Figure 2.1: fatigue life resistance of NiTi wires tested by bending rotating tests and characterized by different wires diameters [68].

The effect of the temperature, combined with the one of the operating environment, has been investigated in [65]. Results, figure 2.2, show that in the low cycle regime the material exhibits higher resistance in water as a consequence of the higher efficiency of the thermal exchange during the loading and unloading path; on the contrary for the lowest applied strain the material exhibits higher resistance in air due to the eventual corrosion phenomena that can occur after a certain number of loading cycles.

In all the studied cases NiTi manifests, in terms of fatigue life resistance, the typical behavior of a common engineering metal; however an unusual response (“z-shape”) has been obtained by Figueiredo et al. [70], figure 2.3. In particular, from their tests, the pseudoelastic material exhibited, for applied deformation ranged from 4% to 8%, an increase of the resistance approaching the response of the stable martensite, for the highest values of the applied strain, and of the stable austenite, for the lowest values of the applied strain, and the martensitic phase showed a higher resistance than the austenitic one.

Fatigue of Pseudoelastic NiTi within the Stress-Induced Transformation Regime

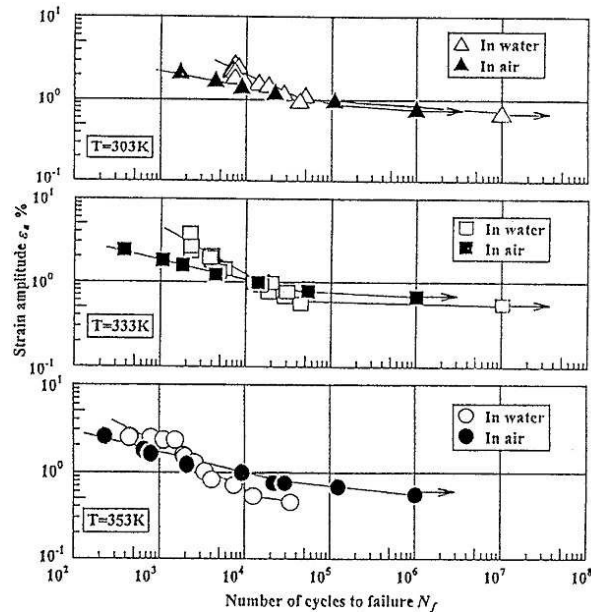


Figure 2.2: fatigue life resistance of NiTi wires tested by bending rotating tests at different temperatures and operating environment [65].

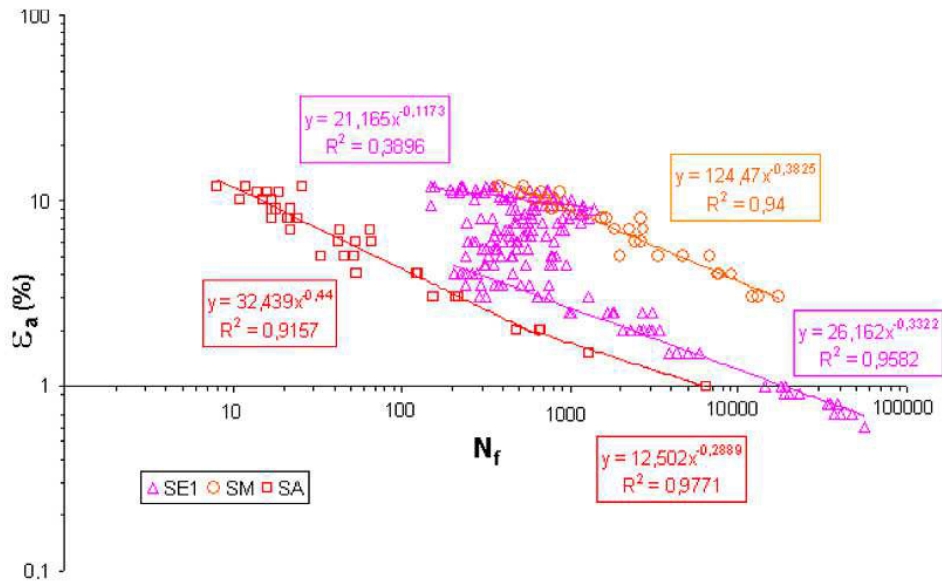


Figure 2.3: fatigue life resistance of NiTi wires, characterized by a different phase, tested by bending rotating tests [70].

In other recent researches the fatigue properties of SMA bars and tubes have been analyzed [73-82], in terms of functional fatigue [73-75], *i.e.* the evolution of pseudoelastic response under and cyclic loads, crack propagation [76-78] and fatigue life estimation [79-82], and the effects of biaxial loading conditions have been also studied by applying axial loads, bending and torsion [81]. These studies provided very

Fatigue of Pseudoelastic NiTi within the Stress-Induced Transformation Regime

interesting results since NiTi tubes are typically employed for the manufacturing of endovascular stents. Moreover, in order to better investigate the fatigue properties of such components, diamond-shaped samples were studied [83-84], with a geometry very close to the unit cell of a stent, figure 2.4. Furthermore, other studies have been devoted to the analysis of the functional fatigue of single crystal NiTi alloys [85-86] by using special test specimens, which have been cut along different crystallographic orientations.

In particular, fatigue resistance and functional evolution, for different orientations, were investigated in [85], figure 2.5, while the influence of different heat treatments and of precipitates, were studied in [86].

Finally, a few works have been carried out to analyze the fatigue properties of NiTi sheets [87-90].

However, disagreements have been found between the results of these researches, which can be attributed to several causes such as: *i*) material processing conditions, *ii*) specimen geometry and dimensions and *iii*) loading and environmental conditions. Due to these reasons a direct transferability of the results to the engineering community is not possible, as only a few models have been proposed for fatigue lifetime estimation but, unfortunately, their general applicability must be proved by systematic experimental studies. In particular, in a recent study the fatigue properties of NiTi alloys has been analyzed under the framework of Coffin-Manson approach [81], by defining an equivalent strain obtained from different multiaxial loading conditions. Furthermore, an energy approach has been proposed in [82] where the dissipated energy of the pseudoelastic hysteresis cycle is used as a parameter for lifetime estimation.



Figure 2.4: NiTi diamond shaped specimen [84].

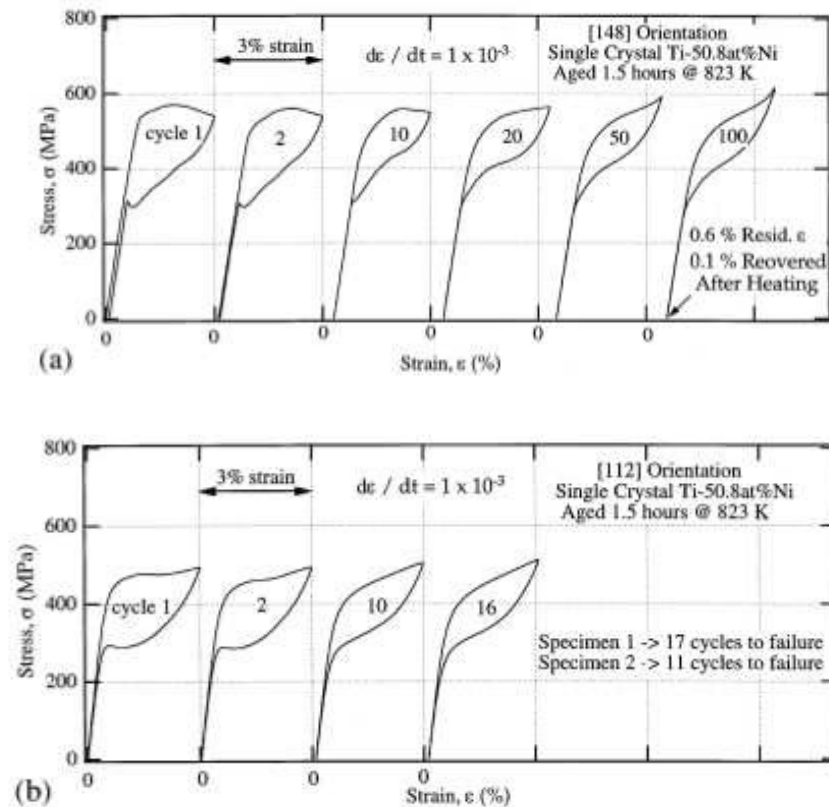


Figure 2.5: Constant amplitude tests for the (a) [148] orientation, (b) [112] orientation [85].

Within this context, in this chapter is presented a study focused on the low cycle fatigue of a pseudoelastic NiTi sheet in the stress-induced transformation regime, *i.e.* with maximum deformations within the transformation plateau of the alloy. Results on both functional and structural fatigue are reported and discussed. In particular, the evolution of the pseudoelastic response of the alloy in the first transformation cycles has been analyzed by preliminary fatigue tests, in order to stabilize the stress-strain behavior of the SMA, in terms of both recoverable and residual strain, and to identify the evolution of several functional damage parameters, involving strain, energy, transformation stress, Young's modulus and phase transition temperatures. In fact, a cyclic creep-like mechanism, the so called ratchetting [91], occurs in NiTi alloys during repeated stress-induced transformation cycles, mainly due to the formation of stabilized martensite [73-74, 85-86], which causes an increase of mean strain up to a stable hysteretic response. Subsequently, strain controlled fatigue tests of the stabilized material have been carried out and the number of cycles to complete failure have been recorded. Finally, a novel strain-life approach is proposed, which takes into account the different strain mechanisms involved during stress-induced transformation in SMAs,

Fatigue of Pseudoelastic NiTi within the Stress-Induced Transformation Regime and the experimental results have been used to obtain the model parameters.

2.2 Materials and Experiments

A commercial pseudoelastic NiTi sheet (Type S, Memry, Memory metalle Germany), with nominal chemical composition of 50.8at.% Ni - 49.2 at.% Ti and with thickness $t=1.5$, has been investigated. The material has been preliminary analyzed by isothermal tensile tests and differential scanning calorimetry (DSC). In particular, figure 2.6 illustrates stress-strain curve of the *as received* material obtained from an isothermal ($T=298$ K) loading-unloading cycle up to complete stress-induced martensitic transformation corresponding to a The figure also shows the values of the main thermo-mechanical parameters of the alloy, in terms of Young's moduli (E_A , E_M), transformation stresses (σ_s^{AM} , σ_f^{AM} , σ_s^{MA} , σ_f^{MA}), transformation strain (ϵ_L) and Cluasius-Clapeyron constants (C_A , C_M). These latter parameters were obtained from isothermal tensile tests carried out at different values of the temperature. Figure 2.7 illustrates a Differential Scanning Calorimetry (DSC) curve of the *as received* material which was performed over a temperature range between -100°C and 100°C using a heating/cooling rate of $10^\circ\text{C}/\text{min}$ (DSC Seiko 220C). The graph clearly shows a two-stage direct transformation from high temperature parent phase (B2) to rhombohedral phase (R) to low temperature stable phase (B19'). In contrast, a one-stage inverse transformation B19'-B2 characterizes the heating branch of the curve. This is a typical curve of NiTi after aging, indeed the formation of Ti_3Ni_4 precipitates are responsible of the change of the transformation path from B2-B19' to B2-R-B19' [54].

Dog bone shaped specimens, with gauge length of 10 mm, have been made from as received sheets, by wire electro discharge machining, with the rolling direction axis of the specimen, as illustrated in figure 2.8. A successive polishing procedure of the machined surfaces was carried out, by sandpapers with progressively finer grits (#400-#1200) and diamond compound (5 mm), to reduce the surface roughness and local surface damages, which represent preferable sites for crack nucleation and propagation under mechanical cycling.

Fatigue of Pseudoelastic NiTi within the Stress-Induced Transformation Regime

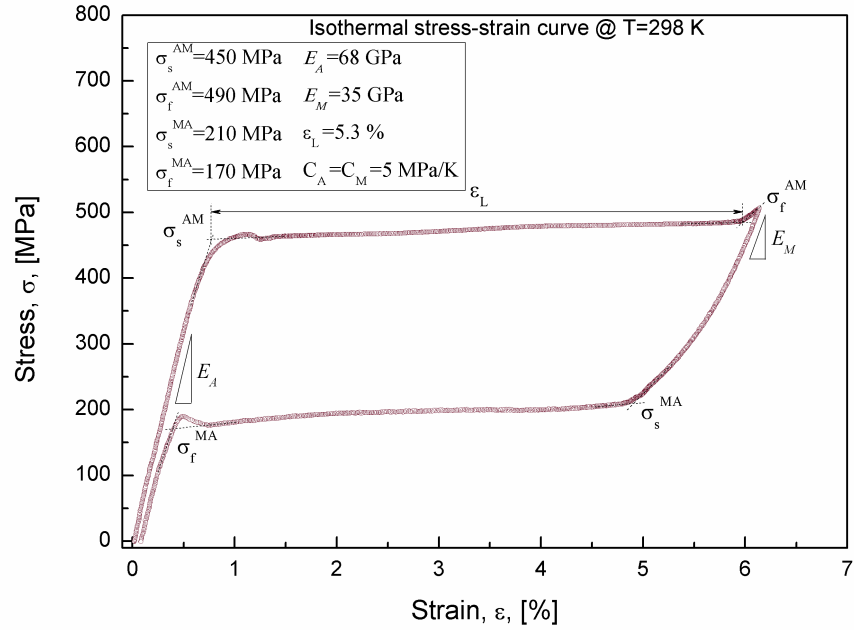


Figure 2.6: Thermo-mechanical properties of the *as received* material: a) isothermal ($T=298\text{K}$) stress strain curve.

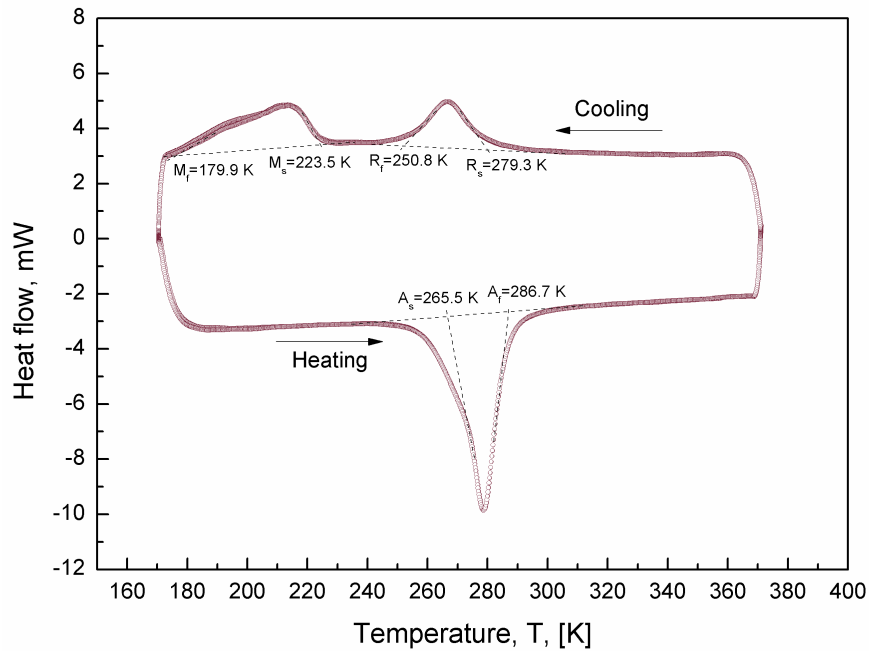


Figure 2.7: Thermo-mechanical properties of the *as received* material: Differential Scanning Calorimetry curve.

Fatigue test have been carried out, by using an universal servo-hydraulic testing machine (Instron 8500), within a climatic chamber (MTS 651) at an environmental temperature $T=298\text{ K}$. In addition, strain were measured by a resistance extensometer with a gauge length of 10 mm, and special care was adopted to avoid sliding during

fatigue tests.

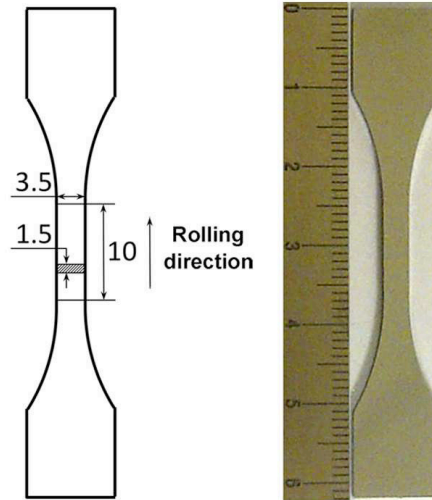


Figure 2.8: Dog-bone shaped specimen for fatigue tests.

Due to the cyclic creep-like behavior of NiTi alloys, which causes the accumulation of residual deformations in the first mechanical cycles ($\delta\epsilon_{resi}$), as illustrated in figure 2.9, fatigue tests have been carried out in two subsequent steps:

- 1) **Material stabilization:** fatigue cycles at fixed values of the maximum deformation (ϵ_{max}) and increasing values of the minimum one (ϵ_{min}), in such a way that the load is reversed, in the unloading path, when the stress is close to zero ($\sigma \approx 0$), in order to avoid compression stresses (see figure 2.9) [93]. This step is assumed to be completed after N_s cycles, when the material exhibits a stable stress-strain response, *i.e.* when the increment of residual strain in the previous 10 cycles is lower than the 0.5% of the maximum applied strain ($\sum_{i=N_s-10}^{N_s} \delta\epsilon_{Res i} < 0.5\epsilon_{max}$). As clearly illustrated in figure 2.9, the minimum deformation after N_s cycles corresponds to the stabilized residual deformation (ϵ_{res}), *i.e.* to the accumulation of residual deformation in the first N_s cycle ($\epsilon_{res} = \sum_{i=1}^{N_s} \delta\epsilon_{resi}$).
- 2) **Fatigue life estimation:** strain controlled fatigue cycles at a frequency of 0.5 Hz, with a strain range $\Delta\epsilon = 2\epsilon_a$, corresponding to the stabilized recovery deformation namely ϵ_{rec} , between a minimum strain $\epsilon_{min} = \epsilon_{res}$ and a maximum strain $\epsilon_{max} = \epsilon_{res} + \Delta\epsilon$ (see figure 2.9); complete rupture was

adopted as failure condition and the corresponding number of cycles N_f has been recorded.

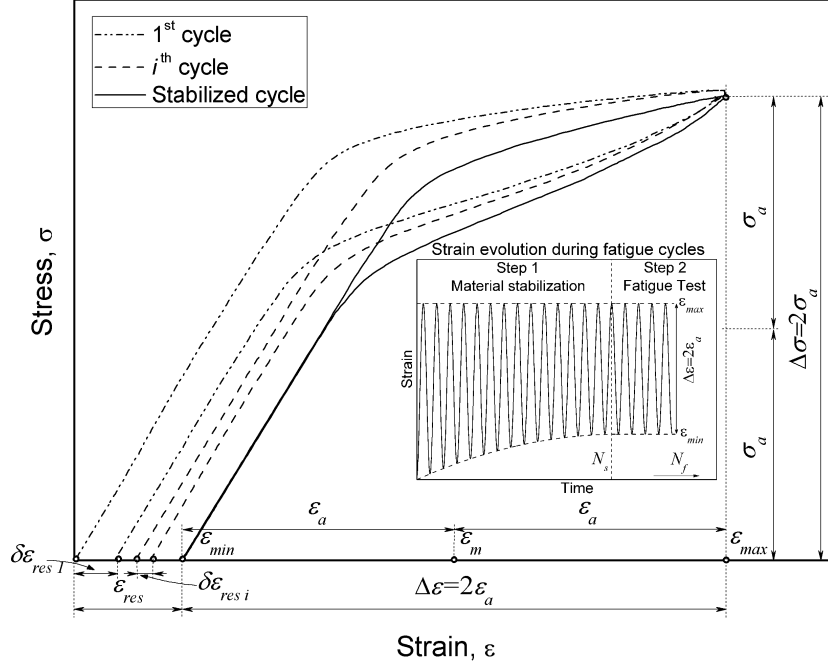


Figure 2.9: Schematic depiction of the evolution of the stress-strain hysteresis loop under cyclic loadings at fixed values of maximum strain.

It is worth noting that the evolution of cyclic response of the material during the first N_s cycles can be regarded as a transient phenomena and, consequently, material stabilization can be considered as a preliminary training process, *i.e.* it must be carried out in those applications where a stable mechanical and functional response is required. If the stabilization is considered as a material processing step in the subsequent fatigue cycles residual deformations can be neglected, then new effective values of the minimum and maximum deformations can be defined: $\epsilon'_{min} = \epsilon_{min} - \epsilon_{res}$ and $\epsilon'_{max} = \epsilon_{max} - \epsilon_{res}$. From this standpoint the fatigue experiments illustrated in this paper can be considered as repeated strain tests, *i.e.* with $\epsilon'_{min} = 0$, $\epsilon'_{max} = \Delta\epsilon$ and $R_\epsilon = \epsilon'_{min}/\epsilon'_{max} = 0$.

Several tests were carried out for different values of the maximum strain, ϵ_{max} , within the pseudoelastic regime of the alloy, *i.e.* in the range between 0.7% and 4.5% and at least two specimen for each testing conditions were analyzed.

2.3. Functional and Structural Fatigue

The modification of the hysteretic stress-strain response of the material obtained under repeated isothermal mechanical cycles involving stress induced transformations can be attributed to several microstructural mechanisms, such as the formation of stabilized martensite, detwinning, grain reorientation, slips deformations and the generation of lattice defects mainly in the form of dislocations. In particular, upon repeated loadings many preferentially oriented martensite variants reaches stress conditions that inhibit the possibility to recover their original configuration, and the dislocation density tends to increase, as a consequence of shear deformations at the martensite-austenite interfaces. These microstructural evolutions cause a gradual loss of functional properties, i.e. the capability to dissipate energy and to recover the applied deformation, with a consequent increase of residual strain and decrease of the hysteresis loop area, as schematically illustrated in figure 2.9. In this work the functional fatigue properties are deeply analyzed by identifying and tracking the evolution of several functional fatigue parameters, as schematically shown in figure 2.10:

- 1) recovered strain, ϵ_{rec} : pseudo-elastic recovery from mechanical unloading;
- 2) residual strain, ϵ_{res} , : unrecovered strain upon unloading;
- 3) recovered energy, E_{rec} : energy below the unloading branch of the hysteresis loop;
- 4) dissipated energy, E_{dis} : energy between loading and unloading paths of the hysteresis loop;
- 5) effective Young's modulus, E_{A} : slope of the first elastic response in the σ - ϵ diagram;
- 6) direct transformation stress, $\sigma_{\text{A-M}}^{\text{s}}$: intersection between elastic straight line and tangent to the stress plateau [58];

In addition, phase transition temperatures of the specimens, after fatigue tests, were investigated by DSC measurements.

Fatigue of Pseudoelastic NiTi within the Stress-Induced Transformation Regime

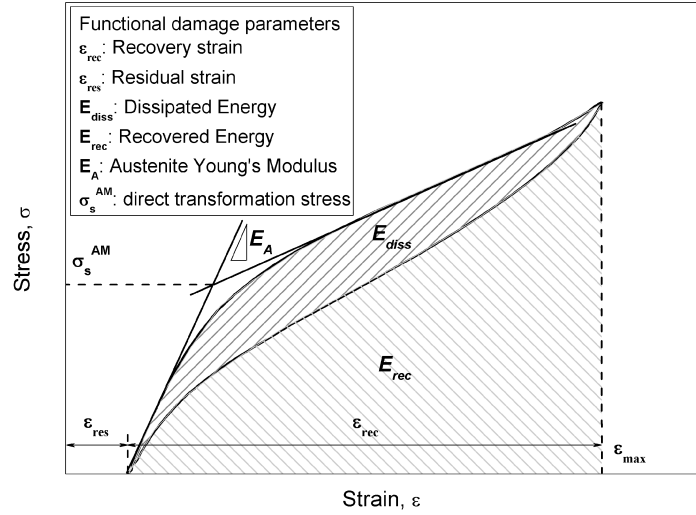


Figure 2.10: Schematic depiction of the functional damage parameters.

Table 2.1 illustrates the strain-life data obtained from fatigue tests which were carried out for several values of the applied maximum strain (ϵ_{max}) within the stress-strain transformation plateau, *i.e.* in the range 0.7-4.5%. In particular, the stabilized recovery and residual deformations (ϵ_{rec} and ϵ_{res}), together the numbers of cycles to material stabilization and failure (N_s and N_f), for each testing specimen are reported. As expected, the table illustrates that the number of cycles to failure increases with decreasing the applied maximum deformation, from about 300 cycles at $\epsilon_{max} = 4.5\%$ to about 14000 at $\epsilon_{max} = 0.7\%$. Furthermore, the number of cycles to material stabilization, which is close to 100, is mainly unaffected by the maximum applied strain and similar results have been obtained in previous researches [73-74] even in the case of single crystal alloys [85-86]. It is a unusual behavior if compared with common metals, where the stabilization of the stress-strain response of the material, due to repeated plastic deformations, is related to the cycles to failure and, consequently, to the strain amplitude [91]. However, it is worth noting that the key mechanisms for residual strain in SMAs can be attributed to several local contributes such as plastic deformation mechanisms, retained martensite and detwinning or reorientation of martensite variants. In any case these complex mechanisms are not studied in detail in this investigation, and the residual strain is treated as an overall parameter defining the irreversible effects of the SMA under cyclic loading conditions. In particular, the table shows that ϵ_{res} increases with increasing the applied maximum strain, ranging from about 0.01% at $\epsilon_{max} = 0.7\%$ to 1.3% at $\epsilon_{max} = 4.5\%$, and, consequently, the

Fatigue of Pseudoelastic NiTi within the Stress-Induced Transformation Regime

recovery strain, ϵ_{rec} , varies between 0.69% and 3.2% ($\epsilon_{rec} = \epsilon_{max} - \epsilon_{res}$). The recovered strain can be regarded as a functional fatigue parameter, as it describes the pseudoelastic recovery capability of the alloy under cyclic loading; therefore, the results presented in table 2.1 indicate that the material has a good functional fatigue response, especially for low values of the applied strain, as it exhibits negligible residual deformations.

Table 2.1: Data obtained from material stabilization and fatigue life steps.

Specimen number	Maximum strain ϵ_{max}	Residual strain ϵ_{res}	Recovery strain ϵ_{rec}	Cycles to stabilization N_s	Cycles to failure N_f
1	0.70%	0.01%	0.69%	100	13495
2	0.70%	0.01%	0.69%	100	10832
3	1.00%	0.02%	0.98%	100	3384
4	1.00%	0.02%	0.98%	100	4829
5	1.30%	0.05%	1.25%	100	2432
6	1.30%	0.02%	1.28%	100	1737
7	1.45%	0.11%	1.34%	100	1690
8	1.70%	0.19%	1.51%	100	1900
9	1.70%	0.19%	1.51%	100	1081
10	1.70%	0.08%	1.62%	100	1550
11	2.00%	0.20%	1.80%	100	784
12	2.00%	0.18%	1.82%	100	622
13	2.40%	0.29%	2.11%	100	510
14	2.40%	0.20%	2.20%	100	840
15	2.80%	0.20%	2.61%	100	943

Fatigue of Pseudoelastic NiTi within the Stress-Induced Transformation Regime

16	3.00%	0.58%	2.43%	100	560
17	3.00%	0.58%	2.42%	100	578
18	3.50%	0.82%	2.69%	100	610
19	3.50%	0.70%	2.80%	100	578
20	4.00%	0.95%	3.05%	100	690
21	4.50%	1.30%	3.20%	100	340

In the following subsections the results concerning the evolution of the aforementioned functional fatigue parameters are reported and discussed, while in Table 2.2 some summary data are illustrated. In particular, this table reports the values of the parameters after material stabilization (cycle N_s) together with the reference values at the first mechanical cycle (cycle #1). It is worth noting that no significant variation of the functional response has been observed among specimens subjected to the same testing conditions, and most of the results reported in the following represent average values of different specimens.

Table 2.2: Values of the functional fatigue parameters obtained from material stabilization.

Maximum strain ϵ_{max}	Residual strain, ϵ_{res} , [%]		Recovery strain, ϵ_{rec} , [%]		Dissipated Energy, E_{diss} , [MJ/m ³]		Recovery Energy, E_{rec} , [MJ/m ³]		Young's modulus, E , [GPa] (Cycle #1 $E_A=68$ GPa)	Transformation stress, σ_{ssAM} , [MPa] (Cycle #1 $\sigma_{ssAM}=450$ MPa)
	Cycle #1	Cycle N_s	Cycle #1	Cycle N_s	Cycle #1	Cycle N_s	Cycle #1	Cycle N_s		
0.70%	0.01	0.02	0.69	0.68	0.45	0.03	2.11	1.23	67.3	
1.00%	0.01	0.04	0.99	0.96	0.80	0.09	2.97	1.99	66.4	355
1.30%	0.01	0.06	1.29	1.24	1.15	0.23	3.87	2.65	65.0	342
1.45%	0.01	0.09	1.44	1.36	1.40	0.42	4.78	3.26	63.5	331
1.70%	0.02	0.14	1.68	1.56	1.72	0.60	5.23	3.84	62.2	322
2.00%	0.03	0.16	1.97	1.84	2.10	0.81	5.84	4.25	61.9	301
2.40%	0.06	0.29	2.33	2.11	2.66	1.02	7.40	5.32	60.7	285

Fatigue of Pseudoelastic NiTi within the Stress-Induced Transformation Regime

3.00%	0.07	0.59	2.92	2.41	3.29	1.21	8.50	5.59	58.1	250
3.50%	0.08	0.84	3.42	2.66	4.89	1.42	9.71	6.14	54.2	239
4.00%	0.16	0.95	3.83	3.05	5.87	1.81	10.82	6.88	49.4	227
4.50%	0.20	1.24	4.33	3.26	7.37	2.38	12.45	7.64	44.9	215

2.3.1 Recovered and Residual Strain

Recovery and residual strains, ϵ_{rec} and ϵ_{res} , are important functional fatigue parameters because they represent a quantitative measure of the cyclic evolution of the pseudoelastic properties of the alloy during loading history. Figure 2.11 reports the evolution of ϵ_{rec} (figure 2.11a) and ϵ_{res} (figure 2.11b) as a function of the number of mechanical cycles and for different values of the maximum strain, ϵ_{max} , in pseudoelastic regime of the alloy, i.e. in the range between 0.7 % and 4.5 %. As expected, a rapid increase of ϵ_{res} , with an associated decrease of ϵ_{rec} , occurs during the first few cycles, as a result of a great available amount of martensite to stabilize and the low dislocation density in the as is material. Nevertheless, the material reaches a pseudoelastic steady state condition with increasing the number of cycles. These phenomena are more evident for the higher values of applied deformation by which an higher evolution rate has been registered; on the contrary the number of cycles to stabilization N_s , which is always between 100 and 140, seems to be unaffected by the strain amplitude. Similar results have been obtained in previous researches [73, 82] even in the case of single crystal alloys [86]. It is a unusual behavior if compared with common metals, where the stabilization of the stress-strain response of the material, due to repeated plastic deformations, is related to the cycles to failure and, consequently, to the strain amplitude [64]. In addition, figure 2.11a and Table 2.2 also show that pseudoelastic strain recovery capabilities of the SMA are mainly preserved, with stabilized values of ϵ_{rec} ranging from 72% to 97% of ϵ_{max} , at $\epsilon_{max} = 4.5\%$ and 0.7% respectively.

Fatigue of Pseudoelastic NiTi within the Stress-Induced Transformation Regime

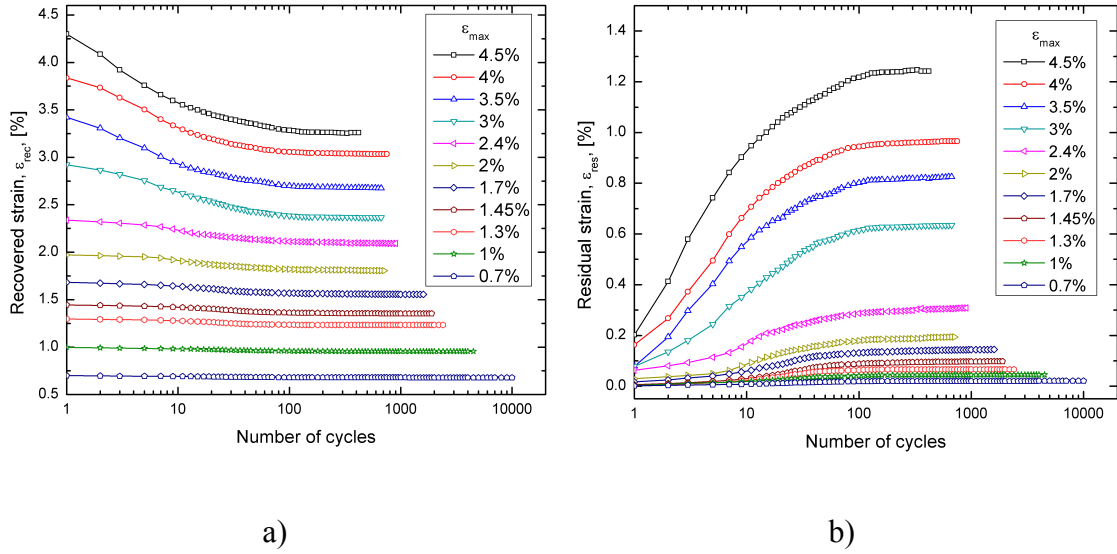


Figure 2.11: Evolution of recovery strain ϵ_{rec} (a) and of the residual strain ϵ_{res} (b) as a function of the number of mechanical cycles and for different values of the maximum applied strain ϵ_{max} .

Figure 2.12 reports the stabilized values of ϵ_{res} and ϵ_{rec} as a function of the maximum applied strain, ϵ_{max} , in a log-log diagram and a linear trend of both parameters is observed. In particular, ϵ_{res} ranges from about 0.01% at $\epsilon_{max} = 0.70\%$ to 1.30% at $\epsilon_{max} = 4.50\%$ and, as a consequence, ϵ_{rec} ranges from about 0.69% to about 3.20%. Complete data for the other values of maximum strain are reported in Table 2.2.

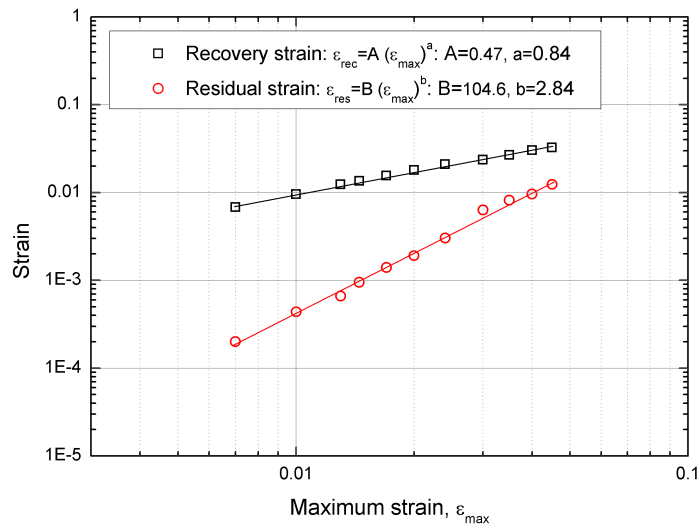


Figure 2.12: Stabilized values of the recovery and residual strains, strain ϵ_{rec} and ϵ_{res} , as a function of the maximum applied strain ϵ_{max} .

2.3.2 Recovered and Dissipated Energy

As described in the previous sections and schematically depicted in figure 2.10, repeated mechanical cycles cause a modification of the whole stress-strain hysteretic behavior of the alloy, i.e. they affect not only the pseudoelastic strain recovery capability but also the shape of the stress-strain hysteretic loop. As a consequence, a marked modification of the recovered and dissipated energy, E_{rec} and E_{diss} (see figure 2.13), has been observed and the knowledge of this trend is of major concern, especially when dealing with the design of energy absorber devices, such as seismic absorbers [91]. Figure 6 reports the evolution E_{rec} (figure 2.13.a) and E_{diss} (figure 2.13.b) as a function of the number of mechanical cycles and for different values of the maximum strain, ϵ_{max} .

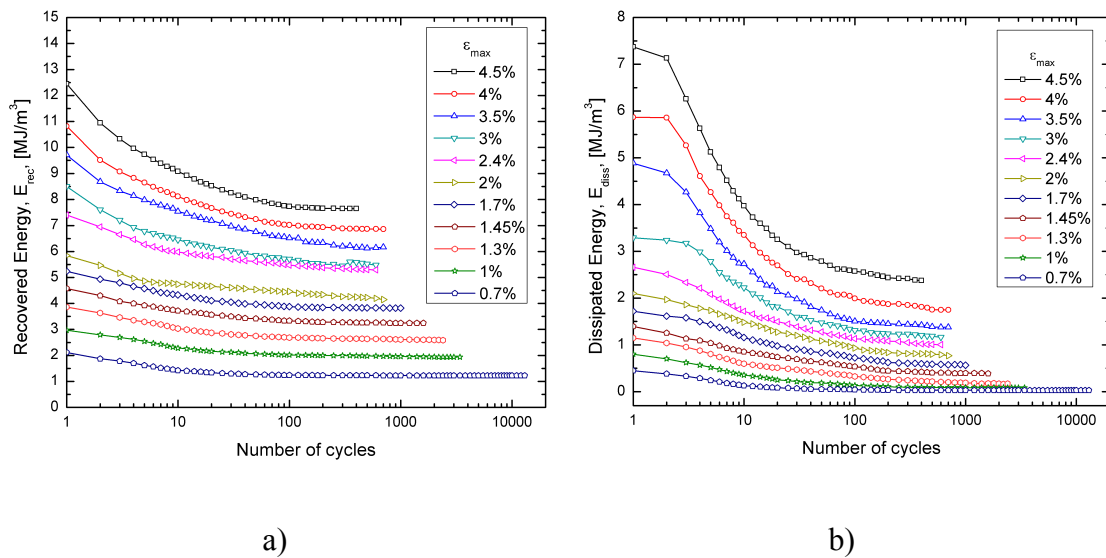


Figure 2.13: Evolution of recovery energy E_{rec} (a) and of the dissipated energy E_{diss} (b) as a function of the number of mechanical cycles and for different values of the maximum applied strain ϵ_{max} .

As expected, a rapid decrease of both parameters occurs during the first few cycles, as a direct consequence of the development of residual deformations (see figure 2.9), and this effect becomes more evident as ϵ_{max} increases. However, a higher reduction rate of the dissipated energy has been observed, which can be attributed to the increased fraction of stabilized material, i.e. the material which does not undergo reversible

phase transition mechanisms during mechanical cycling. In fact, E_{diss} is strictly related to the hysteresis in the stress-induced phase transition mechanisms. In particular, figure 2.13b and Table 2.2 show that stabilized values of E_{diss} are between 30% and 40% of the values of the first cycles for $\epsilon_{max} > 1.30\%$, while even more marked reductions are observed for the lower values of ϵ_{max} , because these latter are very close to the elastic limit of the material and, consequently, the hysteretic behavior tends to vanish. This trend should be accurately taken into account in the design of energy absorber and seismic devices operating under low cycle regime, as it implies a marked degradation of their functional response. Alternatively, proper training processes of the material should be carried out in order to obtain a stable functional response.

Figure 2.14 reports the stabilized values of E_{rec} and E_{diss} as a function of the maximum applied strain, ϵ_{max} , in a semi-log diagram. The figure show that E_{rec} ranges from about 1.22 MJ/m^3 at $\epsilon_{max} = 0.70\%$ to 7.64 MJ/m^3 at $\epsilon_{max} = 4.50\%$, while E_{diss} ranges from about 0.03 MJ/m^3 to about 2.38 MJ/m^3 . Complete data for the other values of maximum strain are reported in Table 2.2.

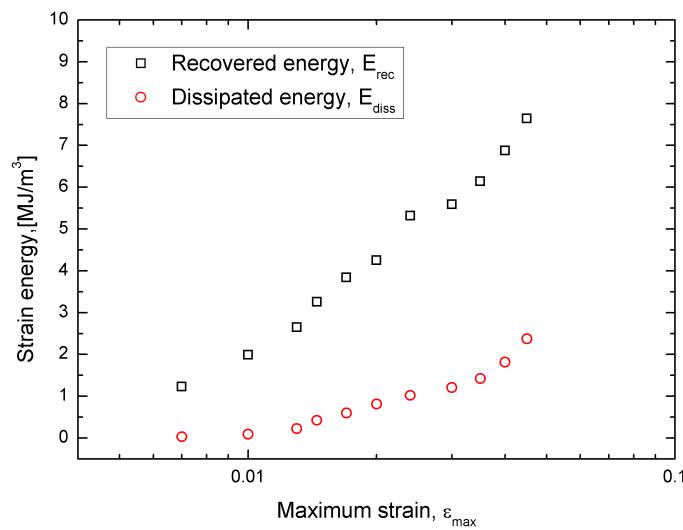


Figure 2.14: Stabilized values of the recovery and dissipated energies, E_{rec} and E_{diss} , as a function of the maximum applied strain ϵ_{max} .

2.3.3 Transformation Stress and Young's Modulus

Figure 2.15a illustrates the evolution of the effective Young's modulus, E , as a function of the number of mechanical cycles during material stabilization (cycle # $<Ns$), while Fig. 2.15b shows the evolution of the direct transformation stress. Both parameters exhibit a marked decrease in the first few cycles, and these effects become more evident when increasing the maximum strain ϵ_{max} . This result can be attributed to the formation of a heterogeneous microstructure, i.e. to several microstructural mechanisms occurring during stabilization process, such as the formation of stabilized martensite, detwinning, grain reorientation and slips deformations. This heterogeneous microstructure is characterized by an effective Young's modulus which is between those of austenite (E_A) and martensite (E_M), as illustrated in Fig. 2.15a. In particular, a marked reduction, down to 45 GPa, has been recorded for $\epsilon_{max} = 4.5\%$.

Similar considerations apply to the direct transformation stress, where the formation and accumulation of stabilized martensite, as well as the presence of a heterogeneous structure, cause a decrease of the critical stress to transform austenite to martensite together with a larger range of stress transformation and an increase of the slopes of the stress-strain plateau. In fact, dislocations could play a similar role to strain hardening in plasticity and the increased dislocation density causes the formation of internal stresses that could assist the formation of stress induced martensite. In particular, a marked reduction of σ_{AM}^s , from 450 MPa to 215 MPa, has been observed for $\epsilon_{max} = 4.5\%$, while a decrease from 450 MPa to 355 was recorded for $\epsilon_{max} = 1.0\%$. No value is reported for the lowest applied strain, $\epsilon_{max} = 0.7\%$, because it is very close to the elastic response of the material and the onset of stress-induced phase transformation mechanisms cannot clearly identified. Complete data for the other values of maximum strain are reported in Table 2.2.

Fatigue of Pseudoelastic NiTi within the Stress-Induced Transformation Regime

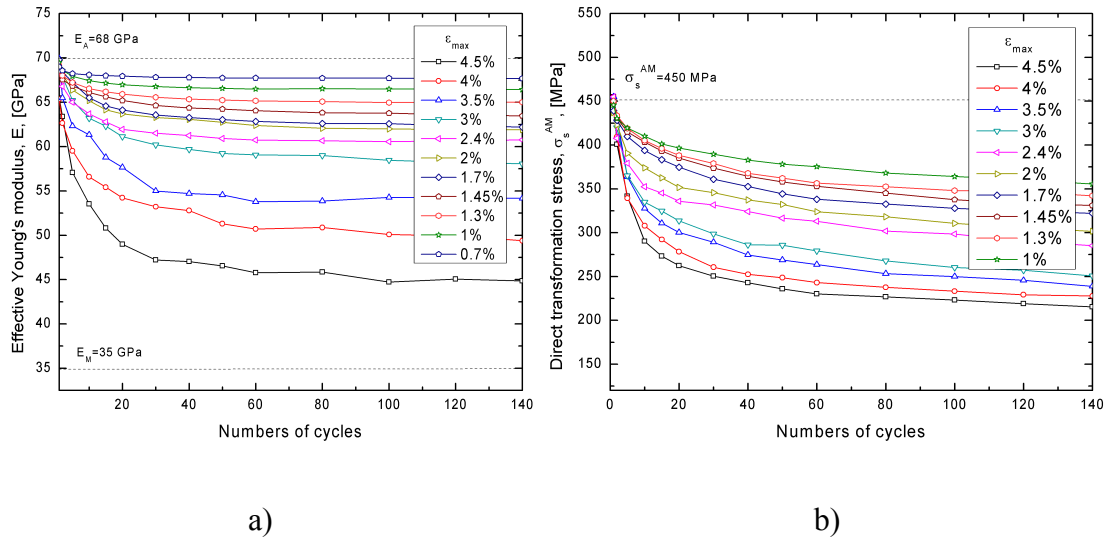


Figure 2.15: Evolution of Young's modulus, E , (a) and of the direct transformation stress, (b) as a function of the number of mechanical cycles and for different values of the maximum applied strain ϵ_{max} .

2.3.4 Transformation Temperatures

Differential scanning calorimetry tests were carried out on fatigue samples. Their DSC thermograms revealed to be similar to that of as received material (see Fig. 2.7). In particular, a two-stage transformation is observed during cooling (B2-R-B19'), while a one-stage transformation (B19'-B2) characterizes the heating branch of the curve. The results, in terms of peak temperatures, are summarized in figure 2.16. Increasing the maximum strain (ϵ_{max}), the R-B19' peak shifts toward lower temperature (from -67°C to -60°C), while the effect of ϵ_{max} on the other two peak temperatures is less pronounced. The irreversible plastic strain induced on the specimens by deformation and by transformation cycling promotes the stabilization of the R-martensite. Indeed, likewise Ti3Ni4 precipitates, higher density of dislocations acts as a resistance to lattice distortion due to the transformation from austenite to martensite, and the resistance is much more significant for transformation involving large lattice distortion like B19' transformation, while the effect becomes less considerable for transformation involving small lattice distortion like R-transformation [54]. Therefore, the introduction of dislocations by fatigue cycles leads to a decrease of the R-B19' characteristic temperatures. It is worth to note that mechanical cycling and formation

of lattice defects are also likely responsible for the stabilization of martensite regions. Deeper structural investigations are needed for an utter understanding of the microstructural alterations owing to mechanical cycling which lead to a resulting modification of the functional and mechanical properties characteristic of the material.

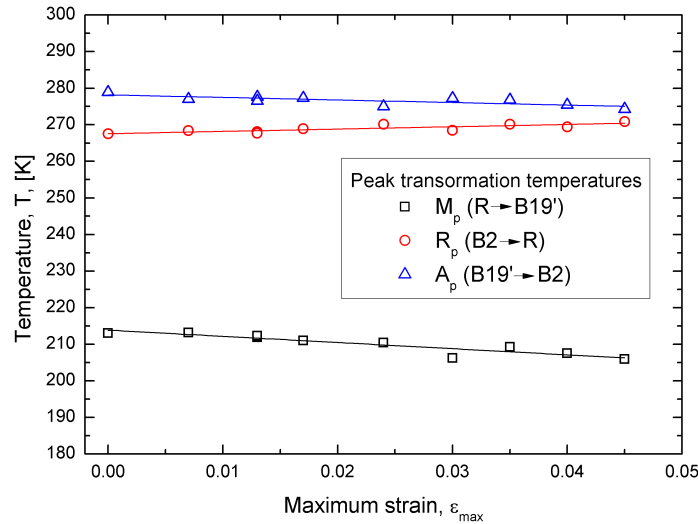


Figure 2.16: Evolution of the peak transformation temperatures (R_p , M_p and A_p) versus the maximum applied strain ϵ_{max} .

2.4 Strain-life Fatigue Model

A novel empirical approach is described in this section by using modified theories on low cycle fatigue of common engineering metals, *i.e.* on the basic assumptions of the Coffin-Manson approach [91]; in particular, as well known, this approach defines a relation between the strain range and the cycles to failure, $\Delta\epsilon = f(N_f)$, based on the calculation of elastic and plastic deformations during cyclic loadings. Unfortunately, classical assumptions cannot be directly applied to pseudoelastic NiTi alloys since the formation of stress induced martensite (SIM), during mechanical loading, leads to a peculiar behavior of the material and unconventional complex mechanisms of deformation occur [54].

However, if considering the stable hysteretic response of the SMA the total strain range during mechanical cycling, $\Delta\epsilon$, can be regarded as the sum of elastic strain range, $\Delta\epsilon_e$, and inelastic strain range, $\Delta\epsilon_i$, as schematically illustrated in figure 2.17:

$$\Delta\varepsilon = \Delta\varepsilon_e + \Delta\varepsilon_i \quad (2.1)$$

In particular, the elastic strain range amplitude, $\Delta\varepsilon_e$, can be directly obtained from the stress range, $\Delta\sigma$, *i.e.* the stress corresponding to the turning point of the stabilized stress-strain hysteresis loop, by the Hooke's law:

$$\Delta\varepsilon_e = \frac{\Delta\sigma}{E(\xi_M)} \quad (2.2)$$

where $E(\xi_M)$ represents the effective Young's modulus of the SMA as a function of the volume fraction of the martensite ξ_M (see figure 2.17). In particular, the Young's modulus $E(\xi_M)$ is assumed to be dependent on the volume fraction of martensite according to the so-called Reuss formula [92]:

$$E(\xi_M) = \left(\frac{\xi_M}{E_M} + \frac{1-\xi_M}{E_A} \right)^{-1} \quad (2.3)$$

where E_A and E_M are the effective Young's moduli of austenite and martensite (see Figure 2.17) and they are obtained from the slope of the stress-strain curve in the elastic untransformed austenitic region (E_A) and in the fully transformed region (E_M).

The evolution of the volume fraction of martensite in the loading stage of the stress-strain curve is assumed to be a linear function of the strain in the stress-strain curves and can be expressed as a function of the total strain range as follows:

$$\xi_M = \begin{cases} 0 & \Delta\varepsilon < \varepsilon_{AM}^s \\ (\Delta\varepsilon - \varepsilon_s^{AM})/\varepsilon_L & \varepsilon_{AM}^s \leq \Delta\varepsilon \leq \varepsilon_{AM}^s + \varepsilon_L \\ 1 & \Delta\varepsilon < \varepsilon_{AM}^s + \varepsilon_L \end{cases} \quad (2.4)$$

where ε_L is the transformation strain, *i.e.* the strain corresponding to the complete stress-induced phase transformation, and ε_{AM}^s represents the elastic strain corresponding to the start transformation stress:

$$\varepsilon_{AM}^s = \frac{\sigma_{AM}^s}{E_A} \quad (2.5)$$

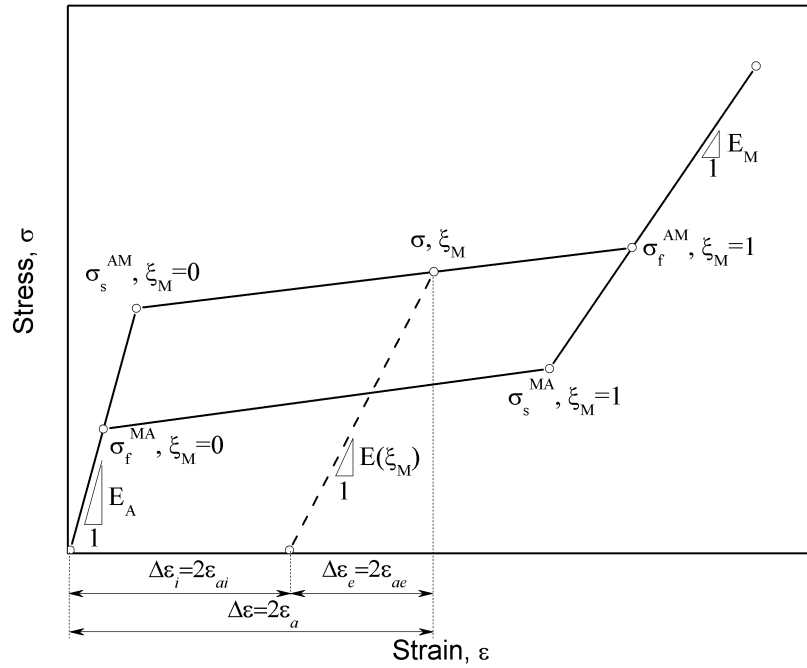


Figure 2.17: schematic depiction of the of the stress-strain curve of the alloy together with the main mechanical parameters.

The inelastic strain range, $\Delta\epsilon_i$, can be regarded as the pseudoelastic strain, i.e. it can be attributed to the reversible stress induced phase transformation, and can be obtained from equations (2.1) by using the experimentally measured total strain range, $\Delta\epsilon$, and the elastic strain range, $\Delta\epsilon_e$, calculated from equations 2.1-2.5.

In addition, fatigue data are normally reported as a function of the strain amplitudes ($\epsilon_a = \Delta\epsilon/2$) then equation (2.1) can be rewritten as follows:

$$\epsilon_a = \epsilon_{ae} + \epsilon_{ai} \tag{2.6}$$

Figure 2.18 illustrates the elastic, inelastic and total strain amplitude (ϵ_{ae} , ϵ_{ai} and ϵ_a) as a function of the number of cycle reversals to failure ($2N_f$) in a log-log diagram. Furthermore, as previously mentioned the experiments were carried out within the stress-induced transformation regime and, consequently, the fatigue response of the material in the full austenitic and martensitic regions has not been investigated. This condition is schematically depicted by two bounds in figure 2.18, one in the low-cycle region, corresponding to strain values beyond the limit of the transformation plateau ($2\epsilon_a < \epsilon_{AM}^s + \epsilon_L$), i.e. in the fully martensitic region ($\xi_M = 1$), and the other one in the

Fatigue of Pseudoelastic NiTi within the Stress-Induced Transformation Regime

high-cycle region ($2\varepsilon_a < \varepsilon_{AM}^S$), which corresponds to maximum strain within the elastic deformation of austenite ($\xi_M = 0$). These two bounds can be also regarded as the application limits of the proposed approach as different fatigue behavior are expected in the fully martensitic and austenitic regions due to different strain mechanisms, as well as to an intrinsic different fatigue properties of the two phases. This result has been demonstrated in previous studies, where the properties of the two phases have been directly and/or indirectly compared [65, 67, 70, 77, 79-80, 89-90], by analyzing the effects of the mean strain and of the testing temperature.

Finally, Figure 2.18 shows that both elastic and inelastic strain amplitude (ε_{ae} and ε_{ai}) are well approximated by straight lines in the log-log diagram and, consequently, the two strain components can be expressed by a power law relations in the $\varepsilon_a - 2N_f$ diagram, likewise to Coffin-Manson approach in common engineering metals.

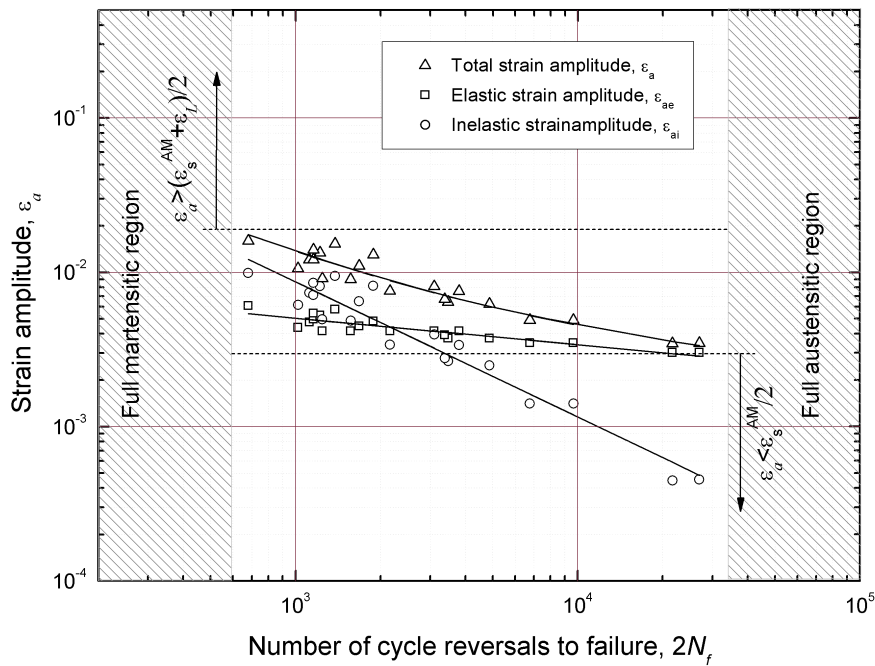


Figure 2.18: Modified Coffin-Manson approach.

In particular, the two strain components can be expressed as:

$$\varepsilon_{ae} = C (2N_f)^c \quad (2.7)$$

$$\varepsilon_{ai} = D (2N_f)^d \quad (2.8)$$

As a consequence, the total strain amplitude, ε_a , can be related to the cycle reversals to failure, $2N_f$, based on a modified Coffin-Manson approach:

$$\varepsilon_a = \varepsilon_{ae} + \varepsilon_{ei} = C (2N_f)^c + D (2N_f)^d \quad (2.9)$$

where the coefficients C and D and the exponents c and d obtained from the experiments are reported in Table 2.3. It is worth noting that these values have been obtained from a fitting of the experimental data reported in this investigation, *i.e.* they are related to specific specimen geometry and loading conditions and, consequently, they should be considered as testing parameters. However, the transferability of the proposed model to the engineering community, *i.e.* to predict fatigue life under generic loading conditions, requires further experimental results and the authors undertaken targeted works for verifying this modified Coffin-Manson approach.

Table 2.3: Parameters of the modified Coffin-Manson approach

Parameter	Value
<i>C</i>	0.016
<i>c</i>	-0.171
<i>D</i>	3.679
<i>d</i>	-0.876

2.5 SEM Analyses Of The Fracture Surfaces

In figures 2.19, SEM micrographs of the fracture surfaces obtained by testing the samples at different values of maximum deformation (a. 0.7%, b. 1.3%, c. 1.45%, d. 1.7%) are reported.

Fatigue of Pseudoelastic NiTi within the Stress-Induced Transformation Regime

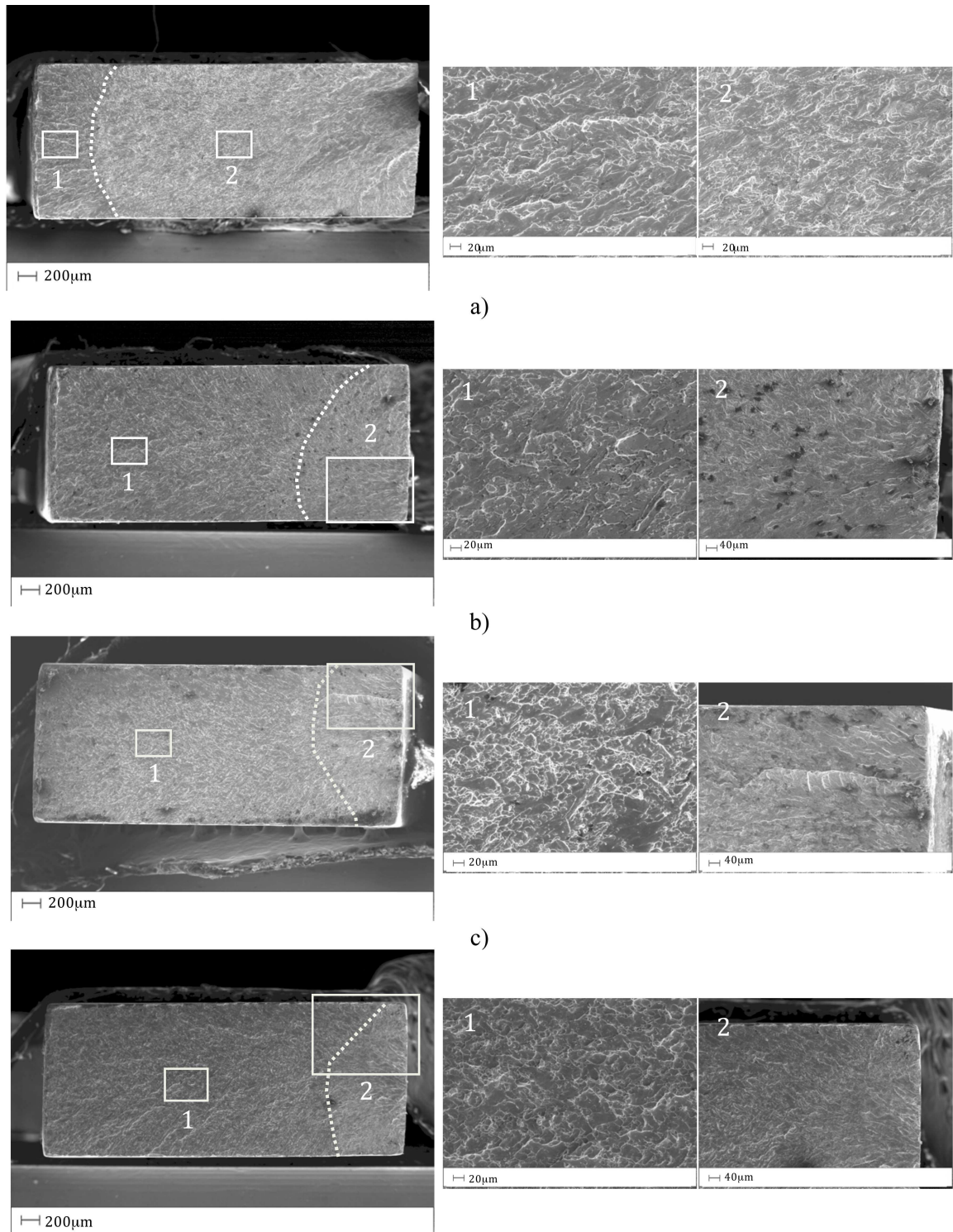


Figure 2.19: SEM micrographs of the fracture surfaces with highlight of the stable (right) and unstable (left) crack growth path obtained from specimens tested at different values of maximum deformation: a) 0.7%, b) 1.3%, c) 1.45% and d) 1.7%.

The analysis revealed that crack initiation occurs at the lateral surface of the specimens, as a consequence of the surface defects produced by the cutting process. In

fact, these irregularities lead to local stress concentrations and act as preferable nucleation sites. Furthermore, fracture surfaces show two distinct regions characterized by different morphologies. In particular, the right part of the surfaces in the SEM micrographs of figures 2.19 are characterized by fatigue striations, which are attributed to the stable crack growth resulting from fatigue loads, while the left sides show dimples structures typical of ductile overload fractures. In addition, as expected, the stable crack penetration area decreases with increasing of the maximum applied deformation, ranging from about 2.8 mm at $\epsilon_{\max} = 0.7\%$ to 0.8 mm at $\epsilon_{\max} = 1.7\%$.

2.6 Summary

Strain controlled fatigue tests of flat dog-bone shaped specimens, obtained from a commercial pseudoelastic NiTi sheet, have been carried out within the stress-induced transformation regime. Both functional and structural fatigue have been analyzed as a function of the strain amplitude, i.e. the evolution of the pseudoelastic capability and the cycles to failure. The results revealed a degradation of the pseudoelastic recovery, during the first mechanical cycles, and this effect becomes more evident when increasing the applied strain amplitude. However, a stable functional response is always observed after the first N_S cycles, namely the cycles to stabilization, which is almost unaffected by the strain amplitude and it is close to 100 cycles. Furthermore, structural fatigue data have been analyzed by a novel strain-life model, based on a modified Coffin-Manson approach, which takes into account the unusual strain mechanisms in SMAs. Finally, fracture surfaces have been analyzed by SEM observation in order to study the stable and unstable crack growth mechanisms.

CHAPTER 3

DIGITAL IMAGE CORRELATION TECHNIQUE: OVERVIEW

3.1 Introduction

Optical measurements of macroscopic parameters, such as strain and displacement, have evolved into an accepted branch of experimental stress analysis. Topics such as holography, speckle interferometry, speckle photography, speckle-shearing interferometry, white-light speckles and moiré have advanced from the basic research stage into mature methods employed to analyze a variety of engineering problems.

However, all of these techniques suffer from two major limitations. First, they have varying stability requirements. All interferometric methods have stringent stability requirements which limit their applicability to research environments for most cases. Speckle photography, moiré and white-light speckle have less stringent requirements than those for interferometric techniques, and are more adaptable to industrial applications. Secondly, the data processing required to reduce the fringe patterns and thereby obtain the desired data is laborious and time consuming for each method noted above. However, many researchers have recognized this difficulty and have developed computerized procedures to simplify the data reduction process.

The DIC method is a non-interferometric optical technique and has been widely accepted and commonly used as a powerful and flexible tool for the surface deformation measurement in the field of experimental solid mechanics. It directly provides full-field displacements and strains by comparing the digital images of the specimen surface in the un-deformed (or reference) and deformed states respectively. In principle, DIC is an optical metrology based on digital image processing and numerical computing. It was first developed by a group of researchers at the University of South Carolina in the 1980s [94–99] when digital image processing and numerical computing were still in their infancy [99].

During the past few years, the DIC method has been extensively investigated and significantly improved to reduce computation complexity, achieving high accuracy deformation measurement and expanding application range. For example, the two-

dimensional (2D) DIC method using a single fixed camera is limited to in-plane deformation measurement of the planar object surface. If the test object is of a curved surface, or three-dimensional (3D) deformation occurs after loading, the 2D DIC method is no longer applicable. To overcome this disadvantage of 2D DIC, 3D DIC based on the principle of binocular stereovision [100–103] was developed.

Compared with the interferometric optical techniques used for in-plane deformation measurement, the 2D DIC method has both advantages and disadvantages. For instance, it offers the following special and attractive advantages.

- (1) Simple experimental setup and specimen preparation: only one fixed CCD camera is needed to record the digital images of the test specimen surface before and after deformation. Specimen preparation is unnecessary (if the natural texture of a specimen surface has a random gray intensity distribution) or can simply be made by spraying paints onto the specimen surface.
- (2) Low requirements in measurement environment: 2D DIC does not require a laser source. A white light source or natural light can be used for illumination during loading. Thus, it is suitable for both laboratory and field applications.
- (3) Specimen size is not an issue as the method can be applied to both large and small specimens. Specimen size is accommodated by changing the magnification used in recording the image.
- (4) The method is not overly sensitive to vibration and a vibration isolation table is not necessary. However, it is essential that both the specimen and the camera be stable during the time required to record the image.
- (5) Large strains or significant rigid body movement does not cause difficulties if the specimen does not move out of the field of view of the camera.
- (6) It is a non-contact technique.
- (7) It can provide full field results, figure 3.1.

Nevertheless, the 2D DIC method also suffers some disadvantages: (1) the test planar object surface must have a random gray intensity distribution; (2) there is high sensitivity to fluctuation and the light intensity should be very uniform; (3) the calibration process is pretty tedious; (4) the measurements depend heavily on the quality of the imaging system; (5) at present, the strain measurement accuracy of the 2D DIC method is lower than that of interferometric techniques, and is not recommended as an effective tool for non-homogeneous small deformation measurement.

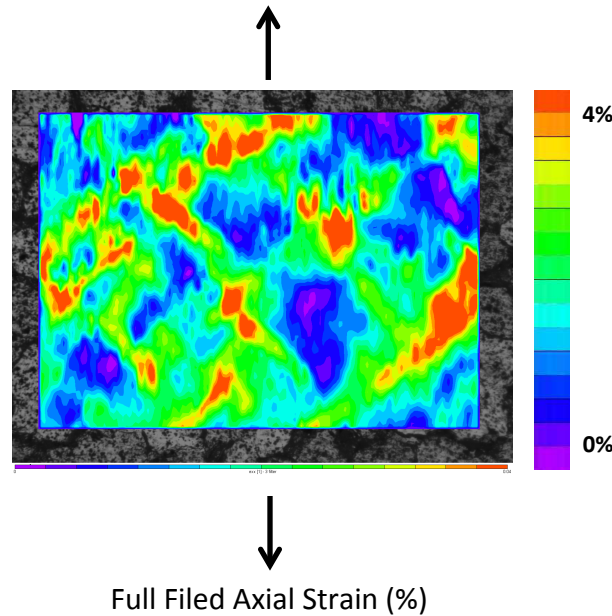


Figure 3.1: Full field axial strain obtained by using DIC technique.

In this chapter will be introduced the basic theory of digital correlation, as well as how it is used to determine displacement fields, the interpolation methods employed to extend the range of the measurements and, in the next chapter, the experiment performed with this technique.

3.2 2Dimensional DIC

In general, the implementation of the 2D DIC method comprises the following three consecutive steps, namely (1) specimen and experimental preparations; (2) recording images of the planar specimen surface before and after loading; (3) processing the acquired images using a computer program to obtain the desired displacement and strain information. In this section, issues on specimen preparation and image capture are introduced first. Then, the basic principles and concepts of 2D DIC are described.

3.3 Specimen Preparation and Image Capture

Figure 3.2 shows the schematic illustration of a typical experimental setup using an optical imaging device for the 2D DIC method. The specimen surface must have a

random gray intensity distribution (i.e. the random speckle pattern), which deforms together with the specimen surface as a carrier of deformation information. The speckle pattern can be the natural texture of the specimen surface or artificially made by spraying black and/or white paints, figure 3.3, or other techniques. The camera is placed with its optical axis normal to the specimen surface, imaging the planar specimen surface in different loading states onto its sensor plane.

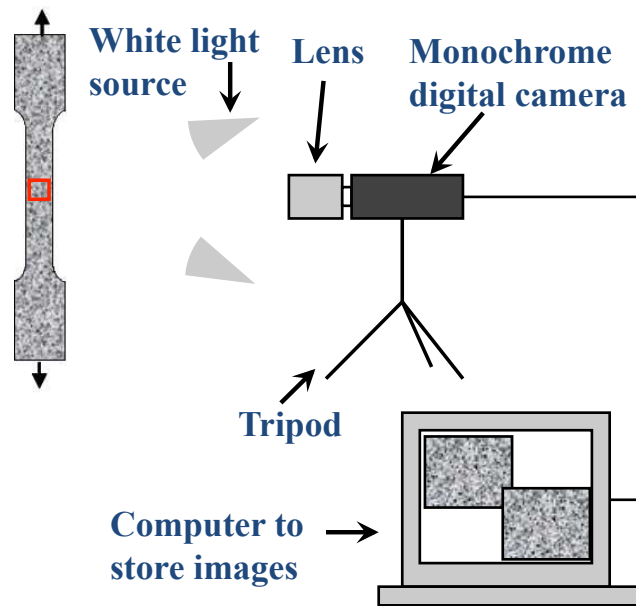


Figure 3.2: Typical optical image acquisition system for the 2D DIC technique.

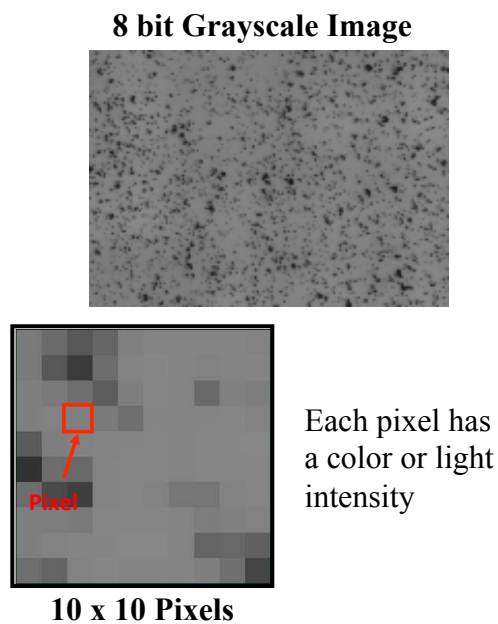


Figure 3.3: Example of the superficial pattern of a specimen.

3.4 Basic Principles and Concepts

After recording the digital images of the specimen surface before and after deformation, the DIC computes the motion of each image point by comparing the digital images of the test object surface in different states. In the following, the basic principles and concepts involved in 2D DIC are introduced.

3.4.1. Basic Principles.

In routine implementation of the 2D DIC method, the calculation area (i.e. region of interest, ROI) in the reference image should be specified or defined at first, which is further divided into evenly spaced virtual grids as shown in figure 3.4.

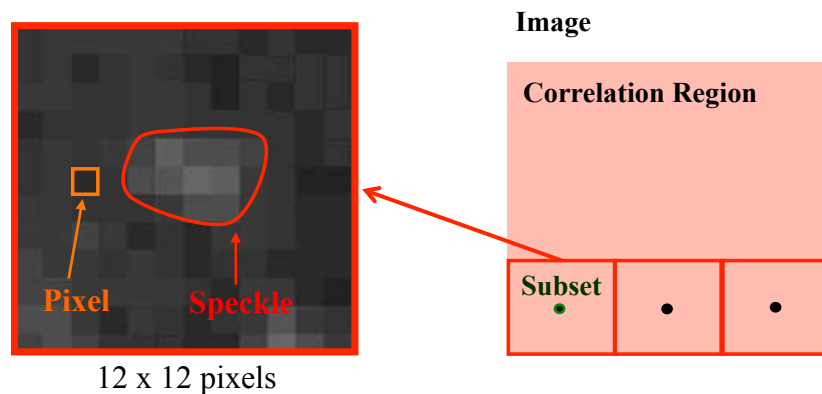


Figure 3.4: Reference image with a selected region of interest and subsequent division in subsets.

Each subset is characterized by a grey scale distribution denoted by a matrix of number, where each number represents a different grey scale, figure 3.5.

The basic principle of 2D DIC is the tracking (or matching) of the same points (or pixels) between the two images recorded before and after deformation as schematically illustrated in figure 3.6. In order to compute the displacements of point P , a square reference subset of $(2M + 1) \times (2M + 1)$ centered at point $P(x_0, y_0)$ from the reference image is chosen and used to track its corresponding location in the deformed image.

The reason why a square subset, rather than an individual pixel, is selected for matching is that the subset comprising a wider variation in gray levels will distinguish itself from other subsets, and can therefore be more uniquely identified in the deformed image.

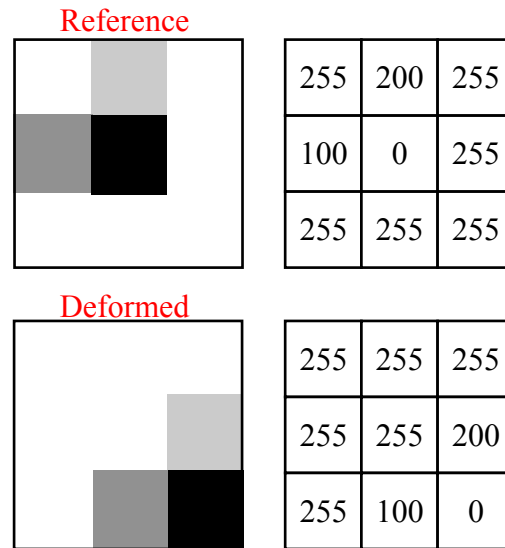


Figure 3.5: Example of grey scale distribution.

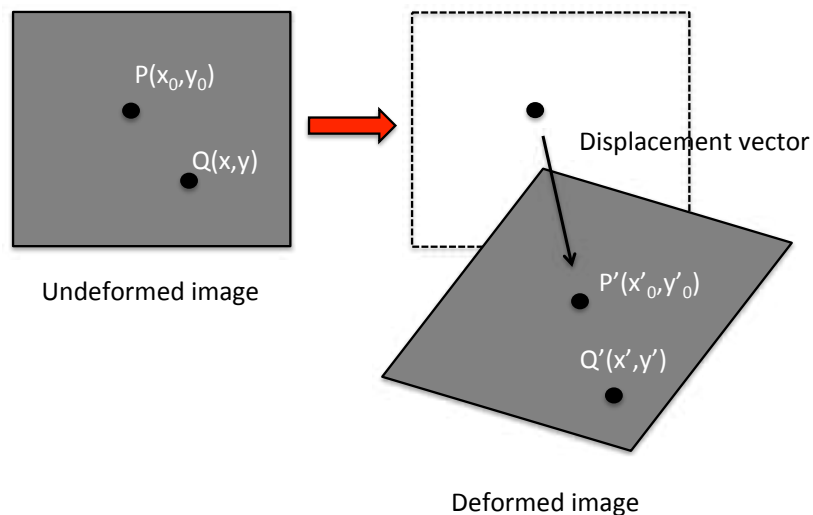


Figure 3.6: Correlation scheme between the undeformed (reference) and deformed image.

To evaluate the similarity degree between the reference subset and the deformed subset, a cross-correlation (CC) criterion or sum-squared difference (SSD) correlation criterion must be predefined. The matching procedure is completed through searching the peak position of the distribution of a correlation coefficient. Once the correlation

coefficient extremum is detected, the position of the deformed subset is determined. The differences in the positions of the reference subset center and the target subset center yield the in-plane displacement vector at point P , as illustrated in figure 3.6.

3.4.2 Shape Function/Displacement Mapping Function.

The idea of the Digital Image Correlation technique is to try to approximate a 2D function that maps points from the reference to the deformed image.

It is reasonable to assume that the shape of the reference square subset is changed in the deformed image. However, based on the assumption of deformation continuity of a deformed solid object, a set of neighboring points in a reference subset remains as neighboring points in the target subset. Thus, as schematically shown in figure 3.6, the coordinates of point $Q(x, y)$ around the subset center $P(x_0, y_0)$ in the reference subset can be mapped to point $Q'(x', y')$ in the target subset according to the so-called shape function [104] or displacement mapping function [105]:

The most simple way to define this function is shown in figure 3.7 and described by the following equation, where the correlation function of a single point is described.

$$x' = x + u \tag{3.1a}$$

$$y' = y + v \tag{3.1b}$$

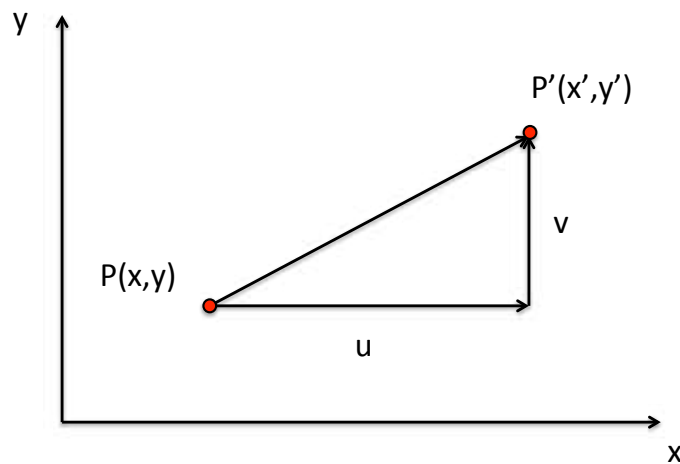


Figure 3.7: Correlation function of a single point.

If all the points of a subset have to be mapped the correlation function is described as below.

$$x' = x + u(x, y) \tag{3.2a}$$

$$y' = y + v(x, y) \tag{3.2b}$$

In order to get $u(x,y)$ and $v(x,y)$, a Taylor expansion, about the center point of the subset, has to be done. In function of the displacement and strain associated to the subset, different order of the expansion can be selected. If only a rigid translation, with no strain or rotation, is allowed, the subset remains square, figure 3.8, therefore a zero order Taylor expansion can be used, where the displacement field is described as a constant value, with no dependency from the coordinates, and each point in the subset will be characterized by the same displacement vector.

$$u(x, y) = u_0 \tag{3.3a}$$

$$v(x, y) = v_0 \tag{3.3b}$$

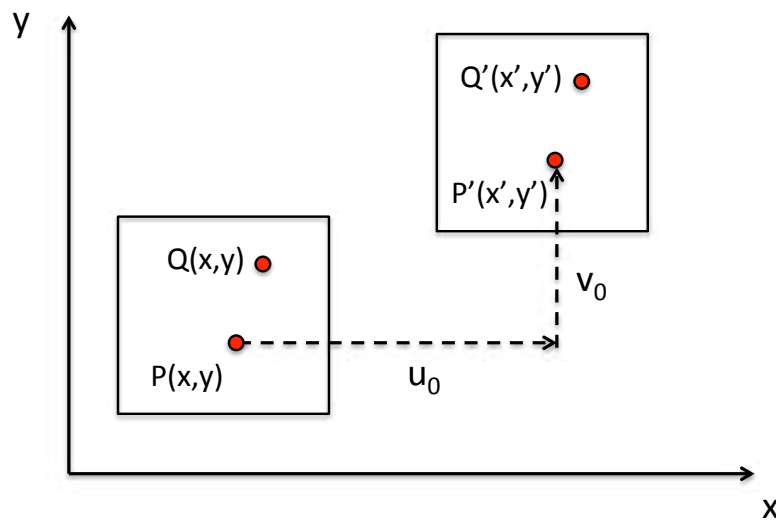


Figure 3.7: Correlation function of the points inside a subset with the displacement field described with a zero order Taylor expansion. The subset keeps its shape with no rotations or deformations.

Obviously, the zero-order shape function is not sufficient to depict the shape change of the deformed subset. Thus, the first-order shape function that allows translation,

rotation, shear, normal strains and their combinations of the subset is most commonly used:

$$u(x, y) = u_0 + \frac{du}{dx} \Delta x + \frac{du}{dy} \Delta y \quad (3.4a)$$

$$v(x, y) = v_0 + \frac{dv}{dx} \Delta x + \frac{dv}{dy} \Delta y \quad (3.4b)$$

It is important to underline that constant strain (and/or rotation) are assumed in this case and the subset remains parallelogram, figure 3.8.

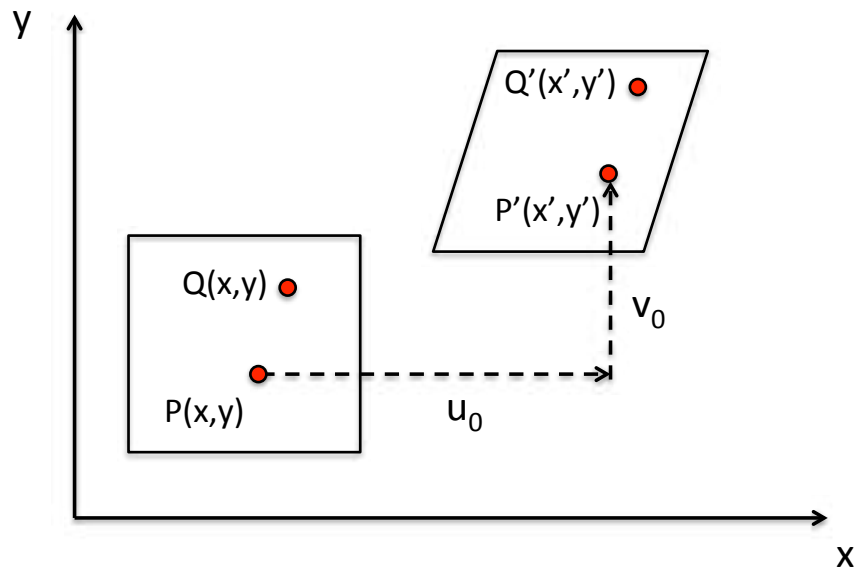


Figure 3.8: Correlation function of the points inside a subset with the displacement field described with a first order Taylor expansion. The subset gets a parallelogram shape.

Besides, the second-order shape functions proposed by Lu *et al* [105] can be used to depict more complicated deformation states of the deformed subset:

$$u(x, y) = u_0 + \frac{\partial u}{\partial x} \Delta x + \frac{\partial u}{\partial y} \Delta y + \frac{1}{2} \frac{\partial^2 u}{\partial x^2} \Delta x^2 + \frac{1}{2} \frac{\partial^2 u}{\partial y^2} \Delta y^2 + \frac{\partial^2 u}{\partial x \partial y} \Delta x \Delta y \quad (3.5a)$$

$$v(x, y) = v_0 + \frac{\partial v}{\partial x} \Delta x + \frac{\partial v}{\partial y} \Delta y + \frac{1}{2} \frac{\partial^2 v}{\partial x^2} \Delta x^2 + \frac{1}{2} \frac{\partial^2 v}{\partial y^2} \Delta y^2 + \frac{\partial^2 v}{\partial x \partial y} \Delta x \Delta y \quad (3.5b)$$

The latter form is the most common used, the strains vary throughout the subset that can become general quadrilaterals or have curved edges, figure 3.9.

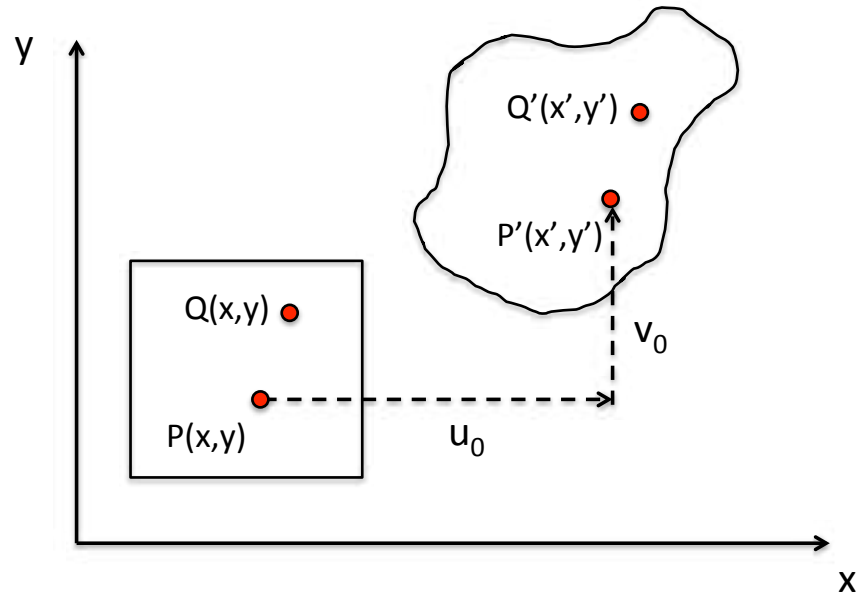


Figure 3.9: Correlation function of the points inside a subset with the displacement field described with a second order Taylor expansion. The subset change its shape as a consequence of the deformations and rotations

3.5 Correlation Criterion.

As already mentioned, to evaluate the similarity degree between the reference and deformed subsets, a correlation criterion should be defined in advance before correlation analysis. Although different definitions of correlation criteria can be found in the literature, these correlation criteria can be categorized into two groups, namely Cross-Correlation (CC) criteria and Sum of Square Difference (SSD) correlation criteria [106, 107]. It is worth noting that the CC criteria are actually related to the SSD criteria.

3.6 Interpolation Scheme.

As can be seen from equation (1), the coordinates of point (x', y') in the deformed subset may locate between pixels (i.e. sub-pixel location). Before evaluating the similarity between reference and deformed subsets using the correlation criterion described previously, the intensity of these points with sub-pixel locations must be

provided. Thus, a certain sub-pixel interpolation scheme should be utilized. In the literature, various sub-pixel interpolation schemes including bilinear interpolation, bicubic interpolation, bicubic B-spline interpolation, biquintic B-spline interpolation and bicubic spline interpolation have been used. The detailed algorithms of these interpolation schemes can be found in numerical computing books [108]. However, a high-order interpolation scheme (e.g. bicubic spline interpolation or biquintic spline interpolation) is highly recommended by Schreier *et al* [109] and Knauss *et al* [110] since they provide higher registration accuracy and better convergence character of the algorithm than the simple interpolation schemes do.

3.7 Displacement Field Measurement

Due to the discrete nature of the digital image, the integer displacements with 1 pixel accuracy can readily be computed. To further improve displacement measurement accuracy, certain sub-pixel registration algorithms should be used [111]. Generally, to achieve sub-pixel accuracy, the implementation of 2D DIC comprises two consecutive steps, namely initial deformation estimation and sub-pixel displacement measurement. In other words, the 2D DIC method normally requires an accurate initial guess of the deformation before achieving sub-pixel accuracy. For example, for the most commonly used iterative spatial cross-correlation algorithm (e.g. the Newton–Raphson method), it only converges when an accurate initial guess is provided (the radius of convergence is estimated to be smaller than 7 pixels in the evaluation tests performed by Vendroux and Knauss [112]). As for the coarse–fine algorithm and the peak-finding algorithm, an integer displacement of 1 pixel resolution must be provided before further sub-pixel displacement registration. For this reason, the techniques for an initial guess of deformation are described first in this section.

3.7.1. Initial Guess of Deformation.

Usually, the relative deformation or rotation between the reference subset and the deformed subset is quite small, so it is easy to get accurate estimation of the initial

displacements by a simple searching scheme implemented either in spatial domain or in frequency domain. In spatial domain, the accurate locations of the target subset can be determined by a fine search routine, pixel by pixel, performed within the specified range in the deformed image. Some schemes, such as the coarse-to-fine and the nested searching schemes [113], can be used to speed up the calculation. These search schemes yield 1 pixel resolution. Alternatively, the correlation between the reference subset and the deformed subset can also be implemented in Fourier domain as conducted and advocated by Chen *et al* [114], Sojahal *et al* [115] and Hild *et al* [116]. In Fourier domain, the correlation between two subsets is calculated as the complex multiplication of the first subset's Fourier spectrum by the complex conjugate of the second subset's spectrum. Since the FFT can be implemented with very high speed, the Fourier domain correlation method is also extremely fast. However, the in-plane translation is implicitly assumed in the Fourier domain method, small strains and/or rotations occurring between the two subsets will lead to significant errors.

The above-mentioned technique performs well for most cases. Difficulties occur in certain cases when large rotation and/or large deformation presents between the reference and target subsets in which some pixels of the reference subset run out of the area of the assumed subset within the deformed image; consequently, the similarity between the reference subset and the assumed deformed subset will decrease substantially. As can be seen from figure 3.10(a), if only rigid body translation exists between the reference and deformed subsets, a single peak can be found in the correlation coefficient distribution. In contrast, while a 20° relative rotation occurs between the reference image and the deformed image, there will not be even a single sharp peak in the correlation distribution map as indicated in figure 3.10(b), and thus result in a failure in integer pixel displacement searching.

Other techniques are therefore required to achieve a reliable initial guess of deformation in these cases. Inspired by the nested coarse-fine algorithm presented by Zhang *et al* [113] that can provide an initial guess for each calculation point, a technique was presented by Pan *et al* [117] to achieve a reliable initial guess for the NR method for these cases. Slightly different from Zhang's work, this technique only provides the initial guess of the first calculation point. Then, based on the assumption of continuous deformation of solid object, the obtained result of the first point serves as the initial guess for the next point to be calculated. The initial guess of deformation is determined by manually selecting three or more points (x_i, y_i) ($i = 1, 2, \dots, n$, and $n > 3$)

with distinct features around the reference subset center, and their corresponding locations (x'_i, y'_i) ($i = 1, 2, \dots, n$, and $n > 3$) in the deformed image. Thus, the desired initial guess can be resolved from the coordinate correspondence (depicted by the first-order shape function) using the least-squares method. Alternatively, benefiting from the extraordinary ability of its global optimum, the genetic algorithm [118] can also be used as an automatic technique for determining the initial guess of the first calculation point. However, the genetic algorithm normally costs a lot of computation time to converge to the global extremum.

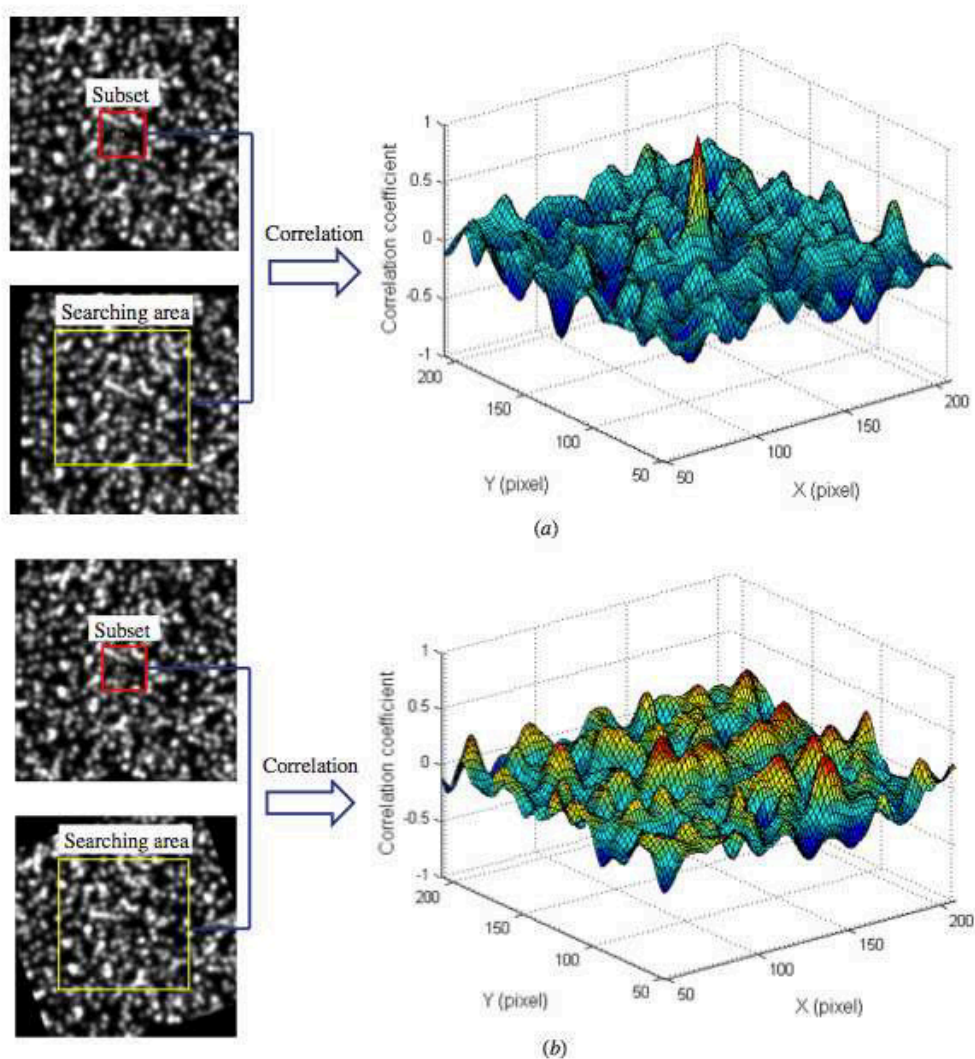


Figure 3.10: Computed whole-field cross-correlation coefficient distribution when the deformed image is subjected to (a) rigid body translation, and (b) 20° relative rotation.

3.7.2. Calculation Path.

As described in subsection 2.2.1, before the implementation of DIC analysis, ROI should be specified or defined in the reference image. The regularly spaced points within ROI are considered as points to be computed. Conventional correlation calculation generally starts with the upper-left point of the ROI. Then, the calculation analysis is carried out point by point along each row or column. Normally, to speed calculation and save computation time, the computed displacements and strains of the current point are used as the initial guess of the next point according to the continuous deformation assumption. In this sense, the conventional DIC computation is a path-dependent approach. Although we can estimate the initial guess separately for each point, however, this approach is either impractical because it is extremely time-consuming or impossible if large deformation and/or rotation presents in the deformed image. So, even though the well-established conventional DIC method is effective in most cases, this path-dependent approach may give rise to wrong results in the following cases. First, if the digital images of a practical test object contain discontinuous areas such as cracks, holes or other discontinuous area or if an irregular ROI is defined in the reference image, the transfer of the initial guess will fail to provide a reliable initial guess for the next point at some locations. Second, if apparent discontinuous deformation occurs in the deformed image, the transfer of the initial guess also fails. Third, occasionally occurring wrong data points will also provide a wrong initial guess for the next point. In all these cases, if one point is wrongly computed, the results of wrong points will be passed to the next point, which leads to the propagation of error.

More recently, a universally applicable reliability-guided DIC (RG-DIC) method has been proposed by Pan [119] for reliable image deformation measurement. In the method, a special coefficient is used to identify the reliability of the point computed. The correlation calculation begins with a seed point and is then guided by that coefficient. That means the neighbors of the point with the highest coefficient in a queue for the computed points will be processed first. Thus, the calculation path is always along the most reliable direction and possible error propagation of the conventional DIC method can be entirely avoided. The RG-DIC method is very robust

and effective. It is universally applicable to the deformation measurement of images with area and/or deformation discontinuities.

3.7.3. Sub-Pixel Displacement Registration Algorithms

The techniques described above only provide displacements with pixel level accuracy or approximated initial guess of the deformation vector. To further improve the accuracy of DIC, a certain kind of sub-pixel registration algorithm should be used. In the following, various sub-pixel registration algorithms proposed in the literature are introduced and discussed.

3.7.3.1. Coarse–fine Search Algorithm.

In the determination of integer-pixel displacement, the search method searches the specified searching area of interest with 1 pixel step to find the point with maximum cross-correlation coefficient. It is straightforward to change the search step into 0.1 pixels or 0.01 pixels to achieve a sub-pixel accuracy of 0.1 pixels or 0.01 pixels, respectively [94, 120]. Usually the zero-order shape function is implicitly used in the coarse–fine searching algorithm while implementing the direct searching scheme. The gray level at sub-pixel locations must be reconstructed in advance using certain interpolation scheme, which generally costs long computation time. Some work [113] has been done to reduce the computation cost and the probability of mis-identification of the traditional coarse–fine search algorithm. Nevertheless, compared with the next two algorithms, the coarse–fine method is still time-consuming.

3.7.3.2. Peak-finding Algorithm.

The peak-finding algorithm refers to a class of algorithms for detecting the peak position of the local discrete correlation coefficient matrix (typically, 3×3 or 5×5 pixels) around the pixel with maximum CC coefficient or minimum SSD coefficient

after the integer-pixel displacement searching scheme. Both least-squares fitting and interpolation algorithms can be used to approximate the local correlation coefficient matrix, and the peak position of the approximated curve surface is taken as the sub-pixel displacements. For example, Chen *et al* [114] proposed a biparabolic least-squares fitting of the local peak and define the peak position to be the extremum of the obtained polynomial; Sjodahl *et al* [115] used the algorithm by expanding the discrete correlation function in terms of a Fourier series first, followed by a numerical searching scheme to find the exact peak; Hung *et al* [121] and other researchers [122–127] employed a two-dimensional quadratic surface fitting of the peak and the sub-pixel displacements are defined based on the location of the maximum value of the fitting surface; and more recently, Wim *et al* [128] computed the sub-pixel displacements by simply calculating the center of mass localization of the discrete correlation matrix. The principle and implementation of peak-finding techniques for sub-pixel displacement measurement is simple, it can be done very fast. However, the peak-finding algorithms do not consider the shape change of the deformed subset, and just compute the approximated peak rather than the actual peak of correlation coefficient; as a consequence, the accuracy is lessened [111, 121].

3.7.3.3. Genetic Algorithms.

As a random search algorithm with robust global converge capability, the genetic algorithm is widely used to optimize the multi-dimensional nonlinear function, and it was also introduced into the 2D DIC method to optimize the correlation criterion for determination of deformation parameters [117]. To detect a global optimum deformation vector for the objective function (i.e. correlation criterion), an initial population containing N candidate individuals (i.e. deformation parameter vector) is randomly generated within its possible range, and then the objective function cost function is evaluated for all the candidate individuals. The best individuals are kept and the worst discarded, and some new individuals are also randomly generated to replenish the population. Subsequently, some schemes, such as crossover, mutation and recombination, are used to generate a new population from the last population and the objective function is evaluated again for all the candidate individuals. These

processes are repeated until the converging conditions are satisfied. Although with extraordinary ability of global optimum, the genetic DIC method generally requires a long computation cost to find the global extremum of the correlation coefficient.

3.7.3.4. Finite Element Method and B-spline Algorithm.

The above-mentioned algorithms determine the displacements for each subset center independently and can be considered as a pointwise algorithm. Quite different from these pointwise algorithms, a continuum method (or a global method), in which the surface deformation of the test object throughout the entire image area was represented by the B-spline function, was proposed by Cheng *et al* [129]. In addition, the so-called Q4-DIC developed by Besnard *et al* [130] and the finite element formulation proposed by Sun *et al* [131] can also be categorized into a global method. These techniques ensure the displacement continuity and displacement gradients continuity among calculation points. Thus, they declared that the mismatching of points can be avoided. However, from the reported results, these two methods seem not to provide higher displacement measurement accuracy than the NR algorithm.

Although various algorithms can be used to achieve sub-pixel displacement, it is worth noting that the most widely used two algorithms in various literature are the iterative spatial domain cross-correlation algorithm and the peak-finding algorithms, due to their simplicity. However, after evaluating their displacement measurement accuracy and precision using computer simulated speckle images with controlled deformation, the iterative spatial domain cross-correlation algorithm with higher accuracy, best stability and broader applicability is highly recommended for practical use [111].

CHAPTER 4

FATIGUE CRACK PROPAGATION IN NITI BASED SYNGLE CRYSTAL SHAPE MEMORY ALLOYS

4.1. Introduction.

Compared with the total life approach to fatigue of Nitinol, relatively few studies have been conducted to evaluate the damage tolerant properties, i.e. the fatigue crack growth and fracture toughness behavior. One reason for this is that currently the Nitinol industry is dominated by commercial products with geometrically small feature sizes where the emphasis is placed on preventing fatigue crack nucleation rather than controlling crack growth. Not only is it difficult to experimentally measure crack growth rates accurately in such physically small components, but once a macroscopic crack nucleates and starts growing, failure generally ensues shortly afterwards. For example, a stent with a typical strut width of 0.2 mm cycled at 1 Hz (heart rate) may require only hours or days for a crack to fully propagate through the wall once nucleated. Indeed, in those cases, it is important to screen, and reject, devices for surface flaws that are larger than the critical crack length for such propagation, which in stents is typically about 15–50 mm. Provided that those geometrically small devices do not have flaw sizes larger than this critical crack length, then the total life approach to fatigue evaluation is more appropriate. The damage tolerant approach to fatigue is most appropriate when the product is in a stress controlled environment and its geometric size is large enough to sustain stable crack growth for many thousands of cycles and over a long enough time period to retain functionality of the device over its lifetime despite the presence of a growing crack, or when devices cannot be adequately examined and rejected for surface flaws exceeding the critical crack length. In today's commercial landscape, there are few Nitinol products that meet such a description. However, damage tolerant analyses are useful as a compliment to a total life approach. Specifically, whereas stress/strain life data should be employed to provide the primary basis for life prediction in most medical devices, damage tolerant analyses can be used as secondary life prediction methodology that can additionally assess, in the quantitative way, the effect of the presence of defects in terms of reduced

performance/lifetimes. Moreover, the commercial landscape may change in the future, and require the implementation of damage tolerant techniques as the primary life prediction strategy. Indeed, the orthopedics community is beginning to adopt Nitinol for in vivo skeletal stabilizing devices (in a stress controlled environment) that have geometries on the order of several centimeters, where the damage tolerant analysis is more relevant.

Starting from the pioneer work of Melton and Mercier [55], where, for the first time, the fatigue crack propagation in NiTi Smas has been analyzed, others relevant contributes have been proposed during the years. Crack propagation behavior in stable (with no phase transformation) and unstable (with transformation) structures has been analyzed in [76-78,132-137], In particular an accurate evaluation of the threshold has been studied in [133], while the effect of the temperature and environmental operating conditions have been studied in [76-78], where cylindrical specimens, with dimensions approaching the endovascular stents, have been adopted. Furthermore, the effect of the crystallographic texture [135], and material form and microstructure [137], has been analyzed.

However, due to complexity of the problem, related to the particular behavior of this class of material, not many efforts have been done to deeply understand the fatigue crack propagation response, and most of research has been focused on the pseudoelastic microstructure.

For this reason, in order to identify a lower and upper bound, in terms of da/dN vs ΔKI , for this class of material, fatigue crack propagation tests, for the stable austenite and stable martensite structure, have been carried out.

Furthermore, with the aim to generate effective crack propagation laws, single crystal specimens and the Digital Image Correlation (DIC), based on the measurement of the displacement field, have been adopted.

4.2. Material and Experimental Procedure

Single crystal edge-notched tension specimens, obtained from a Ti-Ni 50.1% plate by electrical discharge machining (EDM), were tested in this study.

The [012] crystallographic orientations, determined by using the X-Ray Diffraction (XRD) technique, was investigated. Each specimen was previously solutionized in order to reduce precipitates and residual stresses and then they were heat treated at 450°C for 100hr in order to get a stable martensitic structure at room temperature. The new characteristic transformation temperatures, table 4.1, were obtained by Differential Scanning Calorimetry (DSC) thermography.

Table 4.1

Transformation temperatures of the heat treated material.

Transformation	Temperature [°C]
Austenite → Martensite (start) M_s	45
Austenite → Martensite (finish) M_f	55
Martensite → Austenite (start) A_s	30
Martensite → Austenite (finish) A_f	25

The mechanical properties, in terms of critical stress, figure 4.1a, and elastic modulus, figure 4.1b, were calculated by means of monotonic tests performed at different temperatures. As a consequence of the heat treatment, the material manifested a stable martensitic behavior at room temperature and a stable austenitic behavior, with no phase transformation, at 80°C.

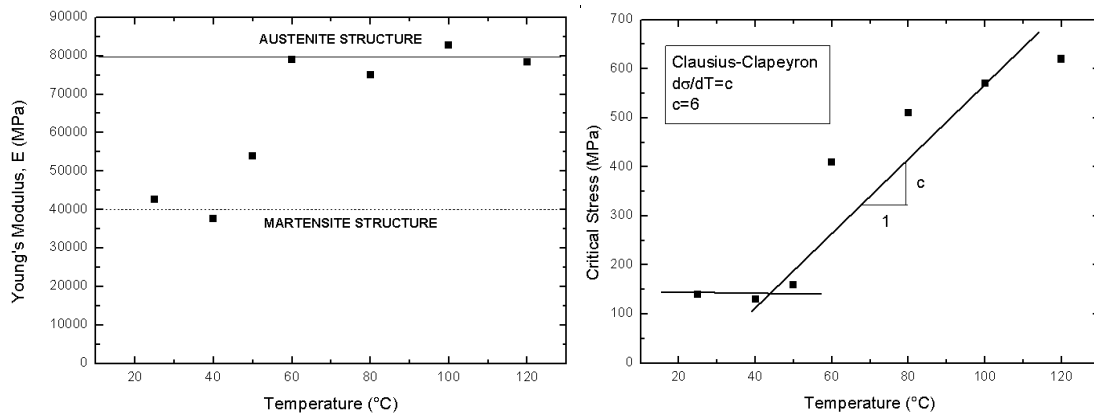


Figure 4.1: mechanical properties of the specimens analysed; a) elastic modulus in function of the temperature, b) critical stress in function of the temperature.

Fatigue tests were performed in load control with a fix stress ratio ($R = \sigma_{min} / \sigma_{max}$) and a rate of 5 Hz to initiate a crack at the notch.

Fatigue Crack Propagation in NiTi Based Single Crystal Shape Memory Alloys

The specimens were polished to a mirror finish using abrasive paper. Black paint was then airbrushed onto each specimen to create a speckle pattern for digital image correlation (DIC). For a description of the digital image correlation technique, see [138]. A digital camera was used to capture images during the fatigue crack growth experiments. The camera resolution was 1600 by 1200 pixels, the maximum frame rate was 15 fps, and an adjustable lens with a 12X magnification range and 2X adapter was used. The experimental setup is shown in figure 4.2. The properties of each specimen and test procedure are displayed in table 4.2.

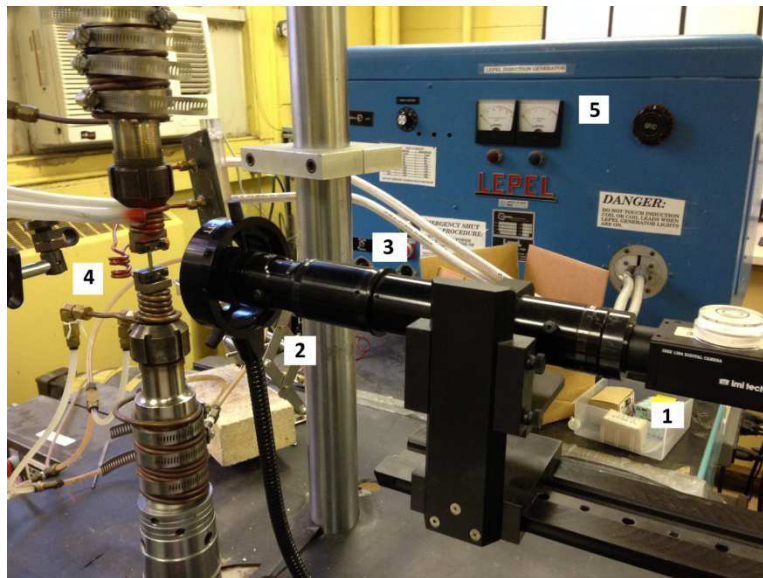


Figure 4.2: The experimental setup. Labeled in the figure: (1) camera, (2) light source, (3) lens, (4) specimen, and (5) thermal induction equipment.

Table 4.2

Summary of the specimen dimensions, testing conditions, and equipment setup.

Crystallography orientation	Temperature [°C]	Thickness [mm]	R ratio	Stress Range [MPa]	Magnification	Resolution [$\mu\text{m}/\text{pix}$]
[0 1 2]	20	1.19	0.1	54	2.73	1.61
[0 1 2]	20	1.16	0.1	54	2.76	1.60
[0 1 2]	80	1.15	0.1	54	2.71	1.62
[0 1 2]	80	1.18	0.1	54	2.75	1.64

Fatigue Crack Propagation in NiTi Based Single Crystal Shape Memory Alloys

A computer program controlled the servo-hydraulic load frame, and captured images and their corresponding loads measured by a 10 kN load cell during the test. Once a crack was visually identified, measurement cycles were run periodically, at 0.25 Hz, to capture a greater number of images per cycle to provide an in-depth analysis into the fatigue cycles.

A commercially available image correlation program was used to perform DIC analysis. The first image of each measurement cycle, captured at minimum load, was used as the reference image for that cycle. The full field of the image, both behind and ahead of the crack tip, was used for correlations. A two-point digital image correlation displacement gage (virtual extensometer), which consists of a subset on each crack flank, was used to measure crack opening displacements; multiple digital extensometers were placed on the image along the length of the crack spanning from the crack tip to the notch [139-140], as shown in figure 4.3. Subset sizes of 21 by 21 pixels were used. A typical gage length was 50 μm , and gages used in this work were placed from 200 μm ahead of the crack tip. Each set of extensometer provided an accurate displacement profile behind the crack tip, and the crack opening displacement calculated at the tip allowed to identify the evolution of the elastic properties of the martensitic structure.

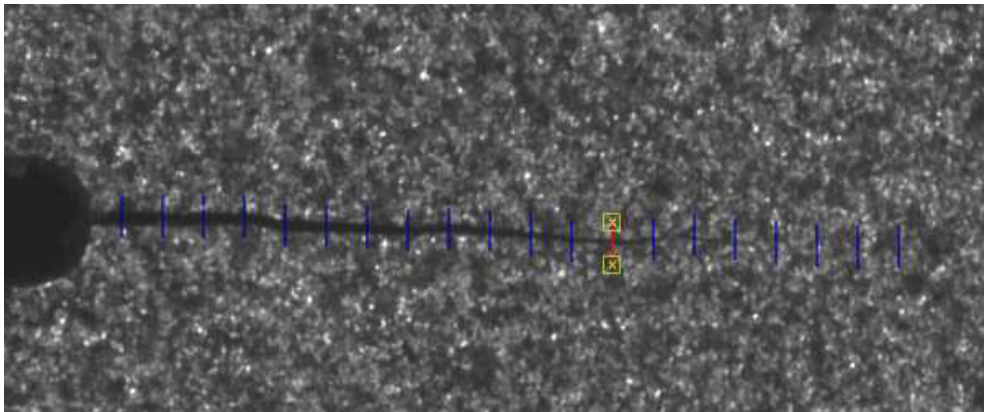


Figure 4.3: Illustration of DIC displacement gages across open crack faces. Each gage consists of two subsets one on each of the crack flanks.

4.3. Digital Image Correlation (DIC) Analysis

Fatigue crack propagation tests were performed in order to better understand the behavior in the stable structures of the NiTi single crystal alloy. Two different values of temperature, 20°C and 80°C, were adopted during the tests in order to get, respectively, the martensitic and austenitic stable behavior of the material.

To determine the effective stress intensity factor the specimen actually experiences, which could be different than the theoretical load-based stress intensity factor primarily due to crack closure, a least squares regression was performed on the DIC measured displacements.

The displacement field, at the crack tip, proposed by Williams [141], and modified by Shah [142], was used to fit the experimental data obtained from the tests.

As the displacement field is not unique unless rigid body motion is also specified, three in-plane rigid motion terms, rotation, A , rigid translation parallel to the crack line, B_u , and rigid translation perpendicular to the crack line, B_v have to be specified. Furthermore, due to the low magnitude of the pictures [143], if the T-stress term is included, in order to improve the fitting the analytical and experimental results, the asymptotic crack tip displacement equations become:

$$\begin{aligned}
 u = & K_I \sqrt{\frac{2r}{\pi}} \operatorname{Re} \left[\frac{1}{\mu_1 - \mu_2} \{ \mu_1 p_2 \sqrt{\cos \theta + \mu_2 \sin \theta} - \mu_2 p_1 \sqrt{\cos \theta + \mu_1 \sin \theta} \} \right] \\
 & + K_{II} \sqrt{\frac{2r}{\pi}} \operatorname{Re} \left[\frac{1}{\mu_1 - \mu_2} \{ p_2 \sqrt{\cos \theta + \mu_2 \sin \theta} - p_1 \sqrt{\cos \theta + \mu_1 \sin \theta} \} \right] \\
 & + a_{11} T r \cos \theta + A r \sin \theta + B_u \\
 v = & K_I \sqrt{\frac{2r}{\pi}} \operatorname{Re} \left[\frac{1}{\mu_1 - \mu_2} \{ \mu_1 q_2 \sqrt{\cos \theta + \mu_2 \sin \theta} - \mu_2 q_1 \sqrt{\cos \theta + \mu_1 \sin \theta} \} \right] \\
 & + K_{II} \sqrt{\frac{2r}{\pi}} \operatorname{Re} \left[\frac{1}{\mu_1 - \mu_2} \{ q_2 \sqrt{\cos \theta + \mu_2 \sin \theta} - q_1 \sqrt{\cos \theta + \mu_1 \sin \theta} \} \right] \\
 & + a_{12} T r \cos \theta + A r \cos \theta + B_v
 \end{aligned}$$

Details are reported in [144].

Fatigue Crack Propagation in NiTi Based Single Crystal Shape Memory Alloys

Because of the different microstructure, between twinned martensite and austenite, a different approach was adopted to measure the propagation rate, from eqn. 1. The presence of variants randomly distributed in the martensitic phase, gives the material isotropic behavior, while horthotropic properties are associated to the austenite. Therefore, when the regression was performed on the martensitic specimen, isotropic compliance coefficients were used.

The experimentally obtained and regressed displacements were plotted together to demonstrate the accuracy of the regression technique. In figures 4.4-4.5, the blue contours represent the experimentally found displacements and the red contours represent the regressed displacement contours. A selected fatigue cycle for each sample tested is presented at maximum load. In the analysed cases a little inclined path was observed during the crack propagation, but the maximum calculated inclination was of 7° with a mode II stress intensity component less than one order of magnitude compared with the obtained KI. For this reason the effect of the shear component was neglected.

The displacement fields, vertical and horizontal, for the martensitic and austenitic specimen are given in Figs. 4.4-4.5a and 4.4-4.5b, respectively. The experimental and regressed displacement contours show good agreement.

The horizontal displacements are pretty symmetric indicating that mode II displacement, occurring during the cycle, is negligible.

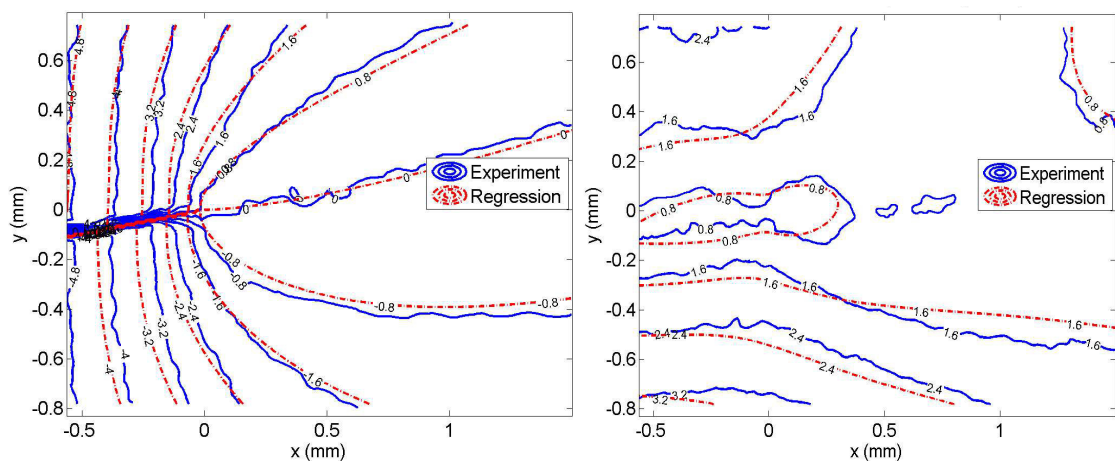


Figure 4.4: martensitic structure; comparison of experimentally measured and regression a) v -displacement contours and b) u -displacement contours

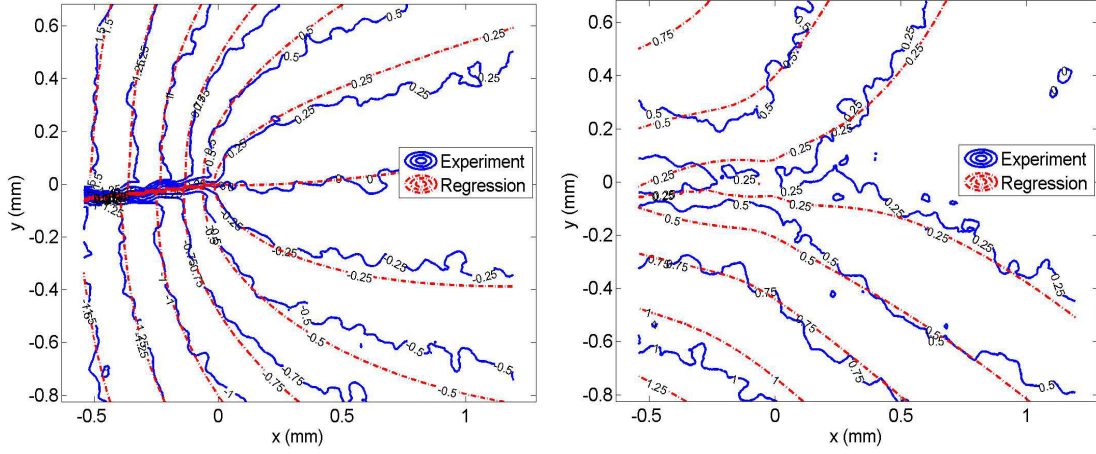


Figure 4.5: austenitic structure; comparison of experimentally measured and regression a) v -displacement contours and b) u -displacement contours

4.4. Fatigue Crack Propagation

Effective fatigue crack propagation curves, based on the mode I effective stress intensity factor ranges, obtained from the least square regressions, were made. Each trend was compared with the one proposed by the Linear Elastic Fracture Mechanic (LEFM), where the stress intensity factor range can be calculated as:

$$\Delta K_I = \Delta\sigma\sqrt{\pi a} \cdot f\left(\frac{a}{w}\right) \quad (4.2)$$

where $\Delta\sigma$ is the normal stress range on the crack plane, a is the crack length, and $f(a/w)$ is the geometric correction factor. The stress intensity factor was measured in $\text{MPa}\sqrt{\text{m}}$. For a single-edge notch tension specimen, the geometric correction factor is given as [145]:

$$f\left(\frac{a}{w}\right) = 0.265 \cdot \left(1 - \frac{a}{w}\right)^4 + \frac{0.857 + 0.265 \cdot \left(1 - \frac{a}{w}\right)}{\left(1 - \frac{a}{w}\right)^{\frac{3}{2}}} \quad (4.3)$$

where a is the crack length and w is the specimen width.

Fatigue Crack Propagation in NiTi Based Single Crystal Shape Memory Alloys

Results, obtained for each case, are reported in figures 4.6-4.8. It is important to underline that, for a first attempt, the effective elastic properties ($E_M=40$ GPa, $E_A=80$ GPa), figure 4.1a, were adopted in eqn. 1 to fit the experimental data.

As reported in [77], where the effective crack propagation in NiTi shape memory alloys was studied, the martensitic structure manifests an higher value of the threshold stress intensity factor range than the austenite. In particular a $\Delta K_{I_{th}}=1.4$ MPa \sqrt{m} was recorded for the austenite and a $\Delta K_{I_{th}}=3.3$ MPa \sqrt{m} was obtained for the martensitic material. Similar results are reported in [77]. Different behavior is shown in [77], where the austenite manifested an higher value of threshold than the martensite, and, as also reported in [132-134], where only the martensitic structure was analysed, higher values of the threshold ranges were recorded. In these studies, however, a LEFM approach was adopted and these results are quite similar with the one showed in figure 4.6 and 4.7 obtained with the same approach.

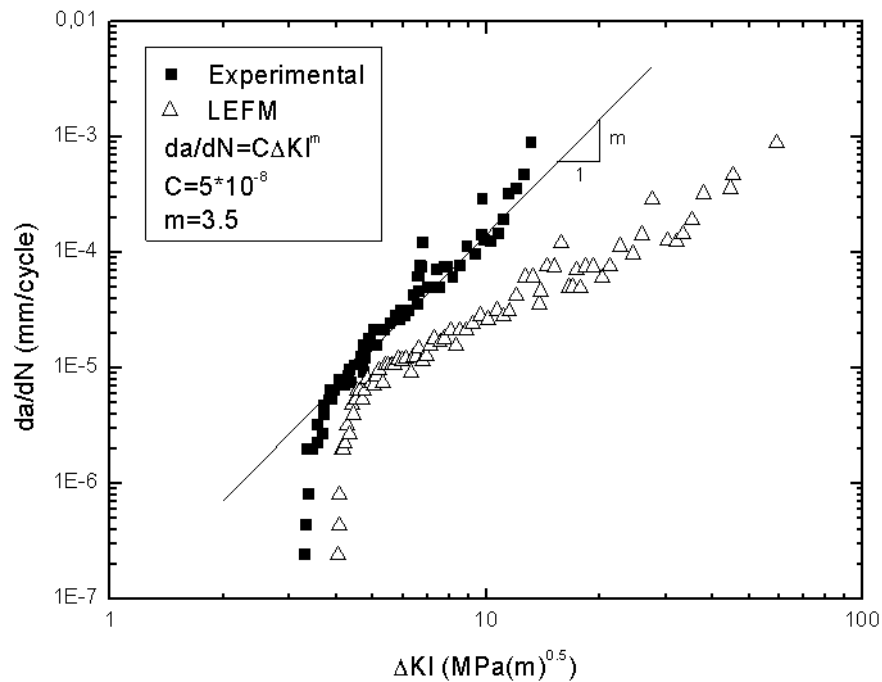


Figure 4.6: martensitic structure; crack propagation behavior calculated using the digital image correlation (DIC) and the linear elastic fracture mechanics (LEFM).

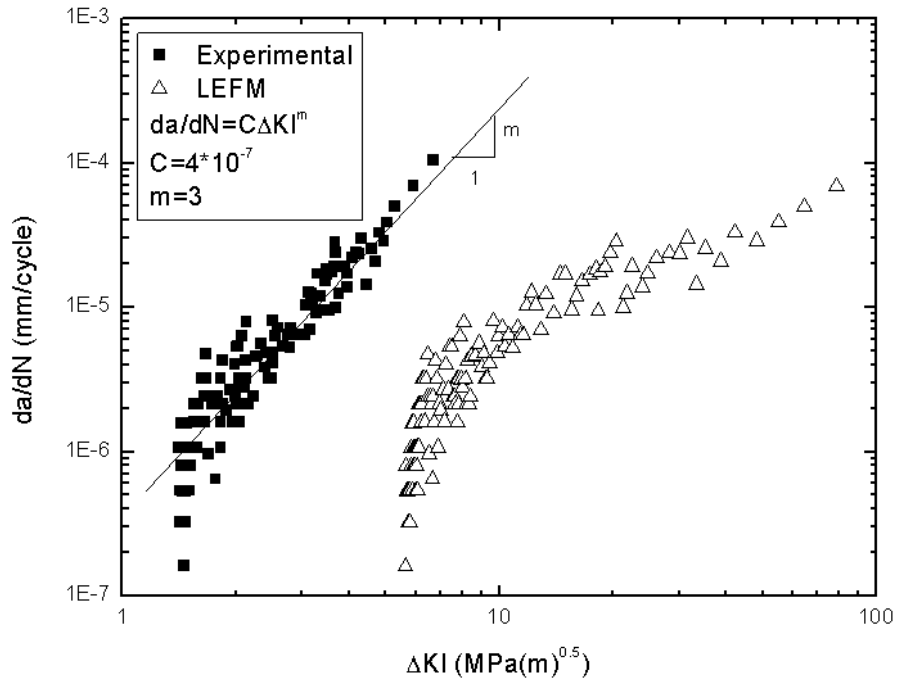


Figure 4.7: austenite structure; crack propagation behavior calculated using the digital image correlation (DIC) and the linear elastic fracture mechanics (LEFM).

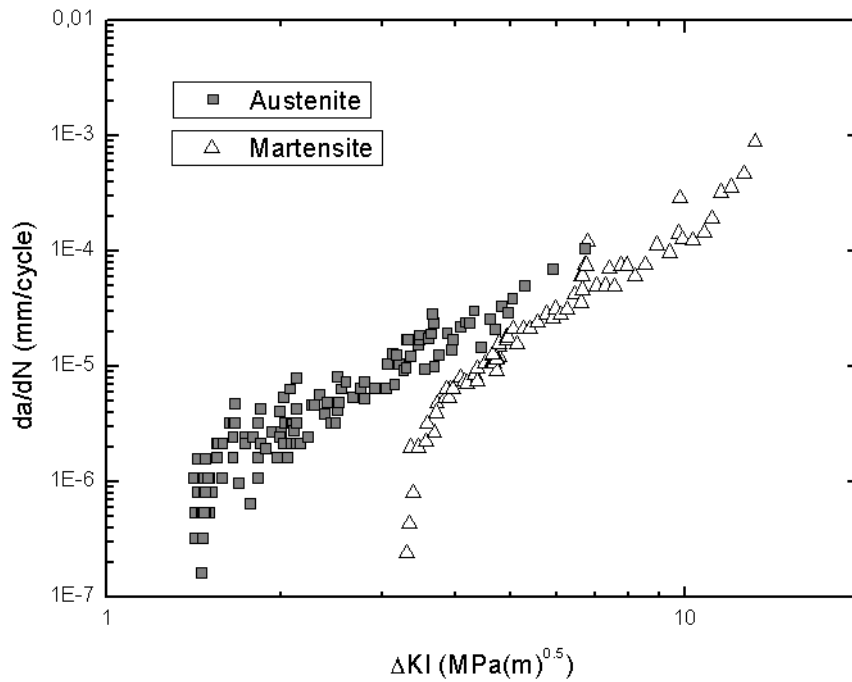


Figure 4.8: comparison between the crack propagation behavior of austenitic and martensitic structures.

4.5. Fatigue Crack Closure

DIC displacement gages were used to measure crack opening displacements along the crack length. The opening displacement is defined here as the difference between the vertical displacement recorded on each couple of subsets located in the opposite sides of the crack length, figure 4.3. Shearing displacements were found to be extremely small (one order of magnitude less than opening displacements), for this reason they were neglected.

Figure 4.9 and 4.10 show the crack opening obtained for different crack length, for the martensitic and austenitic microstructure, respectively.

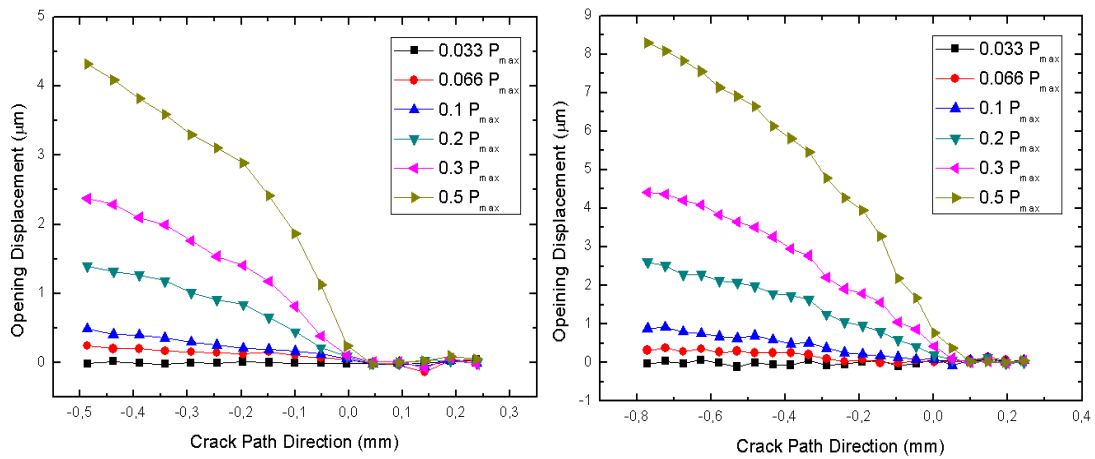


Figure 4.9: crack opening displacement calculated on the martensitic structure; a) crack length $a=1.14$ mm and stress intensity factor $KI=5.32$ $MPa\sqrt{m}$, b) crack length $a=1.78$ mm and stress intensity factor $KI=8.38$ $MPa\sqrt{m}$

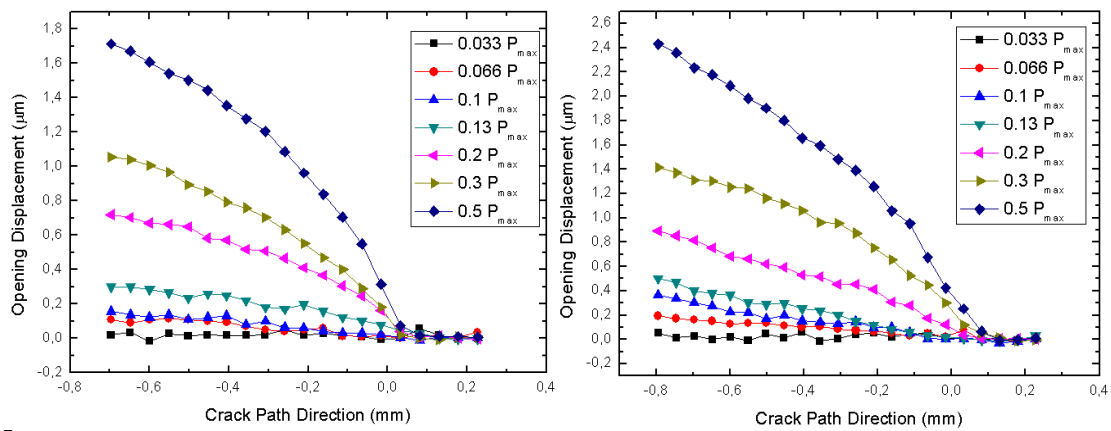


Figure 4.10: crack opening displacement calculated on the austenitic structure, a) crack length $a=1.2$ mm and stress intensity factor $KI=3.1$ $MPa\sqrt{m}$, b) crack length $a=1.71$ mm and stress intensity factor $KI=4.14$ $MPa\sqrt{m}$.

Fatigue Crack Propagation in NiTi Based Single Crystal Shape Memory Alloys

As shown in the figures 4.10, the austenitic structure manifested a typical behavior of the common engineering metals, where, due to the plastic zones generated behind the crack tip, the crack, for a length far from the notch, appears open by 20% of the peak load. Instead, due to the numerical noise related to the low resolution of the pictures, no clear results were obtained for the shortest crack, but, in any case no opening should be expected during this time.

On the contrary, no opening effect was observed in the martensitic specimen, where the crack seems to be always opened till a length $a=1.8$ mm, after that it appears close until the 6% of peak load.

This latter result seem to be not in agreement with the crack propagation behavior showed in figure 4.6, where, due to the difference of the LEFM and the effective stress intensity factor, the opening effect should be expected. This behavior can be related to the elastic properties of the martensitic material at the crack tip. In fact the high stress at the crack tip tends to reorient the twinned variants, previously randomly distributed, in the most favorable applied stress direction. This new distribution implies a change in the elastic properties at the crack tip with an increase of the Young's Modulus due to the new allignment of the variants. Figure 4.11 explains well this phenomena.

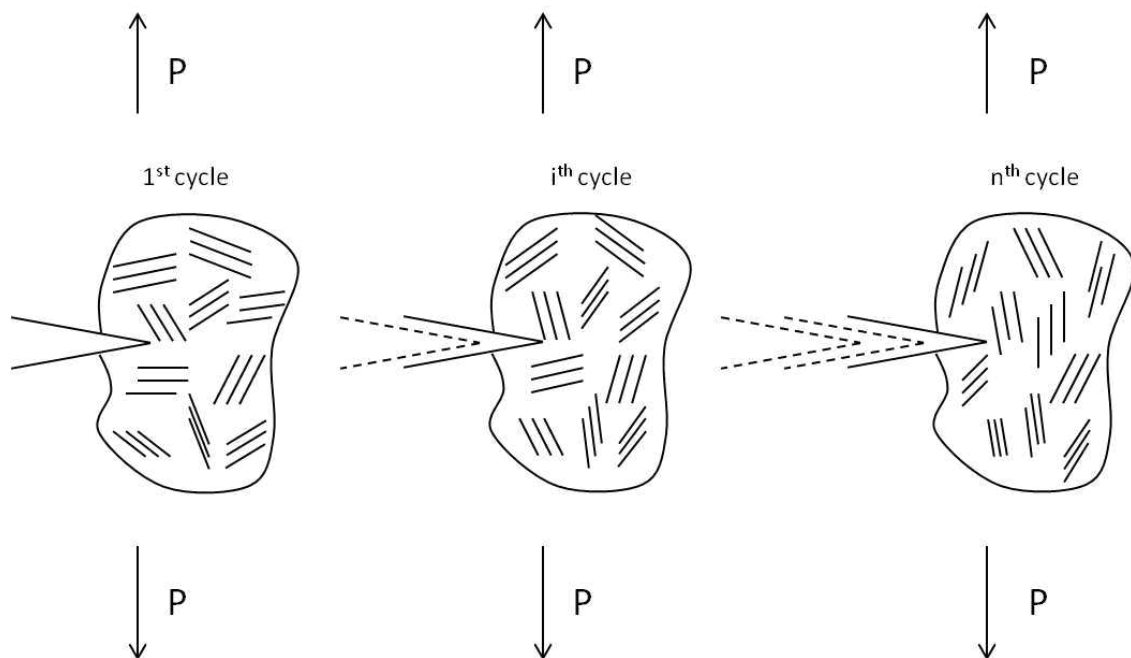


Figure 4.11: evolution of the martensitic variants distribution during the load history.

Fatigue Crack Propagation in NiTi Based Single Crystal Shape Memory Alloys

In the first cycle the variants at the crack tip are randomly distributed and the Young's Modulus is the effective one recorded during the monotonic test, figure 4.1a. When the crack starts to propagate it will grow in a new structure characterized by partially distributed variants with new higher elastic properties. In the end of its life, the crack will be immersed in a new structure with completely distributed variants, where the elastic modulus is the one of a pure NiTi martensitic single crystal.

In order to better understand this phenomena, crack tip opening displacement range was used as a physically measurable fracture mechanic parameter to characterize crack growth. In particular the experimental values were compared with the theoretical one, expressed as:

$$\Delta\delta = \frac{(\Delta K_{I_{max}} - \Delta K_I)^2}{2ES_0} \quad (4.4)$$

where, for each cycle, ΔK_{max} is the maximum recorded stress intensity factor, ΔK is the value recorded after unloading, E is the Young's Modulus and S_0 is the critical stress. Figure 4.12 reports the comparison between them where no agreement was shown. In particular, for the shortest crack lengths, the calculated trend approaches the expected one, instead, when the crack is longer the curves start to diverge. This result confirms that a change in the elastic properties, eqn xx, should be expected during the crack propagation.

For this reason a numerical approach was adopted that, by a proper selection of the elastic properties, allows to match theory and experiments. Details are reported in figure 4.13.

In particular, the experimental crack tip opening displacements, previously calculated, figure 4.12, were given as first input (step 2). For each case a trial Young's Modulus value was chosen (step 3), by which a new effective stress intensity factor range (step 4) and, consequently, a new tip crack opening displacement (step 4), by means of the eqn xx, was calculated. The procedure was stopped when the theoretical results matched the analytical one, figure 4.14.

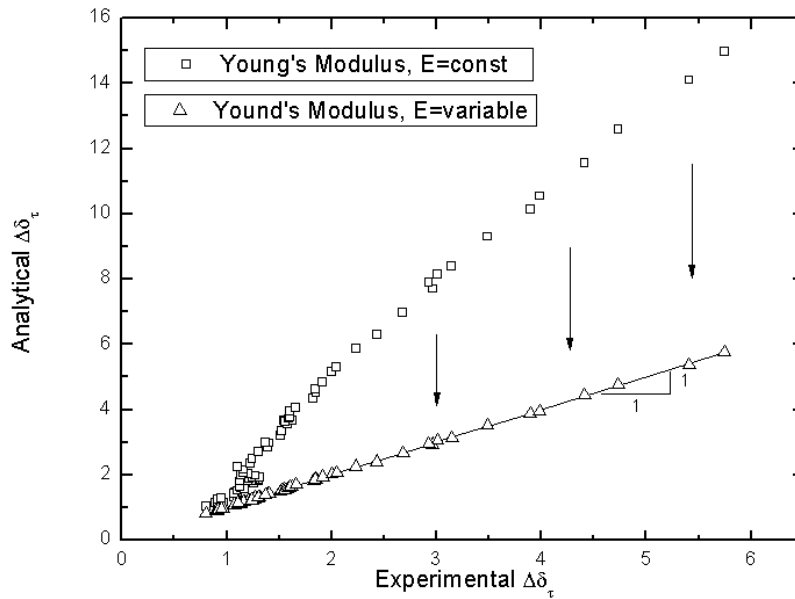


Figure 4.14: experimental and analytical crack opening displacement results: comparison between the one obtained with a fixed value of the Young's Modulus at the crack tip and the one obtained with variable elastic properties, for the martensitic structure.

This approach provided a new evolution of the elastic properties, in terms of Young's Modulus, at the crack tip, figure 4.15. In particular, at the beginning of the test, when the twinned zone at the crack tip is not very large, the value seems to be very close to the effective one revealed by the monotonic test performed in an undeformed specimen characterized by a random distribution of the variants; when the crack grows the elastic modulus increases, meaning that a redistribution of the martensitic variants, along the load direction, is happening; in the end of the crack life, the modulus stabilizes at its maximum value, meaning that all the variants are completely reoriented.

This results allowed to evaluate, replacing in eqn xx the new calculated elastic moduli, a new trend of the crack propagation for the martensitic material, figure 4.16. In particular the new curve lies between the lower (effective Young's Modulus, $E=40$ GPa) and the upper (pure single crystal Young's Modulus, $E=120$ GPa) boundary, and its trend seems to show a good agreement with the LEFM calculated behavior, figure 4.17. This latter result justifies the reason why no closure effect was shown with the virtual extensometer analysis.

Fatigue Crack Propagation in NiTi Based Single Crystal Shape Memory Alloys

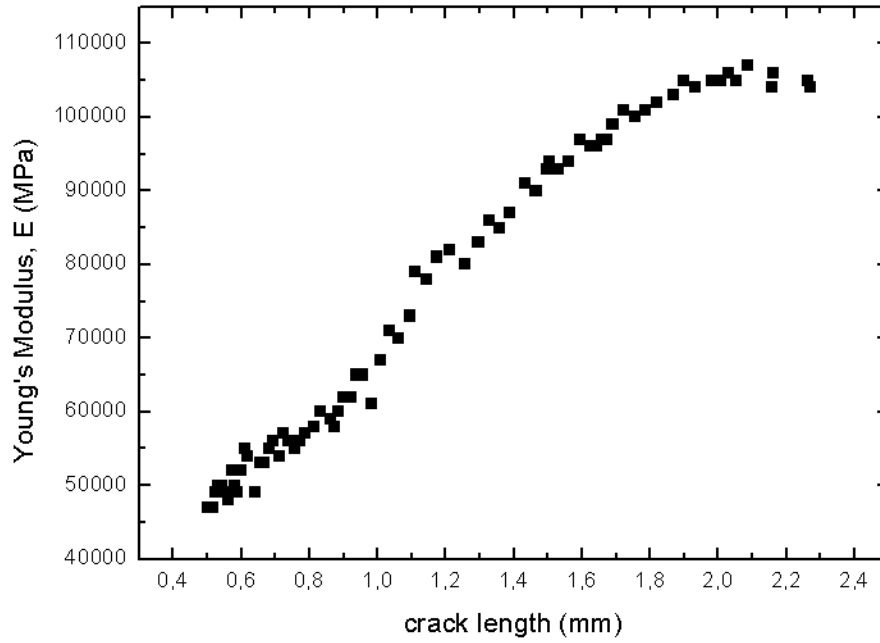


Figure 4.15: calculated evolution of the elastic properties in the martensitic structure.

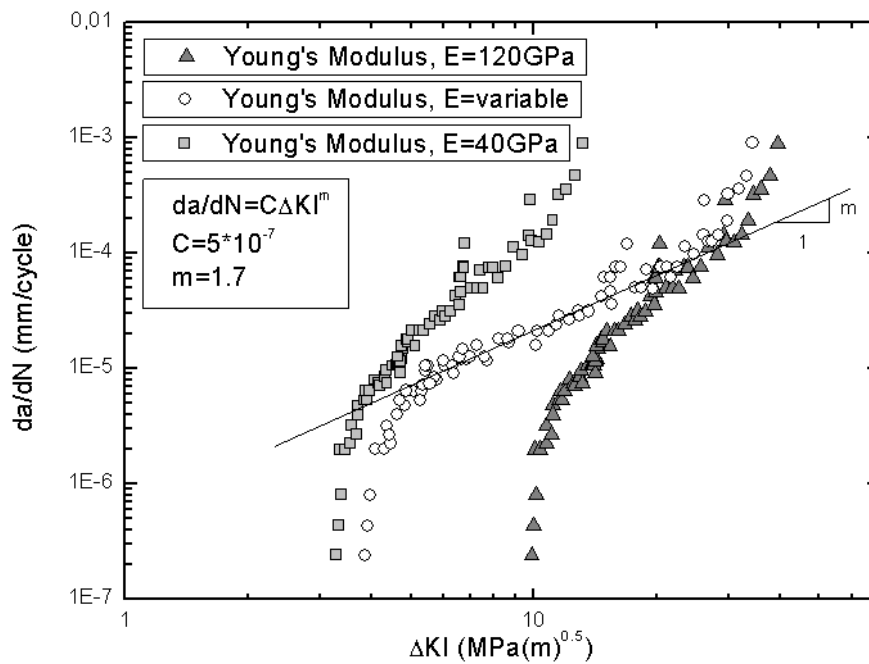


Figure 4.16: crack propagation behavior of the martensitic structure obtained by using variable elastic properties at the crack tip.

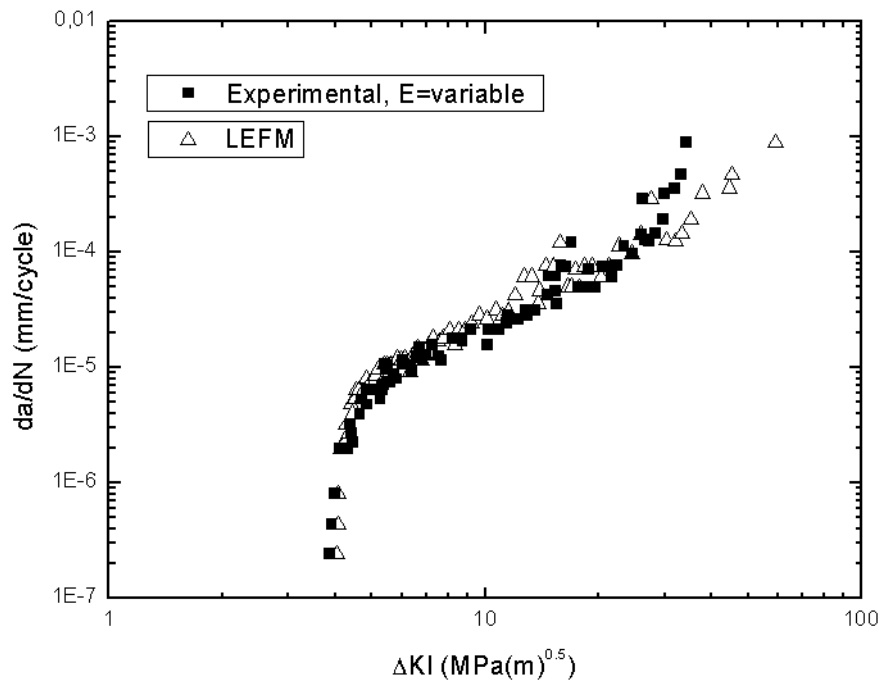


Figure 4.17: comparison between the crack propagation behavior of the martensitic structure, obtained by using variable elastic properties at the crack tip, and the one calculated with the linear elastic fracture mechanics (LEFM).

4.6 Summary

Fatigue crack propagation test have been performed in this investigation. Single crystal NiTi shape memory alloys have been tested in stress control at $25^{\circ}C$ and $80^{\circ}C$, in order to get a stable martensitic and austenitic structure, respectively. Results revealed that martensite has higher resistance to crack propagation than austenite, and that, at its crack tip, there is an evolution of the elastic properties due to the reorientations of its variants

CHAPTER 5

CRACK TIP STRESS DISTRIBUTION AND STRESS INTENSITY FACTOR IN NITI SHAPE MEMORY ALLOYS

5.1. Introduction

As already discussed in chapter 2, NiTi alloys exhibit unusual fatigue and fracture responses with respect to common metals because of the stress-induced martensitic transformation, occurring in the crack tip region as a consequence of the high values of local stress. For this reason much research must be carried out for a better understanding of these properties. In fact, it is widely accepted from the scientific community that stress-induced martensite plays a significant role in the mechanisms associated with crack formation and propagation, as demonstrated in several recent studies. In particular, both the fatigue crack propagation [135-136] and the fracture properties under static loadings have been analyzed [146-153]. In some of these works, the stress-induced phase transition mechanisms near the crack tip have been directly observed by synchrotron X-ray microdiffraction analysis [135, 148, 151], digital image correlation [149] and infrared thermography [152]. To better understand the role of these mechanisms, some numerical studies have been carried out, by using standard finite element (FE) codes and plasticity concepts [154-156] as well as by special constitutive models for SMAs [157-158] and cohesive zone models [159].

Even if these works provide very interesting and useful information on fracture properties of SMAs, most of them are based on linear elastic fracture mechanics (LEFM) concepts [149-153], i.e. standard procedures to calculate the fracture toughness of common engineering materials are used, without taking into account the stress-induced phase transition mechanisms in the crack tip region. As a consequence, a direct transferability of the results to the engineering community is not possible, and proper design criteria that are consistent with the unique properties of NiTi SMAs should be developed. To this aim, some analytical models have been proposed recently [160-171], which are mainly based on modified LEFM concepts.

In the present work, the fracture properties of a commercial pseudoelastic NiTi alloy (Type S, Memry, USA) have been investigated by analytical studies, FE simulations and experimental measurements. In particular, single edge crack (SEC) specimens have been analyzed for different values of the testing temperature in the pseudoelastic regime of the alloy. The phase transition mechanisms occurring in the crack tip region, together with the resulting stress distribution, have been analyzed by a recent analytical model [167-169] as well as by FE simulations, carried out by using a special constitutive model for SMAs. Finally, experimental measurements have been carried out, by using SEC specimens obtained from NiTi sheets by electro-discharge machining (EDM). The results have been analyzed by LEFM theory, and the analytical model has been used to calculate modified stress-intensity factors for SMAs.

5.2. Fracture Mechanics in Smas: Basic Mechanisms and Analytical Modelling

The stress-induced phase transformation mechanisms occurring near the crack tip of SMAs cause a unusual stress distribution, if compared with common engineering metals, as schematically shown in figure 5.1.

In particular, three different regions are observed near the crack tip: (1) a fully transformed martensitic region at the very crack tip, for $r < r_M$, (2) a transformation region, for $r_M < r < r_A$, and (3) an austenitic untransformed region for $r > r_A$. Furthermore, because of the large strain caused by the martensitic transformation as well as to the intrinsic different elastic properties of the two phases, the resulting crack tip stress distribution is significantly different with respect to the predictions of LEFM, and consequently, well-known fracture mechanics theories for common engineering metals cannot be directly applied to SMAs. To this aim, a recent analytical approach has been used [167-169], which is based on modified LEFM relations and on the assumption of small scale yielding, and it is capable to describe the stress-induced crack tip phase transformation mechanisms and the resulting stress and strain distribution in SMAs. In particular, the principal stress components for $\theta = 0$ in the austenitic untransformed region, $\sigma_{Ai}(r)$, are

Crack Stress Distribution and Stress Intensity Factor in NiTi Shape Memory Alloys

given by a modified Irwin correction [172] of the LEFM, i.e. by using effective crack length and SIF, a_e and K_{Ie} , respectively:

$$\sigma_{Ai}(r) = g_i \frac{K_{Ie}}{\sqrt{2\pi}(r-\Delta r)} \quad (5.1)$$

where $g_i = 1$ for $i=1, 2$ and $g_i = b$ for $i=3$, with $b=0$ for plane stress and $b=2n$ under plane strain conditions; Δr , a_e and K_{Ie} are given by (Figure 5.1)

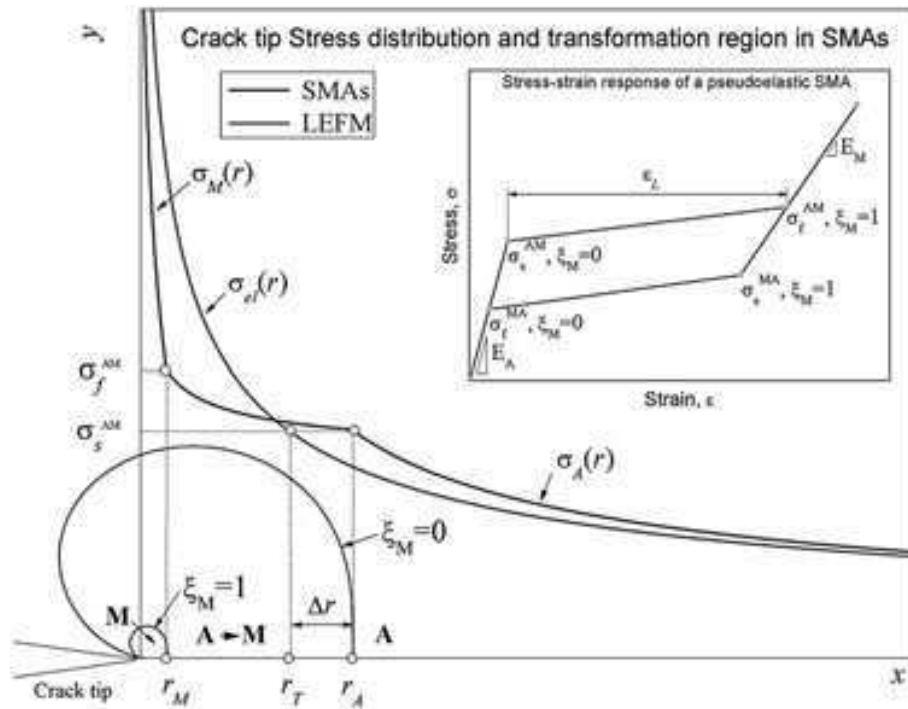


Figure 5.1: Schematic depiction of the crack tip stress distribution and transformation region in pseudoelastic shape memory alloys.

$$\Delta r = r_A - r_T \quad (5.2)$$

$$a_e = a + \Delta r \quad (5.3)$$

$$K_{Ie} = \beta \sigma_0 \sqrt{\pi a_e} \quad (5.4)$$

where β is a geometric factor and the distance r_T is given by:

$$r_T = \frac{(1-b)^2}{2\pi} \left(\frac{K_I}{\sigma_s^{AM}} \right)^2 \quad (5.5)$$

The principal stress components for $\theta = 0$ in the fully transformed martensitic region, $\sigma_{Mi}(r)$, are obtained by compatibility conditions and can be expressed as:

$$\sigma_{Mi}(r) = g_i \frac{2(1-\nu-bv)(K_{Ie}/\sqrt{2\pi r})(-E_A \varepsilon_L + \alpha_M^{-1} \sigma_f^{AM} - \sigma_s^{AM})}{(1-b)\alpha_M^{-1} + (b+1)((1-2\nu)} \quad (5.6)$$

where $\alpha_M = E_M/E_A$ is the Young's modulus ratio. The transformation radii, r_M and r_A , are given by the following equations:

$$r_M = \frac{2}{\pi} \left(\frac{(1-\nu-bv)(1-b(K_{Ie}))}{(1-b)E_A \varepsilon_L + (b+1)(1-2\nu)\sigma_f^{AM} + (1-b)(\sigma_s^{AM})} \right)^2 \quad (5.7)$$

$$r_A = \frac{2(1-b(K_{Ie}^2))}{\pi\sigma_s^{AM}(\sigma_s^{AM} + \sigma_f^{AM})} + \frac{2(E_A \varepsilon_L + \alpha_M^{-1} \sigma_f^{AM} - \sigma_s^{AM})r_M + 4(1-\nu-bv)K_{Ie}\sqrt{2r_M/\pi}}{(1-b)\alpha_M^{-1} + (b+1)((1-2\nu)(\sigma_s^{AM} + \sigma_f^{AM}))} + r_M \quad (5.8)$$

Finally, with the stress Eqs. (5.1) and (5.6), two different SIFs can be defined in the austenitic and martensitic regions. In particular, the mode I austenitic SIF, namely K_{IA} , can be directly obtained from Eq. (5.1) by considering the distance from the effective crack tip ($r=r-\Delta r$), according to the Irwin's assumption:

$$K_{IA} = \lim_{r \rightarrow 0} \sqrt{2\pi r} \sigma_A = K_{\pi e} \quad (5.9)$$

$$K_{IM} = \lim_{r \rightarrow 0} \sqrt{2\pi r} \sigma_M = \frac{2(1-\nu-bv)}{(1-b)\alpha_M^{-1} + (b+1)((1-2\nu)} K_{Ie} \quad (5.10)$$

Equation (5.10) shows that K_{IM} can be expressed as a function of K_{Ie} and of a material constant coefficient. However, it is worth noting that the knowledge of the extent of transformation region, in terms of r_A , is required to calculate both K_{IA} and K_{IM} by an iterative approach, similarly to the Irwin's correction for elastic-plastic materials; in addition, note that K_I in Eq. 5.5 must be replaced with K_{Ie} during iteration steps.

5.3. Experiments

Crack Stress Distribution and Stress Intensity Factor in NiTi Shape Memory Alloys

Single edge crack (SEC) specimens, shown in figure 5.2, have been manufactured by EDM, and the fracture tests have been carried out by following standard procedures and recommendations. However, it is worth noting that most of the conditions given by standard testing procedures, including the limitations on specimen thickness, cannot be applied to SMAs because of their unique constitutive behavior as well as to the raw material geometry. In fact, NiTi alloys are normally not used as a bulk material, and consequently, they are commercially available in the shape of wires, thin sheets and tubes.

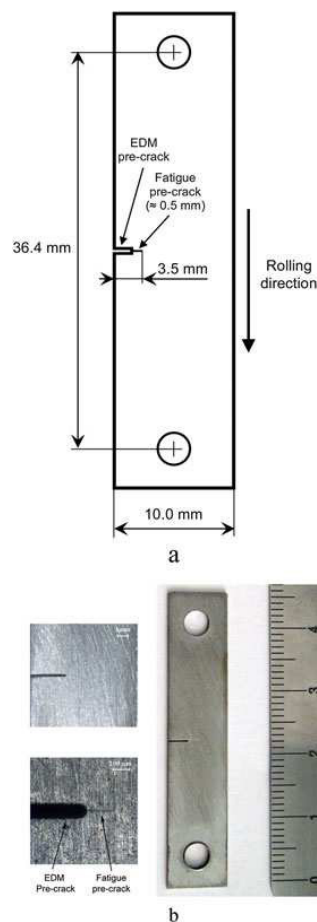


Figure 5.2: Single edge crack specimen: (a) shape and dimensions and (b) picture with highlights of the pre-crack.

Figure 5.2a shows the dimensions of the specimen, whereas figure 5.2b illustrates a picture of the specimen with highlights of the pre-crack. This latter was made by two subsequent steps: (1) EDM by using a copper wire ($f = 200 \text{ m}$) with a length of about 3

mm and (2) fatigue pre-crack with a length of about 0.5 mm. In particular, mode I isothermal tension–tension fatigue loads have been applied to create the fatigue pre-crack, by using a servo-hydraulic testing machine (Instron 8500) equipped with a climatic chamber, at a temperature $T = 303$ K and a nominal stress range $\Delta\sigma=50$ MPa with a loading ratio $R=0.1$. Even if standard procedures cannot be directly applied, it is worth noting that the nominal maximum stress is about 10% of the critical value for stress-induced austenite transformation which can be regarded as an equivalent yield strength in common metals; this is in accordance with standard recommendations for the production of fatigue pre-cracks. A travelling microscope and a strobe light source have been used to monitor the crack propagation until a fatigue pre-crack length of about 0.5mm has been obtained. Almost straight crack paths normal to the load direction, initiating from the notch radius of the EDM pre-crack, have been obtained in all specimens as illustrated in the optical micrographs of figure 5.2b. This result indicates that no spurious effects are introduced in the following fracture tests. These latter have been carried out by applying an isothermal monotonic tensile load until fracture under displacement control condition, at a crosshead speed of 0.005mms^{-1} . The tests were carried out at different values of the testing temperature for $T > A_f$ ($T_1 = 303$ K, $T_2 = 318$ K and $T_3 = 343$ K), and the load–displacement curves were recorded. Finally, the mode I SIF was computed, on the basis of LEFM theory, together with modified SIFs for SMAs, on the basis of the reference analytical model.

5.4. Numerical Modeling

The SEC specimen has been analyzed by two-dimensional plane stress FE analyses carried out by the commercial FE software code MSC Marc, which includes a special thermo-mechanical constitutive model for SMAs. In fact, with previous literature data [151] plane stress conditions may be expected in the adopted SEC specimens, as the conventional minimum thickness for plane strain conditions is much larger than the specimen thickness ($t = 0.5$ mm). Because of geometric and loading symmetries, only one half of the SEC specimen has been modeled, as illustrated in figure 5.3, which consists of

Crack Stress Distribution and Stress Intensity Factor in NiTi Shape Memory Alloys

about 50000 four-node bi-linear plane stress quadrilateral elements. A non-uniform mesh has been introduced by employing a very fine mesh in the crack tip region and a coarse mesh elsewhere, as clearly shown in figure 5.3, to capture the high stress gradients and to describe the stress-induced phase transformation mechanisms in SMAs. The load has been applied on the upper half of the hole by using interpolation elements, to reproduce as close as possible the real loading conditions.

Preliminary convergence studies have been carried out, to calibrate the FE model, by comparisons with a LEFM solution for an edge crack in a semi-infinite linear elastic plate. Subsequently, the calibration curve between the normalized SIF (K_I/K_0) and crack length ratio (a/W) has been obtained over a range of a/W between 0.2 and 0.5. In particular, the mode I SIF, K_I , has been computed by using the modified crack closure integral method, and it has been normalized with respect to the remote SIF $K_0 = \sigma_0 \sqrt{\pi a}$.

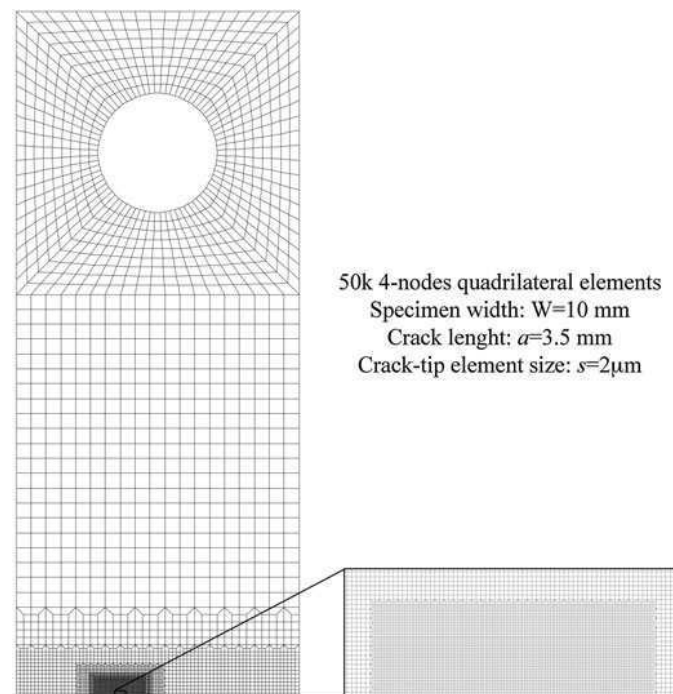


Figure 5.3: Finite element model of the single edge crack specimen with a highlight of the crack tip region.

Figure 5.4 illustrates the obtained FE results together with a comparison with a reference solution for an edge crack in a finite-width specimen subjected to a uniform remote

tensile stress. The comparison shows good agreements with differences of about 1% for $a/W < 0.4$ and not greater than 3% for higher values of a/W .

Nonlinear analyses have been carried out to analyze SMA specimens by using a special constitutive thermo- mechanical model for SMAs.³⁷ The numerical simulations have been performed under isothermal and fully austenitic conditions, i.e. for temperatures higher than A_f , in the range 303–343K, and the crack tip stress distributions and phase transformation mechanisms have been analyzed.

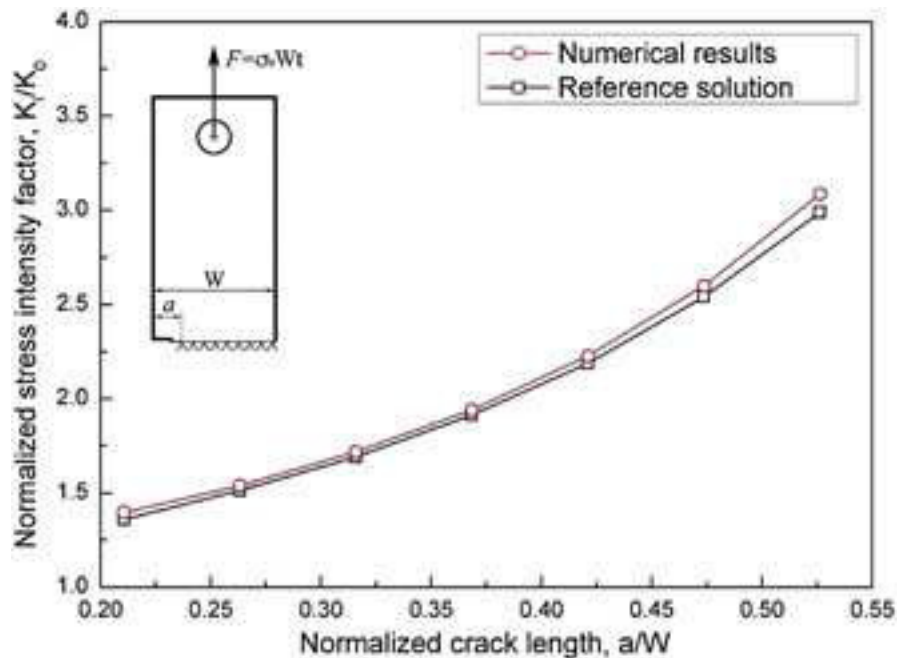


Figure 5.4: Comparison of the numerically obtained K_I/K_0 curve of the single edge crack specimen with a reference solution.

5.5. Results and Discussions

Figure 6 illustrates a comparison between numerical FE results and the predictions of the analytical model, in terms of crack tip normal stress for two different values of the testing temperature ($T = 303$ K and $T = 343$ K). The FE results have been obtained by applying a force $F = 600$ N, corresponding to a remote stress $\sigma_0 = 120$ MPa, whereas the analytical results were obtained by using Eqs (5.1)–(5.8) and the geometric factor $\beta = K_I/K_0$

reported in Fig. 5.4. Figure 5.5 clearly shows a marked effect of the temperature on both stress distribution and transformation region as a direct consequence of the Clausius–Clapeyron relation, as also reported in previous works. In addition, the comparison between FE and analytical results shows satisfactory agreements in terms of both crack distribution and transformation region.

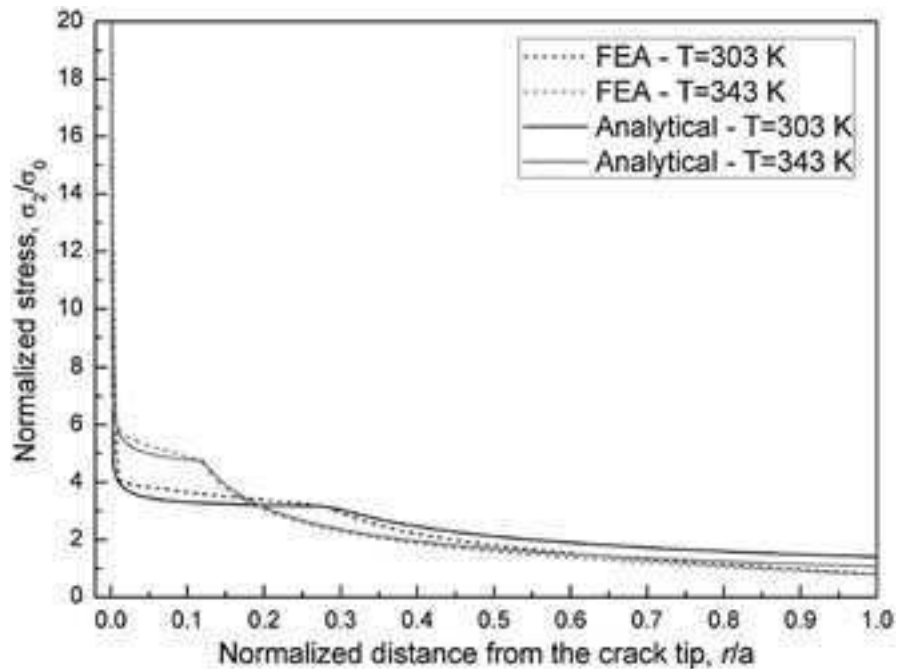


Figure 5.5: Crack tip normal stress for two different values of the temperature (303 and 343 K): comparison between numerical results and analytical predictions.

However, higher differences are observed for the lower value of the temperature ($T = 303$ K), which can be attributed to both numerical and analytical errors. In fact, the errors of FE model increase with decreasing the temperature, i.e. with decreasing the transformation stresses, due to the higher nonlinear effects and, consequently, to the numerical difficulties in obtaining accurate and robust numerical solutions. On the other hand, one of the basic assumptions of the analytical model, the small scale transformation condition, is violated with increasing the extent of the transformation region, as discussed previously, and consequently, the errors increase with decreasing the temperature. However, it is worth noting that the temperature $T = 303$ K is very close to the austenite finish temperature ($A_f = 286.7$ K), which represents the lower bound for pseudoelasticity.

Crack Stress Distribution and Stress Intensity Factor in NiTi Shape Memory Alloys

The analytical model has been developed to predict the crack tip stress distribution along the crack faces, i.e. for $\theta = 0$, and consequently, it does not describe the shape of the crack tip transformation region. To better understand the evolution of the volume fraction of martensite, ξ_M , in the crack tip region, direct full field results have been obtained from the FE simulations as illustrated in figure 5.6.

In particular, this figure shows the contour plots of ξ_M for the two different values of the temperature ($T = 303$ K in figure 5.6a and $T = 343$ K in figure 5.6b) under plane stress conditions. As expected, the shape of the transformation region is similar to the plastic zone in common metals, as a direct consequence of the application of plasticity concept and common yield criteria to define the phase transformation conditions in SMAs. However, it is worth noting that the adopted constitutive model does not take into account the asymmetries between tension and compression in SMAs and slightly different contours could be observed, depending on the degree of asymmetry, triaxiality and grain texture as demonstrated in previous works [135, 164-165]. Figure 5.7 illustrates the results of isothermal mechanical tests of two SEC specimens in terms of applied load, P , and applied mode I SIF, KI^* , as a function of the crosshead displacement, d , of the testing machine. In particular, figure 5.7a has been obtained at the temperature $T = 303$ K, whereas figure 5.7b is relative to the temperature $T=343$ K. It is worth noting that only specimens with crack length to width ratio a/W between 0.3 and 0.4 have been analyzed and the applied SIF (KI^*) has been calculated by using the geometric factor ($b = K_I/K_0$) reported in figure 5.4; as a consequence, KI^* is based on classical assumptions of LEFM and does not take into account the crack tip transformation mechanisms in SMAs. A qualitative comparison between figure 5.7a and b shows that higher nonlinear effects are observed in the near peak region of the curves when decreasing the testing temperature. This effect has been observed in all SEC specimens, and it can be attributed to the decrease of the transformation stresses and, consequently, to the larger size of the crack tip transformation region, when decreasing the testing temperature.

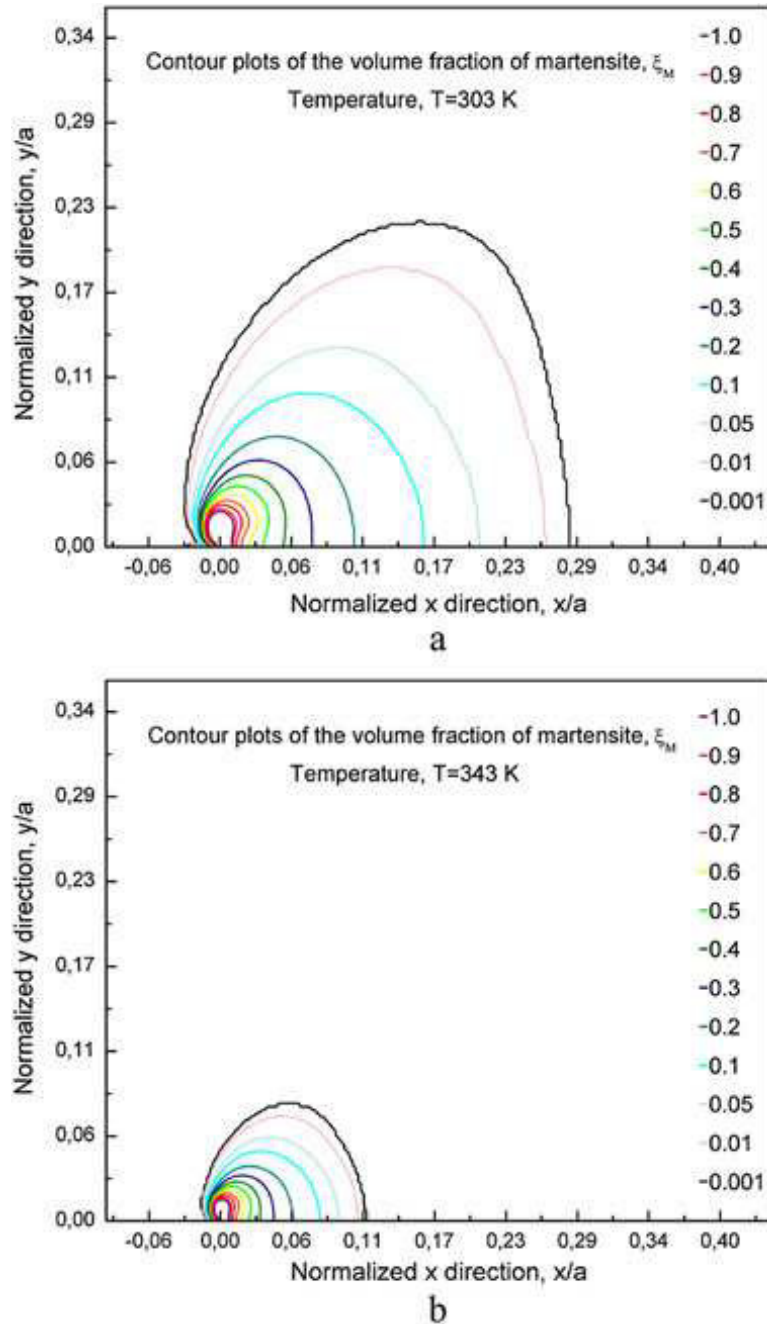


Figure 5.6: Contour plots of the volume fraction of martensite obtained from finite element simulations for two different values of the temperature: (a) $T = 303$ K and (b) $T = 343$ K.

The critical values of the SIF, namely K_{IC}^* , have been calculated for three different values of the testing temperature within the stress-induced transformation regime (303, 318 and 343K). It is worth noting that LEFM theories and standard procedures to calculate such parameter cannot be directly applied to SMAs, as most of the conditions given by LEFM are not fully met, because of the marked nonlinear effects resulting from

crack tip phase transition mechanisms. In any case, an average value of K_{IC}^* equal to $33.8 \text{ MPa m}^{1/2}$ has been computed in the investigated range of temperature, by using two specimens for each value of the testing temperature. This result is very close to previous literature results, which indicate an average K_{IC}^* equal to $34 \text{ MPa m}^{1/2}$ for pseudoelastic alloys and $31 \text{ MPa m}^{1/2}$ for martensitic alloys. In addition, a slight increase of K_{IC}^* with increasing the testing temperature has been recorded from about $32 \text{ MPa m}^{1/2}$ at $T=303\text{K}$ to about $35 \text{ MPa m}^{1/2}$ at $T = 343 \text{ K}$. This trend is in agreement with the predictions of the adopted analytical model, which estimate a reduction of both martensitic and austenitic SIFs (K_{IM} and K_{IA}) with increasing the temperature, i.e. it indicates a toughening effect. Furthermore, the critical values of these latter parameters, namely K_{IMC} and K_{IAC} , have been calculated by Eqs. (5.9) and (5.10), and average values equal to 22.6 and $38.5 \text{ MPa m}^{1/2}$, respectively, have been found. However, it is worth noting that the effects of testing temperature on fracture toughness of NiTi alloys, within the stress-induced transformation regime, were not directly analyzed previously, and further systematic studies should be carried out, by using a larger number of specimens and statistical methods, for a complete validation of the results.

For a deeper understanding of the fracture mechanisms, the morphology of the fracture surfaces has been analyzed by scanning electron microscopic (SEM) observations. As illustrated in figure 5.8, at low magnification, the surface morphology of the specimens can be divided into three regions that correspond to pre-crack EDM machining, room temperature fatigue pre-cracking and final fracture. The figure also shows the different observation regions: (1) crack initiation site, (2) at a distance of about 3 mm from the crack tip and (3) in the final fracture region.

Figure 5.9 illustrates SEM micrographs of a specimen tested at $T = 303 \text{ K}$, carried out at higher magnification. In particular, figure 5.9a shows the surface morphology of the fatigue crack initiation site (region #1), and a cleavage-like fracture is observed as also illustrated at higher magnification in figure 5.9b. Figure 5.9c and d shows fracture morphologies in the final fracture region and in particular in regions #2 (figure 5.9c) and #3 (figure 5.9d). Both figures exhibit dimpled appearance characteristic of tensile failures due to ductile fracture mechanisms, and small differences in dimple sizes are observed between the two regions. In additions, no significant differences have been observed

Crack Stress Distribution and Stress Intensity Factor in NiTi Shape Memory Alloys

between the fracture surfaces of the specimens analyzed at higher values of the testing temperature ($T = 318 \text{ K}$ and $T = 343 \text{ K}$), as it is also demonstrated by similar values of the critical SIFs.

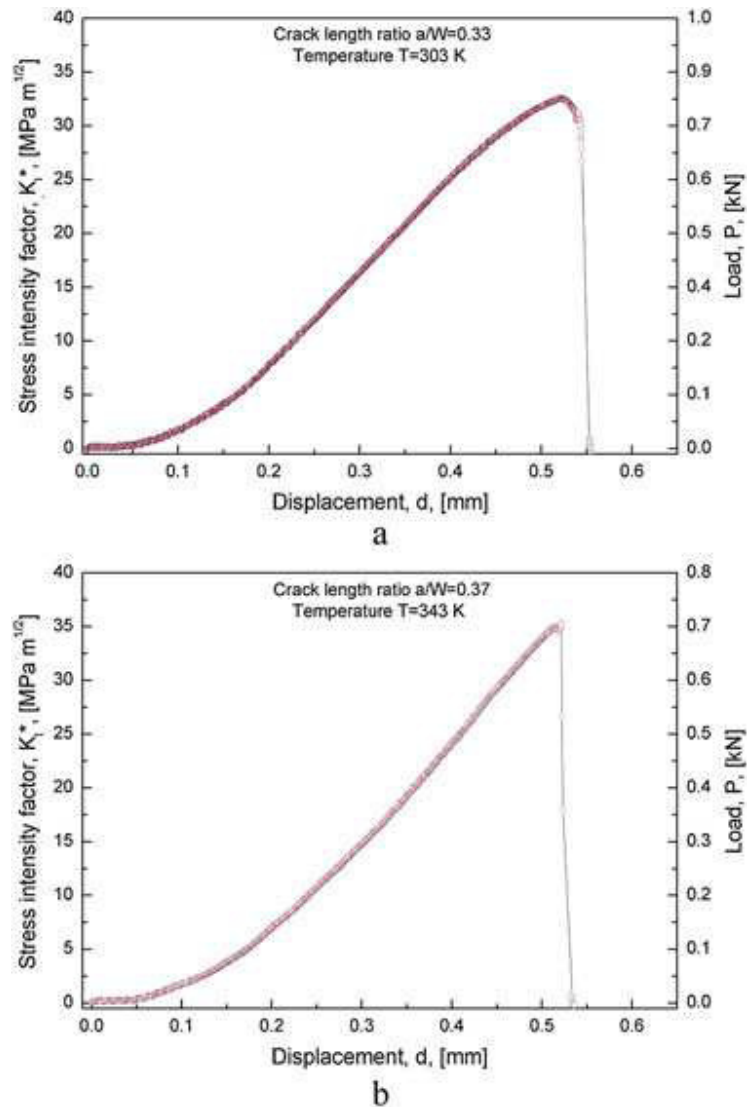


Figure 5.7: Isothermal mechanical tests of single edge crack specimens in terms of applied load (P) and mode I stress intensity factor (K_I^*) as a function of the crosshead displacement (d): (a) $T = 303 \text{ K}$ and (b) $T = 343 \text{ K}$.

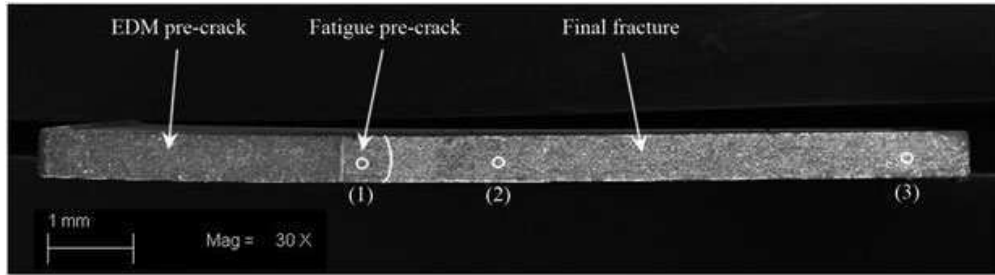


Figure 5.8: Scanning electron microscopic observation of the fracture surface at low magnification with highlights of the different fracture regions.

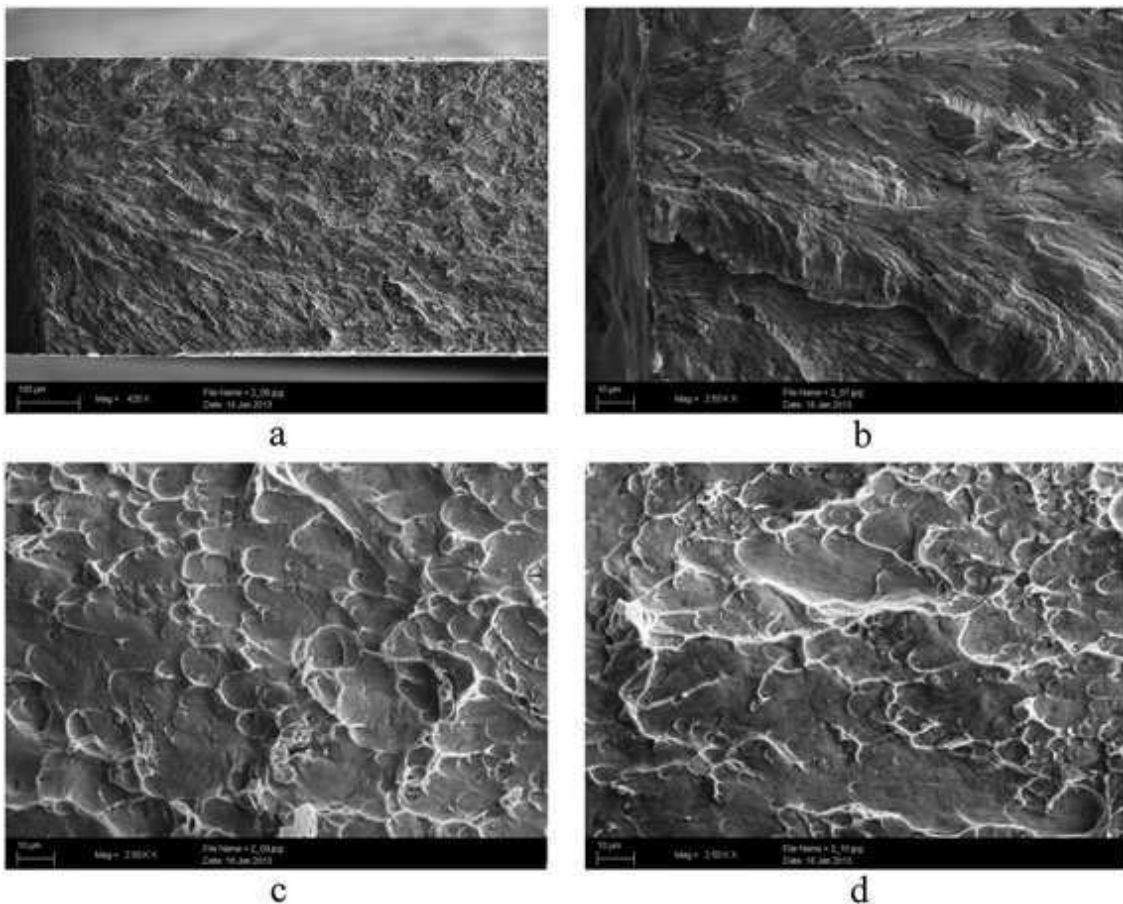


Figure 5.9: Surface morphology of the fracture surface: (a) crack initiation site (region #1), (b) crack initiation site at higher magnification, (c) final fracture (region #2) and (d) final fracture (region #3).

"La presente tesi è cofinanziata con il sostegno della Commissione Europea, Fondo Sociale Europeo e della Regione Calabria. L'autore è il solo responsabile di questa tesi e la Commissione Europea e la Regione Calabria declinano ogni responsabilità sull'uso che potrà essere fatto delle informazioni in essa contenute"

REFERENCES

- [1] Chang, L. C. & Read, T. A. 1951 Trans. AIME 191.
- [2] Buehler, W. J., Gilfrich, J. V. & Wiley, R. C. 1963 J. Appl. Phys. 34, p. 1475.
- [3] Arbuzov, I. A. & Khandros, L. G. 1964 Fiz. Met. Metalloved 17, p. 390.
- [4] Otsuka, K. & Shimizu, K. 1970 Scripta Met. 4, p. 469.
- [5] Wang, F. E. & Buehler, W. J. 1963 A Summary of Recent Research on the NiTiNOL Alloys and Their Potential Application in Ocean Engineering, Journal of Applied Physics 34.
- [6] Otsuka K and Ren X 2005 Physical metallurgy of TiNi-based shape memory alloys Progr. Mater. Sci. 50 511-678
- [7] L. Contardo, G. Guenin, Training and two way memory effect in Cu-Zn-Al alloy, Acta Metallurgica 38 (7) (1990) 1267–1272.
- [8] D. A. Miller, D. C. Lagoudas, Thermo-mechanical characterization of NiTiCu and NiTi SMA actuators: Influence of plastic strains, Smart Materials and Structures 9 (5) (2000) 640–652.
- [9] X. Ren, K. Otsuka, Universal symmetry property of point defects in crystals, Physical Review Letters 85 (5) (2000) 1016–1019.
- [10] P. Rodriguez, G. Guenin, Stability of the two way memory effect during thermal cycling of a high ms temperature Cu-Al-Ni alloy, Materials Science Forum 56–58 (2) (1990) 541–546.
- [11] K. Otsuka, C. M. Wayman (Eds.), Shape Memory Materials, Cambridge University Press, Cambridge, 1999.
- [12] Zhang, C. S., L. C. Zhao, T. W. Duerig, and C. M. Waymann (1990). Scripta Metallurgica et Materialia 24, 1807.
- [13] Lindquist, P. G. and C. M. Wayman (1990). Engineering aspects of shape memory. Butterworth-Heinemann.
- [14] H. Funakubo (Ed.), Shape Memory Alloys, Gordon and Breach Science Publishers, 1987.
- [15] B. Sanders, R. Crowe, E. Garcia, Defense advanced research projects agency–Smart materials and structures demonstration program

- overview, *Journal of Intelligent Material Systems and Structures* 15 (2004) 227–233.
- [16] J. Kudva, Overview of the DARPA smart wing project, *Journal of Intelligent Material Systems and Structures* 15 (2004) 261–267.
- [17] J. K. Strelec, D. C. Lagoudas, M. A. Khan, J. Yen, Design and implementation of a shape memory alloy actuated reconfigurable wing, *Journal of Intelligent Material Systems and Structures* 14 (2003) 257–273.
- [18] R. Mani, D. Lagoudas, O. Rediniotis, MEMS based active skin for turbulent drag reduction, in: *Proceedings of SPIE, Smart Structures and Materials*, Vol. 5056, San Diego, CA, 2003, pp. 9–20.
- [19] M. Tawfik, J. Ro, C. Mei, Thermal post-buckling and aeroelastic behaviour of shape memory alloy reinforced plates, *Smart Materials and Structures* 11 (2002) 297–307.
- [20] C. Nam, A. Chattopadhyay, Y. Kim, Application of shape memory alloy (SMA) spars for aircraft maneuver enhancement, in: *Proceedings of SPIE, Smart Structures and Materials*, Vol. 4701, San Diego, CA, 2002, pp. 226–236.
- [21] D. Pitt, J. Dunne, E. White, E. Garcia, SAMPSON smart inlet SMA powered adaptive lip design and static test, *Proceedings of the 42nd AIAA Structures, Structural Dynamics, and Materials Conference*, Seattle, WA, 16–20 April 2001 (2001) 1–11.
- [22] J. Mabe, R. Cabell, G. Butler, Design and control of a morphing chevron for takeoff and cruise noise reduction, in: *Proceedings of the 26th Annual AIAA Aeroacoustics Conference*, Monterey, CA, 2005, pp. 1–15.
- [23] T. Turner, R. Buehrle, R. Cano, G. Fleming, Modeling, fabrication, and testing of a SMA hybrid composite jet engine chevron concept, *Journal of Intelligent Material Systems and Structures* 17 (2006) 483–497.
- [24] J. H. Mabe, F. Calkins, G. Butler, Boeing’s variable geometry chevron, morphing aerostructure for jet noise reduction, in: *47th AIAA/ ASME / ASCE / AHS / ASC Structures, Structural Dynamics and Materials Conference*, Newport, Rhode Island, 2006, pp. 1–19.
- [25] V. Birman, Review of mechanics of shape memory alloy structures, *Applied Mechanics Reviews* 50 (11) (1997) 629–645.
- [26] H. Prahlad, I. Chopra, Design of a variable twist tiltrotor blade using shape memory alloy (SMA) actuators, in: *Proceedings of SPIE, Smart Structures and Materials*, Vol. 4327, Newport Beach, CA, 2001, pp. 46–

59.

- [27] A. Jacot, R. Ruggeri, D. Clingman, Shape memory alloy device and control method, U.S. Patent 7,037,076 (2 May 2006).
- [28] K. Singh, J. Sirohi, I. Chopra, An improved shape memory alloy actuator for rotor blade tracking, *Journal of Intelligent Material Systems and Structures* 14 (2003) 767–786.
- [29] D. Kennedy, F. Straub, L. Schetky, Z. Chaudhry, R. Roznoy, Development of an SMA actuator for in-flight rotor blade tracking, *Journal of Intelligent Material Systems and Structures* 15 (2004) 235–248.
- [30] R. Loewy, Recent developments in smart structures with aeronautical applications, *Smart Materials and Structures* 6 (1997) R11–R42.
- [31] C. Test, S. Leone, S. Ameduri, A. Concilio, Feasibility study on rotorcraft blade morphing in hovering, in: *Proceedings of SPIE, Smart Structures and Materials*, Vol. 5764, San Diego, CA, 2005, pp. 171–182.
- [32] A. Johnson, Non-explosive separation device, U.S. Patent 5,119,555 (June 1992).
- [33] O. Godard, M. Lagoudas, D. Lagoudas, Design of space systems using shape memory alloys, in: *Proceedings of SPIE, Smart Structures and Materials*, Vol. 5056, San Diego, CA, 2003, pp. 545–558.
- [34] C. Willey, B. Huettl, S. Hill, Design and development of a miniature mechanisms tool-kit for micro spacecraft, in: *Proceedings of the 35th Aerospace Mechanisms Symposium*, Ames Research Center, 9–11 May, 2001, pp. 1–14.
- [35] A. Peffer, K. Denoyer, E. Fossness, D. Sciulli, Development and transition of low-shock spacecraft release devices, in: *Proceedings of IEEE Aerospace Conference*, Vol. 4, 2000, pp. 277–284.
- [36] B. Carpenter, J. Lyons, EO-1 technology validation report: Lightweight flexible solar array experiment, Tech. rep., NASA Godard Space Flight Center, Greenbelt, MD (8 August 2001).
- [37] S. Shabalovskaya, Biological aspects of TiNi alloys surfaces, *Journal de Physique IV* 5 (1995) 1199–1204.
- [38] J. Ryhänen, Biocompatibility evolution of nickel-titanium shape memory alloy, Ph.D. thesis, Univeristy of Oulu, Oulu, Finland (1999).
- [39] L. Machado, M. Savi, Medical applications of shape memory alloys, *Brazilian Journal of Medical and Biological Research* 36 (2003) 683–691.

- [40] D. Mantovani, Shape memory alloys: Properties and biomedical applications, *Journal of the Minerals, Metals and Materials Society* 52 (2000) 36–44.
- [41] K. Speck, A. Fraker, Anodic polarization behavior of Ti-Ni and Ti-6Al-4V in simulated physiological solutions, *J Dent Res* 59 (100) (1980) 1590–1595.
- [42] G. Andreasen, T. Hilleman, An evaluation of 55 cobalt substituted nitinol wire for use in orthodontics, *Journal of the American Dental Association* 82 (1971) 1373–1375.
- [43] S. Thompson, An overview of nickel-titanium alloys used in dentistry, *International Endodontic Journal* 33 (2000) 297–310.
- [44] T. Duerig, A. Pelton, D. Stöckel, Superelastic nitinol for medical devices, *Medical Plastics and Biomaterials* (1997) 31–42.
- [45] D. Lagoudas, E. Vandygriff, Processing and characterization of niti porous sma by elevated pressure sintering, *Journal of intelligent material system and structures* 13 (2002) 837–850.
- [46] J. Paine, C. Rogers, High velocity impact response of composites with surface bonded nitinol-SMA hybrid layers, *Journal of Intelligent Material Systems and Structures* 5 (4) (1994) 530–535.
- [47] B. Barnes, D. B. J. Luntz, A. Browne, K. Strom, Panel deployment using ultrafast SMA latches, in: *ASME International Mechanical Engineering Congress and Exposition, Chicago, Illinois, USA, 2006*.
- [48] K. Otsuka, T. Kakeshita, Science and technology of shape-memory alloys: New developments, *bulletin* (February 2002).
- [49] P. Anderson, A., S. Sangesland, Detailed study of shape memory alloys in oil well applications., *Sintef petroleum research, Trondheim, Norway* (1999).
- [50] I. Ohkata, Y. Suzuki, The design of shape memory alloy actuators and their applications, in: K. Otsuka, C. M. Wayman (Eds.), *Shape Memory Materials*, Cambridge University Press, Cambridge, 1999, Ch. 11, pp. 240–266.
- [51] S. Saadat, J. Salichs, M. Noori, Z. Hou, H. Davoodi, I. Bar-on, An overview of vibration and seismic applications of NiTi shape memory alloy, *Smart Materials and Structures* 11 (2002) 218–229.
- [52] K. R. Melton, General applications of shape memory alloys and smart materials, in: K. Otsuka, C. M. Wayman (Eds.), *Shape Memory Materi-*

als, Cambridge University Press, Cambridge, 1999, Ch. 10, pp. 220–239.

- [53] J. Evans, D. Brei, J. Luntz, Preliminary experimental study of SMA knitted actuation architectures, in: ASME International Mechanical Engineering Congress and Exposition, 2006.
- [54] Otsuka K and Ren X 2005 Physical metallurgy of Ti–Ni-based shape memory alloys *Progr. Mater. Sci.* 50 511-678
- [55] Melton K N and Mercier O 1979 Fatigue of NiTi thermoelastic martensites *Acta Metall.* 27 137-144
- [56] Hornbogen E 2004 Review Thermo-mechanical fatigue of shape memory alloys *J. Mater. Sci.* 39 385-399
- [57] Pelton A R 2011 Nitinol Fatigue: A Review of Microstructures and Mechanisms *J. Mater. Eng. Perform.* 20 613-617
- [58] Miyazaki S, Imai T, Igo Y, and Otsuka K 1986 Effect of cyclic deformation on the pseudoelasticity characteristics of Ti-Ni alloys *Metall. Trans A.* 17 115-120.
- [59] Tobushi H, Shimeno Y, Hachisuka T and Tanaka K 1998 Influence of strain rate on superelastic properties of TiNi shape memory alloy *Mech. Mater.* 30 141-150
- [60] Bertacchini O W, Lagoudas D C and Patoor E 2009 Thermomechanical transformation fatigue of TiNiCu SMA actuators under a corrosive environment – Part 1: Experimental results *Int. J. Fatigue.* 31 1571-1578
- [61] Lagoudas D C, Miller D A, Rong L and Kumar P K 2009 Thermomechanical fatigue of shape memory alloys *Smart Mater. Struct.* 18 art no. 085021
- [62] Torra V, Isalgue A, Auguet C, Carreras G, Lovey F C, Soul H and Terriault P 2009 Damping in civil engineering using SMA. The fatigue behavior and stability of CuAlBe and NiTi alloys *J. Mater. Eng. Perform.* 18 738-745
- [63] Soul H, Isalgue A, Yamny A, Torra V and Lovey F C 2010 Pseudoelastic fatigue of NiTi wires: frequency and size effects on damping capacity *Smart Mater. Struct.* 19 1-7
- [64] Dolce M and Cardone D 2001 Mechanical behavior of shape memory alloys for seismic applications 2. Austenite NiTi wires subjected to tension *Int. J. Mech. Sci.* 43 2657-2677
- [65] Tobushi H, Hachisuka T, Yamada S and Lin P 1997 Rotating-bending

fatigue of a TiNi shape-memory alloy wire *Mech. Mater.* 26 35-42

- [66] Miyazaki S, Mizukoshi K, Ueki T, Sakuma T and Liu Y 1999 Fatigue life of Ti-50 at.% Ni and Ti-40Ni-10Cu (at.%) shape memory alloy wires *Mater. Sci. Eng. A* 273–275 658-663
- [67] Tobushi H, Nakahara T, Shimeno Y and Hashimoto T 2000 Low-cycle Fatigue of TiNi Shape Memory Alloy and Formulation of Fatigue Life *J. Eng. Mater-T ASME.* 122 186-191
- [68] Wagner M, Sawaguchi T, Kausträter G, Höffken D and Eggeler G 2004 Structural fatigue of pseudoelastic NiTi shape memory wires *Mat. Sci. Eng. A* 378 105-109
- [69] Eggeler G, Hornbogen E, Yawny A, Heckmann A and Wagner M 2004 Structural and functional fatigue of NiTi shape memory alloys *Mater. Sci. Eng. A* 378 24-33
- [70] Figueiredo A M, Modenesi P and Buono V 2009 Low-cycle fatigue life of superelastic NiTi wires *Int. J. Fatigue.* 31 751-758
- [71] Norwich D W and Fasching A 2009 A study of the effect of diameter on the fatigue properties of NiTi wire *J. Mater. Eng. Perform.* 18 558-562
- [72] Sawaguchi T, Kausträter G, Yawny A, Wagner M and Eggeler G 2003 Crack initiation and Propagation in 50.9 At. Pct Ni-Ti Pseudoelastic Shape-Memory Wires in Bending-Rotation Fatigue *Metall. Mater. Trans. A.* 34 2847-2860
- [73] Nemat-Nasser S and Guo WG 2006 Superelastic and cyclic response of NiTi SMA at various strain rates and temperatures *Mech. Mater.* 38 463–474.
- [74] Kang G, Kan Q, Yu C, Song D and Liu Y 2012 Whole-life transformation ratchetting and fatigue of super-elastic NiTi Alloy under uniaxial stress-controlled cyclic loading *Mater. Sci. Eng. A* 535 228–234
- [75] Casciati S and Marzi A 2011 Fatigue tests on SMA bars in span control *Engineering Structures* 33 1232–1239
- [76] McKelvey A L and Ritchie R O 1999 Fatigue-crack propagation in Nitinol, a shape-memory and superelastic endovascular stent material *J. Biomed. Mater. Res.* 47 301-308
- [77] McKelvey A L and Ritchie R O 2001 Fatigue-Crack Growth Behavior in the Superelastic and Shape-Memory Alloy Nitinol *Metall. Mater. Trans. A.* 32A 731-743

- [78] Stankiewicz J, Robertson S W and Ritchie R O 2007 Fatigue-crack growth properties of thin-walled superelastic austenitic Nitinol tube for endovascular stent *J. Biomed. Mater. Res.* 81A 685-691
- [79] Tablani R M, Simha N K and Berg B T 1999 Mean stress effects on fatigue of NiTi *Mater. Sci. Eng. A* 273–275 644-648
- [80] Tablani R M, Simha N K and Berg B T 2001 Mean strain effects on the fatigue properties of superelastic NiTi *Metall. Mater. Trans. A.* 32A 1866-1869
- [81] Runciman A, Xu D, Pelton A R and Ritchie R O 2011 An equivalent strain/Coffin –Manson approach to multiaxial fatigue and life prediction in superelastic Nitinol medical devices *Biomaterials.* 32 4987-4993
- [82] Moumni Z, Van Herpen A and Riberty P 2005 Fatigue analysis of shape memory alloys: energy approach *Smart Mater. Struct.* 14 287–292
- [83] Pelton A R, Gong X Y and Duerig T 2003 Fatigue testing of diamond-shaped specimens *Medical Device Materials – Proceedings of the Materials and the Processes for Medical Devices Conference 2003.* 199-204
- [84] Pelton A R, Schroeder V, Mitchell M R, Gong X Y, Barney M and Robertson S W 2008 Fatigue and durability of Nitinol stents *J. Mech Behav Biomed.* 1 153-164
- [85] Gall K, Sehitoglu H, Chumlyakov YI and Kireeva IV 1999 Pseudoelastic cyclic stress-strain response of over-aged single crystal Ti-50.8at% Ni *Scripta Materialia* 40(1) 7–12
- [86] Sehitoglu H, Anderson R, Karaman I, Gall K and Chumlyakov Y 2001 Cyclic deformation behavior of single crystal NiTi. *Mater. Sci. Eng. A* 314 67–74.
- [87] Wagner M, Nayan N and Ramamurty U 2008 Healing of fatigue damage in NiTi shape memory alloy *J. Phys. D Appl. Phys.* 41 1-4
- [88] Wang X, Xu B and Yue Z 2008 Phase transformation behavior of pseudoelastic NiTi shape memory alloys under large strain *J. Alloy Compd.* 463 417-422
- [89] Nayan N, Roy D, Buravalla V and Ramamurty U 2008 Unnotched fatigue behavior of an austenitic Ni-Ti shape memory alloy *Mater. Sci. Eng. A* 497 333-340
- [90] Nayan N, Buravalla V and Ramamurty U 2009 Effect of mechanical cycling on the stress-strain response of a martensitic Nitinol shape

memory alloy *Mater. Sci. Eng. A* 525 60-67

- [91] Stephens R I, Fatemi A, Stephens R R and Fuchs H O *Metal Fatigue in Engineering*, second ed., Wiley-Interscience, New York, 2000.
- [92] Auricchio F and Sacco E 1997 A one-dimensional model for superelastic shape memory alloys with different elastic properties between austenite and martensite *Int. J. NonLin. Mech.* 32 1101-1114
- [93] LExcellent C and Bourbon G 1996 Thermodynamical model of cyclic behaviour of Ti-Ni and Cu-Zn-Al shape memory alloys under isothermal undulated tensile tests *Mech Mater* 24 59- 73
- [94] Peters W H and Ranson W F 1981 Digital imaging techniques in experimental stress analysis *Opt. Eng.* 21 427-31
- [95] Chu T C et al 1985 Applications of digital-image-correlation techniques to experimental mechanics *Exp. Mech.* 25 232-44
- [96] Sutton M A et al 1986 Application of an optimized digital correlation method to planar deformation analysis *Image Vis. Comput* 4 143-50
- [97] Peters W H et al 1983 Application of digital correlation methods to rigid body mechanics *Opt. Eng.* 22 738-42
- [98] Sutton M A, McNeill S R, Helm J D and Chao Y J 2000 Advances in two-dimensional and three-dimensional computer vision *Topics in Applied Physics* vol 77 ed P K Rastogi (Berlin: Springer) pp 323-72
- [99] Schreier H W 2003 Investigation of two and three-dimensional image correlation techniques with applications in experimental mechanics PhD Thesis University of South Carolina
- [100] Luo P F et al 1993 Accurate measurement of three-dimensional displacement in deformable bodies using computer vision *Exp. Mech.* 33 123-32.
- [101] Helm J D, McNeil S R and Sutton M A 1996 Improved three-dimensional image correlation for surface displacement measurement *Opt. Eng.* 35 1911-20
- [102] Garcia D, Orteu J J and Penazzi L 2002 A combined temporal tracking and stereo-correlation technique for accurate measurement of 3D displacements: application to sheet metal forming *J. Mater. Process. Technol.* 125 736-42
- [103] Pan B, Xie H M, Yang L H and Wang Z Y 2009 Accurate measurement of satellite antenna surface using three-dimensional digital image correlation technique *Strain* 45 194-200

- [104] Schreier H W and Sutton M A 2002 Systematic errors in digital image correlation due to under matched subset shape functions *Exp. Mech.* 42 303–10
- [105] Lu H and Cary PD 2000 Deformation measurement by digital image correlation: implementation of a second-order displacement gradient *Exp. Mech.* 40 393–400
- [106] Giachetti A 2000 Matching techniques to compute image motion *Image Vis. Comput.* 18 247–60
- [107] Tong W 2005 An evaluation of digital image correlation criteria for strain mapping applications *Strain* 41 167–75
- [108] Press William H 2003 *C++ Numerical Algorithms* (Beijing: Publishing House of Electronics Industry)
- [109] Schreier H W, Braasch J R and Sutton M A 1999 Systematic errors in digital image correlation caused by intensity interpolation *Opt. Eng.* 39 2915–21
- [110] Knauss W G, Chasiotis I and Huang Y 2003 Mechanical measurements at the micron and nanometer scales *Mech. Mater.* 35 217–31
- [111] Pan B et al 2006 Performance of sub-pixel registration algorithms in digital image correlation *Meas. Sci. Technol.* 17 1615–21
- [112] Vendroux G and Knauss WG 1998 Submicron deformation field measurements: Part 2. Improved digital image correlation *Exp. Mech.* 38 86–92
- [113] Zhang Z F et al 2006 A novel coarse-fine search scheme for digital image correlation method *Measurement* 39 710–8
- [114] Chen DJ, Chiang FP, Tan YS and Don HS 1993 Digital speckle-displacement measurement using a complex spectrum method *Appl. Opt.* 32 1839–49
- [115] Sjodahl M and Benckert L R 1993 Electronic speckle photography: analysis of an algorithm giving the displacement with subpixel accuracy *Appl. Opt.* 32 2278–84
- [116] Hild F et al 2002 Multiscale displacement field measurements of compressed mineral-wool samples by digital image correlation *Appl. Opt.* 41 6815–28
- [117] Pan B, Xie H, Xia Y and Wang Q 2009 Large deformation measurement based on reliable initial guess in digital image correlation method *Acta Optica Sin.* 29 400–6 (in Chinese)

- [118] Pan B and Xie HM 2007 Digital image correlation method with differential evolution J. Optoelectron. Laser 18 100–3 (in Chinese)
- [119] Pan B 2009 Reliability-guided digital image correlation for image deformation measurement Appl. Opt. 48 1535–42
- [120] Yang FJ, He and Quan CG 2006 Characterization of dynamic micro-gyroscopes by use of temporal digital image correlation Appl. Opt. 45 7785–90
- [121] Hung PC and Voloshin PS 2003 In-plane strain measurement by digital image correlation J. Braz. Soc. Mech. Sci. Eng. 25 215–21
- [122] Wattrisse BC, Muracciole A and Nemoz-Gaillard JM 2001 Analysis of strain localization during tensile tests by digital image correlation Exp. Mech. 41 29–39
- [123] Pan B, Xu BQ, Chen D and Feng J 2005 Sub-pixel registration using quadratic surface fitting in digital image correlation Acta Metro. Sin. 26 128–34 (in Chinese)
- [124] Wang Metal 2008 A weighting window applied to the digital image correlation method Opt. Laser Technol. 41 154–8
- [125] Hua T et al 2007 A new micro-tensile system for measuring the mechanical properties of low dimensional materials—fibers and films Polym. Test 26 513–8
- [126] Sun W, Quan CG, Tay CJ and He XY 2007 Global and local coordinates in digital image correlation Appl. Opt. 46 1050–6
- [127] Sun W, Quan CG and He XY 2008 Dynamic characterization of a micro-gyroscope by digital image spectrum correlation Opt. Eng. 47 3
- [128] Wim VP, Assen AS, I lia RR, Stijn DP, Joris Dand Ventseslav C S 2008 Study of the deformation characteristics of window security film by digital image correlation techniques Opt. Lasers Eng. 46 390–7
- [129] Cheng P et al 2002 Full-field speckle pattern image correlation with B-spline deformation function Exp. Mech. 42 344–52
- [130] Besnard Getal 2006 Finite-element displacement fields analysis from digital images: application to portevinle chatelier bands Exp. Mech. 46 789–803
- [131] Sun Y F et al 2005 Finite element formulation for a digital image correlation method Appl. Opt. 44 7357–63
- [132] R.H. Dauskardt, T. W. Duerig and R. O. Ritchie. 1989. Effects Of In

Situ Phase Transformation On Fatigue-Crack Propagation In Titanium–Nickel Shape-Memory Alloys. *MRS Shape Memory Materials Vol.9* pp.243–249

- [133] R.L. Holtz, K. Sadananda, M.A. Imam. 1999. Fatigue Thresholds Of Ni-Ti Alloy Near The Shape Memory Transition Temperature. *International Journal of Fatigue* 21 (1999) S137–S145.
- [134] R. Vaidyanathan, D.C. Dunand 1, U. Ramamurty. 2000. Fatigue Crack-Growth In Shape-Memory Niti And Niti–Tic Composites. *Materials Science and Engineering A289* (2000) 208–216.
- [135] S.W. Robertson A, A. Mehta B, A.R. Pelton C, R.O. Ritchie. 2007. Evolution Of Crack-Tip Transformation Zones In Superelastic Nitinol Subjected To In Situ Fatigue: A Fracture Mechanics And Synchrotron X-Ray Microdiffraction Analysis. *Acta Materialia* 55 (2007) 6198–6207
- [136] S.W. Robertson, Robert O. Ritchie. 2007. In Vitro Fatigue–Crack Growth And Fracture Toughness Behavior Of Thin-Walled Superelastic Nitinol Tube For Endovascular Stents: A Basis For Defining The Effect Of Crack-Like Defects. *Biomaterials* 28 (2007) 700–709
- [137] Ken Gall, Jeff Tyber , Geneva Wilkesanders, Scott W. Robertson, Robert O. Ritchie b, Hans J. Maier. 2008. Effect Of Microstructure On The Fatigue Of Hot-Rolled And Cold-Drawn Niti Shape Memory Alloys. *Materials Science and Engineering A* 486 (2008) 389–403
- [138] Bing Pan, Kemao Qian, Huimin Xie and Anand Asundi. 2009 Two-dimensional digital image correlation for in-plane displacement and strain measurement: a review. *Meas. Sci. Technol.* **20** (2009) 062001 (17pp).
- [139] Riddell WT, Piascik RS, Sutton MA, Zhao W, McNeill SR, Helm JD. Determining fatigue crack opening loads from near-crack-tip displacement measurements, vol. 1343. *ASTM STP*; 1999. p. 157.
- [140] Sutton MA, Zhao W, McNeill SR, Helm JD, Piascik RS, Riddell WT. Local crack closure measurements: development of a measurement system using computer vision and a far-field microscope, vol. 1343. *ASTM STP*; 1999. p. 145.
- [141] Williams M.L. On stress distribution at base of stationary crack. *Am Soc Mech Eng Trans J Appl Mech* 1957;24:109.
- [142] Shah PD, Tan CL, Wang X. T-stress solutions for two-dimensional crack problems in anisotropic elasticity using the boundary element method. *Fatigue Fract Engng Mater Struct* 2006;29:343.

- [143] J. Carroll, C. Efstathiou, J. Lambros, H. Sehitoglu, B. Hauber, S. Spottswood, R. Chona. 2009. Investigation of fatigue crack closure using multiscale image correlation experiments. *Engineering Fracture Mechanics* 76 (2009) 2384–2398
- [144] Garrett J. Pataky, Michael D. Sangid, Huseyin Sehitoglu, Reginald F. Hamilton, Hans J. Maier, Petros Sofronis. 2012. Full field measurements of anisotropic stress intensity factor ranges in fatigue. *Engineering Fracture Mechanics* 94 (2012) 13–28
- [145] Tada H, Paris PC, Irwin GR. *The stress analysis of cracks handbook*. 2nd ed. St. Louis MO: Paris Productions Inc.; 1985.
- [146] Gall, K., Yang, N., Sehitoglu, H. and Chumlyakov, Y. I. (2001) Fracture of precipitated NiTi shape memory alloys. *Int. J. Fract.*, 109, 189–207.
- [147] Chen, J. H., Sun, W. and Wang, G. Z. (2005) Investigation on the fracture behavior of shape memory alloy NiTi. *Metall. Mater. Trans. A Phys. Metall. Mater. Sci.*, 36, 941–955.
- [148] Daymond, M. R., Young, M. L., Almer, J. D. and Dunand, D. C. (2007) Strain and texture evolution during mechanical loading of a crack tip in martensitic shape-memory NiTi. *Acta Mater.*, 55, 3929–3942
- [149] Daly, S., Miller, A., Ravichandran, G. and Bhattacharya, K. (2007) An experimental investigation of crack initiation in thin sheets of nitinol. *Acta Mater.*, 55, 6322–6330.
- [150] Gollerthan, S., Herberg, D., Baruj, S. and Eggeler, G. (2008) Compact tension testing of martensitic/pseudoplastic NiTi shape memory alloys. *Mat. Sci. Eng. A*, 481–482, 156–159.
- [151] Gollerthan, S., Young, M. L., Baruj, A., Frenzel, J., Schmahl, W. W. and Eggeler, G. (2009) Fracture mechanics and microstructure in NiTi shape memory alloys. *Acta Mater.*, 57, 1015–1025.
- [152] Gollerthan, S., Young, M. L., Neuking, K., Ramamurty, U. and Eggeler, G. (2009) Direct physical evidence for the back transformation of stress-induced martensite in the vicinity of cracks in pseudoelastic NiTi shape memory alloys. *Acta Mater.*, 57, 5892–5897.
- [153] Maletta, C., Falvo, A., Furgiuele, F., Barbieri, G. and Brandizzi, M. (2009) Fracture behaviour of nickel–titanium laser welded joints. *J. Mater. Eng. Perform.*, 18, 569–574.
- [154] Wang, G. Z. (2007) Effect of martensite transformation on fracture behavior of shape memory alloy NiTi in a notched specimen. *Int. J. Fract.*, 146, 93–104.

- [155] Wang, G. Z., Xuan, F. Z., Tu, S. T. and Wang, Z. D. (2010) Effects of triaxial stress on martensite transformation, stress– strain and failure behavior in front of crack tips in shape memory alloy NiTi. *Mater. Sci. Eng. A*, 527, 1529–1536.
- [156] Maletta, C., Falvo, A., Furgiuele, F. and Leonardi, A. (2009) Stress induced martensitic transformation in the crack tip region of a NiTi alloy. *J. Mater. Eng. Perform.*, 18, 679–685.
- [157] Wang, X. M., Wang, Y. F., Baruj, A., Eggeler, G. and Yue, Z. F. (2005) On the formation of martensite in front of cracks in pseudoelastic shape memory alloys. *Mater. Sci. Eng. A*, 394, 393–398.
- [158] Baxevanis, T., Chemisky, Y. and Lagoudas, D. C. (2012) Finite element analysis of the plane strain crack-tip mechanical fields in pseudoelastic shape memory alloys, *Smart Mater. Struct.*, 21, art. no. 094012. 1–10.
- [159] Freed, Y. and Banks-Sills, L. (2001) Crack growth resistance of shape memory alloys by means of a cohesive zone model. *J. Mech. Phys. Solids*, 55, 2157–2180.
- [160] Birman, V. (1998) On mode I fracture of shape memory alloy plates. *Smart Mater. Struct.*, 7, 433–437.
- [161] Yi, S. and Gao, S. (2000) Fracture toughening mechanism of shape memory alloys due to martensite transformation. *Int. J. Solids Struct.*, 37, 5315–5327.
- [162] Yi, S., Gao, S. and Shen, L. (2001) Fracture toughening mechanism of shape memory alloys under mixed-mode loading due to martensite transformation.
- [163] Xiong, F. and Liu, Y. (2007) Effect of stress-induced martensitic transformation on the crack tip stress-intensity factor in Ni-Mn- Ga shape memory alloy. *Acta Mater.*, 55, 5621–5629.
- [164] LExcellent, C. and Thiebaud, F. (2008) Determination of the phase transformation zone at a crack tip in a shape memory alloy exhibiting asymmetry between tension and compression. *Scripta Mater.*, 59, 321–323.
- [165] LExcellent, C., Laydi, M. R. and Taillebot, V. (2011) Analytical prediction of the phase transformation onset zone at a crack tip of a shape memory alloy exhibiting asymmetry between tension and compression. *Int. J. Fract.*, 169, 1–13.
- [166] Desindes, S. and Daly, S. (2010) The small-scale yielding of shape memory alloys under mode III fracture. *Int. J. Solids Struct.*, 47, 730–

737.

- [167] Maletta, C. and Furgiuele, F. (2010) Analytical modeling of stress induced martensitic transformation in the crack tip region of nickel titanium alloys. *Acta Mater.*, 58, 92–101.
- [168] Maletta, C. and Furgiuele, F. (2011) Fracture control parameters for NiTi based shape memory alloys. *Int. J. Solids Struct.*, 48, 1658–1664.
- [169] Maletta, C. (2012) A novel fracture mechanics approach for shape memory alloys with trilinear stress–strain behavior. *Int. J. Fract.*, 177, 39–51.
- [170] Maletta, C. and Young, M. L. (2011) Stress-induced martensite in front of crack tips in NiTi shape memory alloys: modeling versus experiments. *J. Mat. Eng. Perform.*, 20, 597–604.
- [171] Baxevanis, T. and Lagoudas, D. (2012) A mode I fracture analysis of a center-cracked in NiTi shape memory alloy panel under plane stress. *Int. J. Fract.*, 175, 151–166.
- [172] Irwin, G. R. (1960) Plastic zone near a crack and fracture toughness. In: *Proceedings of Seventh Sagamore Ordnance Materials Conference*, Syracuse University Press, Syracuse, NY, 63–78.